

ALPHA FOUNDATION FOR THE IMPROVEMENT OF MINE SAFETY AND HEALTH  
Final Technical Report

**1.0. Cover Page**

(AFC518-25)

**Project Title:**

Collecting Mine Dust Particles with Liquid-Coated Vibrating Meshes

**Period of Performance:**

Aug. 1, 2017 to Jan. 31, 2019 (18 months)

**Submitting Organization:**

Virginia Tech,  
Blacksburg, VA 24061-0001

**Principal Investigators:**

Sunghwan Jung at Virginia Tech (now at Cornell Univ. 607-225-5798; sj737@cornell.edu)

Aaron Noble at Virginia Tech (865-250-0498; aaron.noble@vt.edu)

Lei Pan at Michigan Tech (906-487-2569; leipan@mtu.edu)

Shima Shahab at Virginia Tech (540-231-6516; sshahab@vt.edu)

**Industry partner:**

Komatsu Mining Corp. Group (Attn. Joe Defibaugh; Engineer - Dust & Ventilation)  
120 Liberty Street  
Franklin PA 16323

**Acknowledgement/Disclaimer:**

This study was sponsored by the Alpha Foundation for the Improvement of Mine Safety and Health, Inc. (ALPHA FOUNDATION). The views, opinions and recommendations expressed herein are solely those of the authors and do not imply any endorsement by the ALPHA FOUNDATION, its Directors and staff.

<b>2.0. Executive Summary (1 page):</b>	<b>3</b>
<b>3.0. Concept Formulation and Mission Statement:</b>	<b>4</b>
3.1 Background Information:	4
3.2 Mission Statement	5
<b>4.0. Proof-of-Concept Technology Components:</b>	<b>6</b>
4.1 Fundamental Studies:	6
4.1.1 Macroscopic Particle-Mesh Interactions:	6
4.1.2 Microscopic particle-liquid attachment:	7
4.1.3 Vibrating Mesh Frequency:	9
Proof-of-concept analysis and experiments:	9
Experimental approach:	10
Computational methods on a vibrating mesh:	13
4.2. Laboratory Scrubber System:	15
4.2.1 System Overview:	15
4.2.2 Wind tunnel structure:	15
4.2.3 Axial fan:	16
4.2.4 Feeding system:	17
4.2.5 Sampling system:	19
4.2.6 Water management system:	20
4.2.7 Mesh and Shaker:	21
4.2.8 Process monitoring system:	23
<b>5.0. Proof of Concept Evaluation:</b>	<b>25</b>
5.1 Materials and Methods:	25
5.1.1 Coal dust characteristics:	25
5.1.2 Experimental Design	26
5.1.3 Laboratory Test Procedures	28
5.1.4 Experimental Data Analysis	29
5.2 Experimental Results	30
5.3 Experimental Challenges	38
<b>6.0. Technology Readiness Assessment:</b>	<b>39</b>
<b>7.0. Appendices:</b>	<b>42</b>
7.1 Particle Size-by-Size Analysis Data:	42
7.2. Image Analysis Technique for Tracking Particles:	72
7.3 Contact Angle Data	77

7.4 Surface modification of mesh	79
7.5 Determination of Surface Tension Components	80
<b>Findings:</b>	<b>81</b>
<b>8.0. Acknowledgement/Disclaimer:</b>	<b>82</b>
<b>9.0 References:</b>	<b>82</b>

## 2.0. Executive Summary (1 page):

Dust is an inherent byproduct of any mining activity. Especially, dust particulates less than 100  $\mu\text{m}$  raise notable health and safety concerns. In coal mining, concentrated airborne dust can generate explosive mixtures that are easily ignited and self-propagating, and the inhalation of small, respirable dust particles can cause incurable lung diseases, including silicosis and coal worker's pneumoconiosis (so called black lung). Mine operators have typically employed preventative particle-collecting devices in underground mines to suppress airborne dust, and Mine Safety and Health Administration's (MSHA) 2014 respirable dust rule mandates even further reductions to respirable dust concentrations. In particular, the static panel filter, instrumental in most scrubber designs, is fundamentally limited in collection efficiencies, and causes numerous operational challenges.

The flooded-bed scrubber, has been developed and widely used for over 20 years as a preventative dust remover in continuous mining operations and has been recently tested on longwall shearers. Despite the proficiency of the scrubber, there are numerous technical challenges that limit the performance and efficiency of the flooded-bed scrubbers including high clogging rate. In this funded project, the PIs investigated a new design that reduces filter clogging, achieves uniformity of wetting, maintains high air flow rates, and enhances particle-liquid adhesion in collaboration with Komatsu Corp. The proposed design replaces the static panel filter with vibrating filter mesh to improve the particle-collecting efficiency as well as reducing the filter clogging issue.

Our microscopic and macroscopic dust collection studies on liquid-coated mesh shows that the use of both wetting agents and vibration benefits the droplet-dust attachment, which in turn increases the particle-capture rate. Based on this encouraging result, a bench-scale, proof-of-concept scrubber unit was fabricated. To properly evaluate the performance of the scrubber unit, systematic experimental tests were conducted based on a statistically designed program to identify the role of various operational factors (i.e. water flow rate, surfactant concentration, and mesh vibration frequency) in maximizing the dust collection efficiency. The analysis of the experimental results (direct particle sampling and high-speed photography) confirmed the importance of all parameters in the estimation of the collection efficiency.

Further analysis of the results showed that optimal collection efficiency can be achieved under a specific combination of water flow rate, surfactant concentration and mesh vibration frequency. Under these conditions, the bench-scale vibrating mesh scrubber unit was capable of capturing over 90% of the dust particles, a notable improvement over similar tests conducted with a simple static mesh. However, the results also show the importance of the mesh frequency in achieving this optimal result. Some tests at non-optimal vibration frequencies and water flow rates actual underperformed those conducted with a simple static mesh.

Altogether, these results confirm that the vibrating mesh approach can significantly outperform static mesh designs with respect to particle capture rate; however, the design parameters must be carefully considered to ensure optimal results. Data from the proof-of-concept tests can now be used for further engineering design and scale-up of the technology.



### 3.0. Concept Formulation and Mission Statement:

#### 3.1 Background Information:

This project aims to advance Atmospheric Purification Technologies using an innovative design idea this is developed via a rigorous understanding of particle-fluid interactions. Inhaling coal mine dust is known to cause several types of respiratory disease as tiny coal mine particles stay in lung tissues. The concentration of mine dust is one of the important factors to coal mine dust lung disease (CMDLD). Workers near drilling and cutting operations in underground mines have high risks to be diagnosed in CMDLD [1, 2], and currently no curative treatment exists for CMDLD. Therefore, prevention for CMDLD is the best practice to improve health and welfare of mine workers. NIOSH recommends the maximum concentration of dust particles in the workplace to be  $1 \text{ mg/m}^3$  and the respirable silica to be  $0.05 \text{ mg/m}^3$  (details are in ref. [3] and [4]). To achieve that level of particle concentration, dry and wet dust scrubbers were used in various industrial setups. Among them, wet dust scrubbers, especially flooded-bed scrubbers, are very efficient to remove small mine dust.

Flooded-bed scrubbers are commonly used to capture dust particles from continuous miners. In contrast to dry scrubbers, wet scrubbers are efficient to capture and retain fine particles at air/water interfaces by attractive capillary force if particles are hydrophilic. Wet scrubbers consist of a metal mesh panel, a mist collector, and a powered fan. The dust laden air is drawn through the panel and collector by the fan. The U.S. Bureau of Mines and the Mining Research and Development Establishment (MRDE) in the U.K. improved flooded bed filtration units. The higher the air speed and the smaller diameter in the mesh, the higher the capturing efficiency. Details in the flooded-bed scrubber developed by the MRDE are following [5].

Given the current state of the art in flooded bed dust scrubbers, four technical challenges identified:

First, *a filter mesh easily gets clogged* as dust-laden air flows through. Clogging is a very common problem in stationary porous membranes or filters as they capture dust particles. Moreover, fouled regions become hydraulically overloaded, which significantly reduces the efficiency of dust collection and the air flow speed. Therefore, removing clogged regions is necessary to enhance the overall efficiency of dust removal.

The second challenge is *a tradeoff between mesh fineness and air flow rate*. Free hole areas (FHA) are defined as a total clear area of a filter panel for air to pass through. In general, the air flow rate through a porous material depends on FHA and the pressure drop as expressed in Darcy's law. As the filter mesh gets closely packed, the flow rate is decreased. Hence, to maintain a certain flow rate, coarse filter meshes should be used, but the coarse meshes cannot capture the particles effectively.

Third, *poorly wetted areas* allow unfiltered dust-laden air to pass through. Adhesion between liquids and silica particles is a key mechanism to hold particulate liquid droplets in the flooded-bed scrubbers. If some regions in the filter do not have moisture or liquid

interfaces, the dust particles likely slide through the mesh because the attractive Van der Waals force between the mesh and silica particles is in an order of magnitude weaker than the force between the liquid interface and silica particles.

Finally, *attractive force between fluid interface and particles* should be optimized. When mine dust particles get close to a fluid interface on a filter, short-range force plays an important role in controlling a number of particles and stability of particles on the interface. By modifying the attraction strength of the liquid interface, the more particles will be captured and held in close proximity.

### **3.2 Mission Statement**

The overall goal of the project activities was to develop cost-effective & efficient particle-collecting devices (scrubbers) with liquid-coated vibrating filter meshes for the application of coal mine dust depression. In the laboratory-scale tests, the PIs proved that our innovative design would overcome three technical challenges in current wet scrubbers: to reduce filter clogging, to maintain high air flow rates, and to enhance particle-liquid adhesion/collection.

The underlying innovation lies in that vibration motions of mesh will reduce the clogging by shedding large particle agglomerates on a mesh, and simultaneously increase air flow rate with non-clogged open areas in the mesh. In addition, our proposed liquid-interface modification is able to uniformly wet the filter panel with liquids and increase the adhesion force between mine dust particles and liquid interfaces.

## 4.0. Proof-of-Concept Technology Components:

### 4.1 Fundamental Studies:

#### 4.1.1 Macroscopic Particle-Mesh Interactions:

The purpose of this subtask was to develop a method to characterize and measure the efficiency of mining meshes used at a macroscopic level. In this task, we used a surrogate mine dust obtained from a standard vendor (see details in Section 5.1.1). Meshes were designed based on the size and porosity of actual meshes obtained from Komatsu Co. To complete the task, we performed two types of experiments.

The first experiment used a single rod to mimic a mesh and observe how mine coal particles interact with the rod. Here, we used a state-of-the-art particle tracking method (see Fig. 1b) to measure the velocity and trajectory of individual particles and further quantify the particle capturing efficiency. The mine particles were contained in a small box attached to a shaker. By turning the shaker on, the particles were uniformly dispensed from the box onto the rod. Then, the particle tracking method measured the position of particles (see Fig. 1a). Dry rods cannot hold particles on the surface while wet rods hold them tightly.

Next, we performed an experiment with a mesh and dust particles as shown in Fig. 1c. In this case, a similar experimental setup was used as previously mentioned; however, the particles were distributed onto the flat steel mesh. The particle tracking software provided a mechanism to quantify the interactions of the coal particles with the mesh. Through experimentation and particle counting, it was found that the efficiency of the mesh as it captured coal particles was 53.6% (see Fig. 1d).

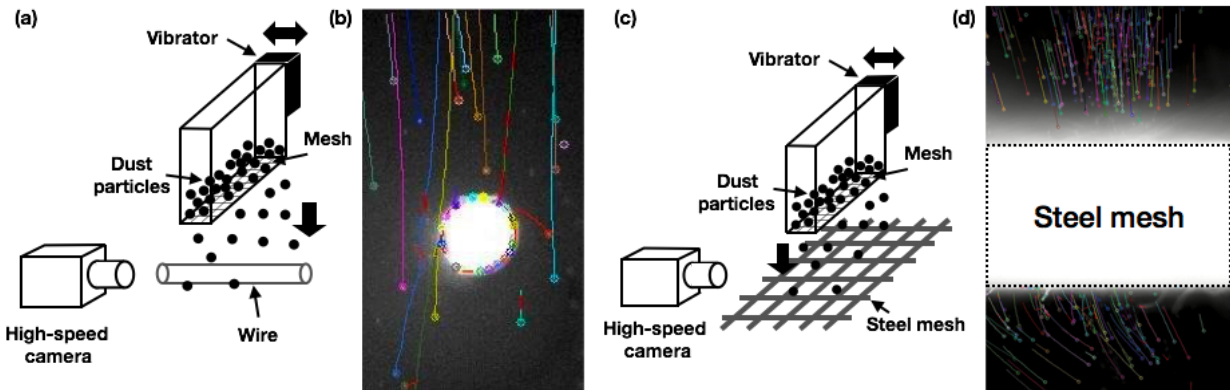


Figure 1. (a) Schematic of mine particles falling onto a rod. (b) Trajectories of particles with various colors around the rod (shown in white). (c) Schematic of mine particles falling onto a mesh. (d) Trajectories of particles through the mesh.

In summary, our technique to track individual particles is quite unique to quantify the particle size, speed, and density from high-speed videos. Using the same methodology, we analyzed the motion of particles in our proof-of-concept, bench-scale wind tunnel described in section 5.

#### 4.1.2 Microscopic particle-liquid attachment:

The objective of this task was to determine the optimal type and dosage for wetting agents to be used in the follow-up laboratory-scale testing. The effect of surfactant dosage on particle-liquid interaction was investigated at a microscopic level by: 1) contact angle measurement, 2) critical separation distance measurement, and 3) direct force measurement. Fig. 2a and 2b show a photo of our tool and a schematic drawing of our experimental setup, respectively.

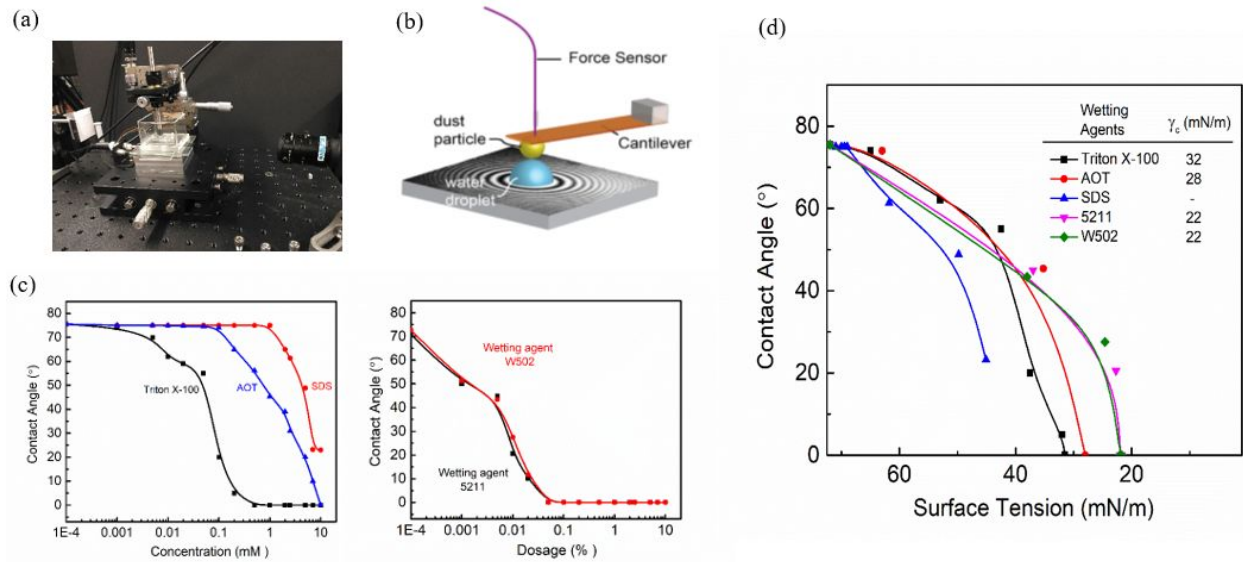


Figure 2. Experimental set-up (a), principle of measuring critical separation and force (b), the effect of surfactant concentration on contact angle (c), and the relationship between contact angle and liquid surface tension (d).

Fig. 2c shows the contact angles of wetting solutions on polished bituminous coal surfaces at different surfactant concentrations. Five surfactants were evaluated including, sodium dodecyl sulfate (SDS), Dioctyl sulfosuccinate sodium (AOT), and Triton X-100 as well as two commercial wetting agents, Dow 5211 and W502. Fig. 2d shows a relationship between the contact angle on bituminous coal surfaces and the surface tension of wetting liquids. Conclusions are drawn as below:

- All wetting agents lower the surface tension of liquid droplets, and increase the wettability of coal surfaces, but their performance varies.
- At 0.1 mM Triton X-100, coal surfaces can be wetted completely by wetting solutions.
- Triton X-100 is more effective than AOT and SDS. Wetting agents W502 and 5211 exhibit identical performance in increasing the wettability of coal particles.

Fig. 3 shows the results of interactions between a droplet of surfactant solution and a polished coal surface. Fig. 3a compares spatiotemporal profiles of the separation distance between water droplets and flat quartz plates of different hydrophobicities to represent hydrophobic coal and hydrophilic quartz surfaces. The radii of water droplets were controlled in the range of 0.56-0.60  $\mu\text{m}$ . The results of Fig. 3b shows the effect of solid's hydrophobicities on

critical separation distance between water droplets and solid surfaces. Table 1 shows characteristics related to the wettability of coal surfaces at different Triton X-100 surfactant concentration.

Table 1. The effect of Triton X-100 surfactant concentration on critical parameters related to the wettability of coal surfaces.  $\gamma_{LV}$  = liquid-vapor surface tension;  $\theta_e$  = coal contact angle;  $d_c$  = critical rupture thickness;  $t_c$  = critical rupture time.

	Concentration of Triton X-100 (mM)				
	0	0.01	0.05	0.1	0.2
$\gamma_{LV}$ (mN/m)	72.0	53.0	42.5	37.5	32.0
$\theta_e$ (°)	75.48	45.26	39.81	25.66	5.76
$d_c$ (nm)	148	560	744	>2000	>2000
$t_c$ (s)	1.15	0.25	0.15	-	-

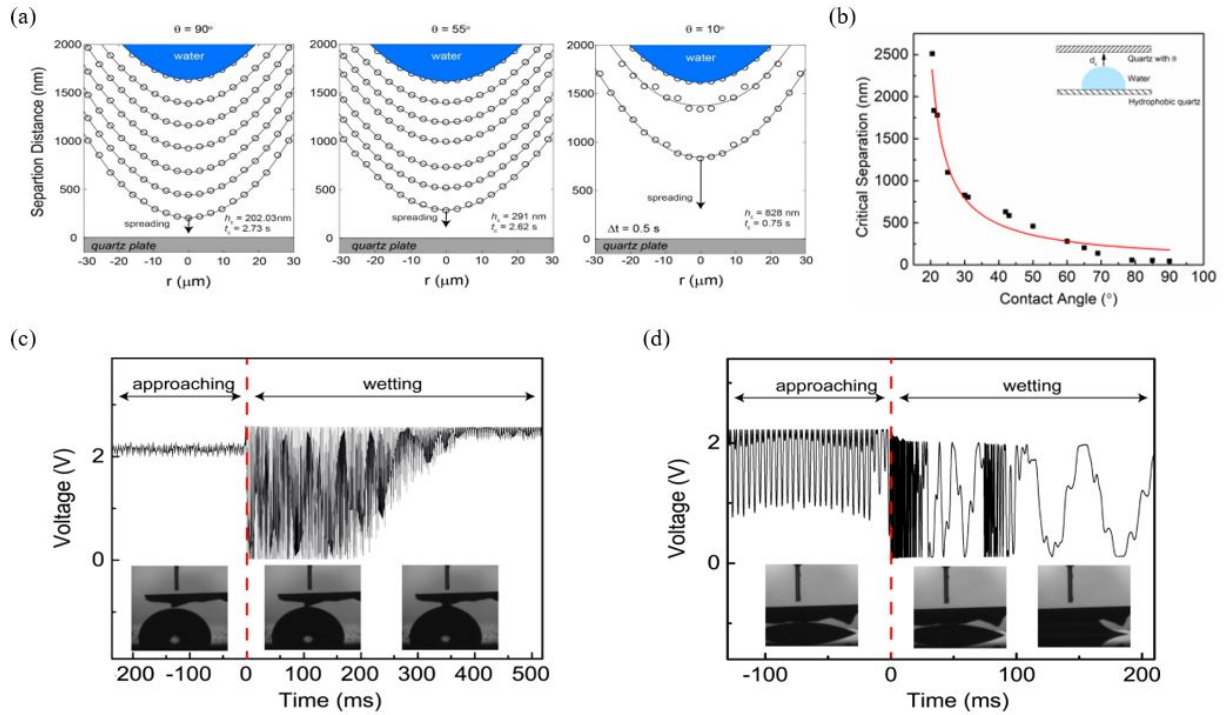


Figure 3. Effect of solid hydrophobicities on spatiotemporal profiles of air films between water droplets and quartz surfaces at a constant approaching velocity of 1200 nm/s (a) and critical separation distance of air films between water droplets and quartz plates (b); Force between coal surfaces and water droplets (c) and Triton X-100 solution (0.2mM) droplets (d) characterized by voltages and side-view images

Two major findings are shown as follows:

- The critical separation distance at which the water droplet captured coal particles increases with increasing surfactant concentration, while the critical time decreases with increasing the surfactant concentration. The results indicate that the use of wetting agents accelerates the capture process due to the presence of a strong attraction.
- The adhesion force with the use of wetting agents is much stronger than that obtained with pure water, confirming that the wetting agents enhance the capture of dust particles by water droplets.

#### 4.1.3 Vibrating Mesh Frequency:

##### Proof-of-concept analysis and microscopic experiments:

The objective of this task was to evaluate the effect of vibrating frequency and amplitude on the interaction between water droplets and solid surfaces. In this study, we have quantified one key characteristics of capture efficiency (*i.e.*, critical rupture thickness) and evaluated that value as a function of vibrational parameters. Tables 2 and 3 shows the result obtained between a vibrating water droplet and a flat solid surface. The vibration represents one element of the mesh.

Table 2. Effects of vibrational amplitudes ( $A_{p-p}$ ) on critical rupture distance ( $d_c$ ) between water droplets and hydrophobic quartz surfaces in air at a vibrational frequency ( $f$ ) of 500 Hz and 13 kHz.

$A_{p-p}$ (nm)	$d_c$ (nm)	
	$f = 500$ Hz	$f = 13$ kHz
25	62	65
48	63	400
76	65	700
106	223	980
133	882	1950

Table 3. Effects of vibrational frequencies ( $f$ ) on critical rupture distance ( $d_c$ ) between water droplets and hydrophobized quartz surfaces at fixed peak-to-peak amplitudes ( $A_{p-p}$ ) of 25 nm and 48 nm.

$f$ (kHz)	$d_c$ (nm)	
	$A_{p-p} = 25$ nm	$A_{p-p} = 48$ nm
0	60	60
4	65	144
8	65	460
12	65	380
16	65	364
20	70	1980
24	70	1650
28	70	1950
30	76	2050

Our experimental data obtained from microscopic fundamental tests confirmed that

- The use of vibration will increase critical separation distance at which the dust particles are wetted by water droplets, and thus vibration benefits the dust capture process by water spray. Both low-frequency vibration (500 Hz) and ultrasonic vibration ( $\sim 20$  kHz) benefits the capture of dust particles on water surfaces.
- The minimum vibrating amplitude at which the vibration plays a significant role is 48-133 nm depending on the vibrating frequency.
- We have shown that the use of vibration benefits capture efficiency by increasing critical rupture distance and attachment probability between dust particles and water surfaces. We also found that the performance of using ultrasonic vibration (13 kHz) is better than that of the lower frequency ( $\sim 500$  Hz).

However, we have also found that (as shown in Table 2) the use of 500 Hz vibration increased the critical rupture distance (i.e., a characteristics of capture efficiency) from 60 nm without vibration to 822 nm at the vibrating amplitude of 133 nm. This result confirms the use of resonant frequency ( $\sim 500$  Hz) will benefit the capture of dust

particles by vibrating mesh to a significant degree.

In the follow-up experiments, “the recommended vibration frequency” is given based on the results obtained from the tests for characterizing and measuring the efficiency of mining meshes used at a macroscopic level. The goal is analysing the interaction of particle flow stream with the vibrating structure in each element. Therefore, the experiments were performed for a beam to show the correlation between the local frequency and interaction surface area.

Note that The global optimal frequency in large-scale desktop experiments will be defined using modal vibration techniques that will be explained in the next section. In the following section we will analyse the global frequency response of the vibrating structure as the whole mesh not the element.

**Modal vibration experimental approach for different mesh configurations in large scale:**

As a fundamental hypothesis of our work, the maximum capture efficiency of a filter mesh can be obtained when the whole mesh vibrates at its maximum oscillation amplitude. This amplitude can be obtained when the mesh is excited at its natural (or resonance) frequency. Therefore, it is crucial to find the natural frequencies of the mesh and their associated modal behavior. For that reason, a series of parallel experimental and numerical studies were performed. Fig. 4a to 4d illustrate the experimental setup. Various mesh designs – e.g. framed coarse (Fig. 4a), non-framed coarse (Fig. 4b), various sizes, multilayered (Fig. 4c), woven (Fig. 4d), etc. – were manufactured, and evaluated in frequency sweep experiments to determine their resonance frequencies.



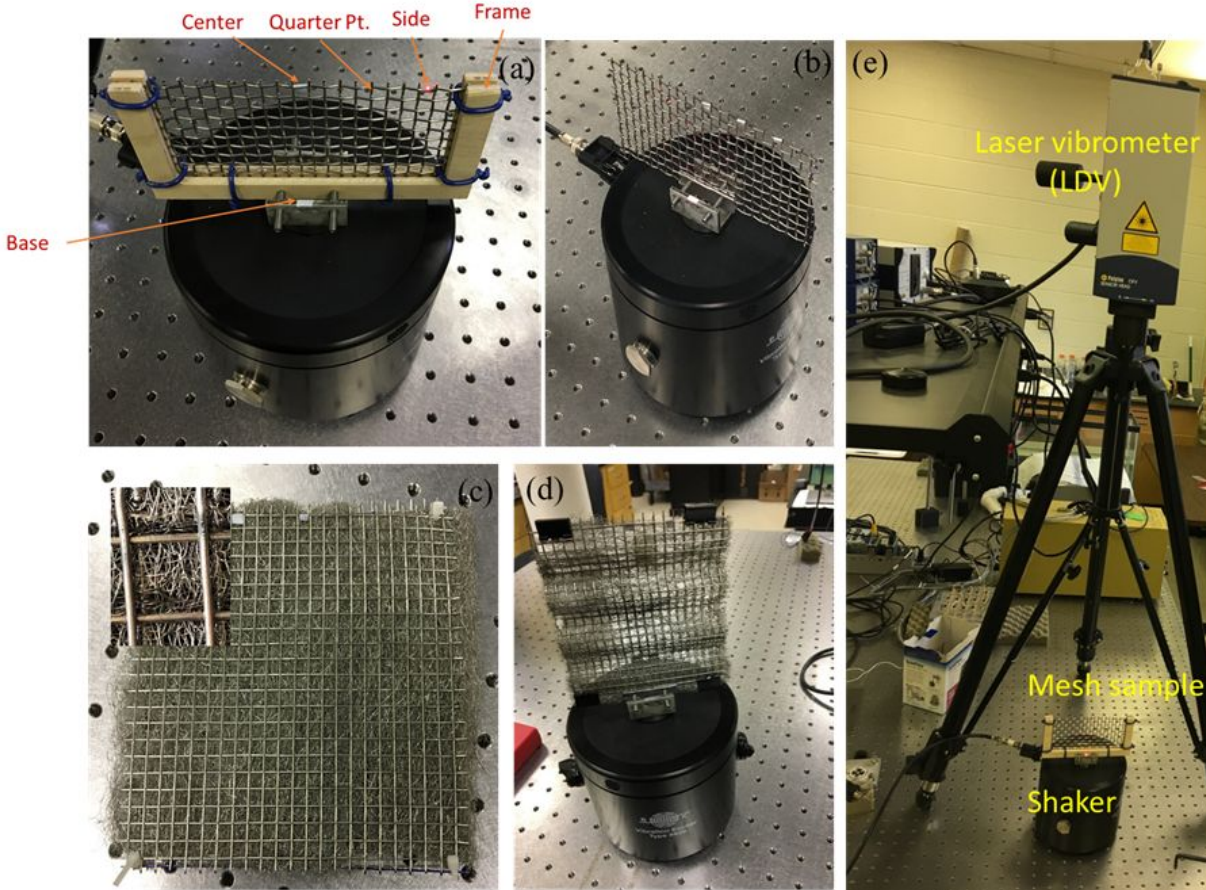


Figure 4. Experimental setup to investigate the frequency response of various mesh designs; (a) Framed coarse mesh, (b) non-framed coarse mesh, (c) multilayered mesh, and (d) woven mesh. (d) The mesh sample, mounted to the vibrating base from its edge, is under vertical excitation by the electromechanical shaker (Brüel and Kjær Type 4809). The transverse relative velocity at the base, center, and side of the mesh was measured by a laser vibrometer (Polytec OFV 5000/505 single-point LDV). The data acquisition device receives base acceleration from an amplifier which was fed by a waveform generator (Keysight 33500B series). Harmonic excitation was applied to the shaker through a Krohn-Hite Corp. 7500 amplifier for base excitation over a range of frequencies covering the fundamental mode of the mesh filter.

Figures 5a to 5d show the experimental results obtained from the frequency response tests for various mesh designs. For all the designs the resonance happens under 1000 Hz. It is observed that, for each configuration of the mesh, the resonance frequency for the whole mesh is much lower than the recommended frequency range obtained from the microscopic tests, using a cantilever beam as one element of the beam (in the previous section). This difference is due the geometric properties and boundary conditions changes, which were made in the structure. It should be noted that in our experimental efforts we studies both local and global optimal frequencies. The microscopic tests were performed to study one element of the mesh and gave information about the local optimal frequency (20-30 kHz), however, the large-scale tests were performed to study the global optimal frequency of the whole mesh (under 1000Hz). From microscopic experiments, we found that the use of vibration frequency

close to 500 Hz increased the critical rupture distance. This result confirms the use of resonant frequency ( $\sim 500$  Hz) will also benefit the capture of dust particles by vibrating mesh to a significant degree.

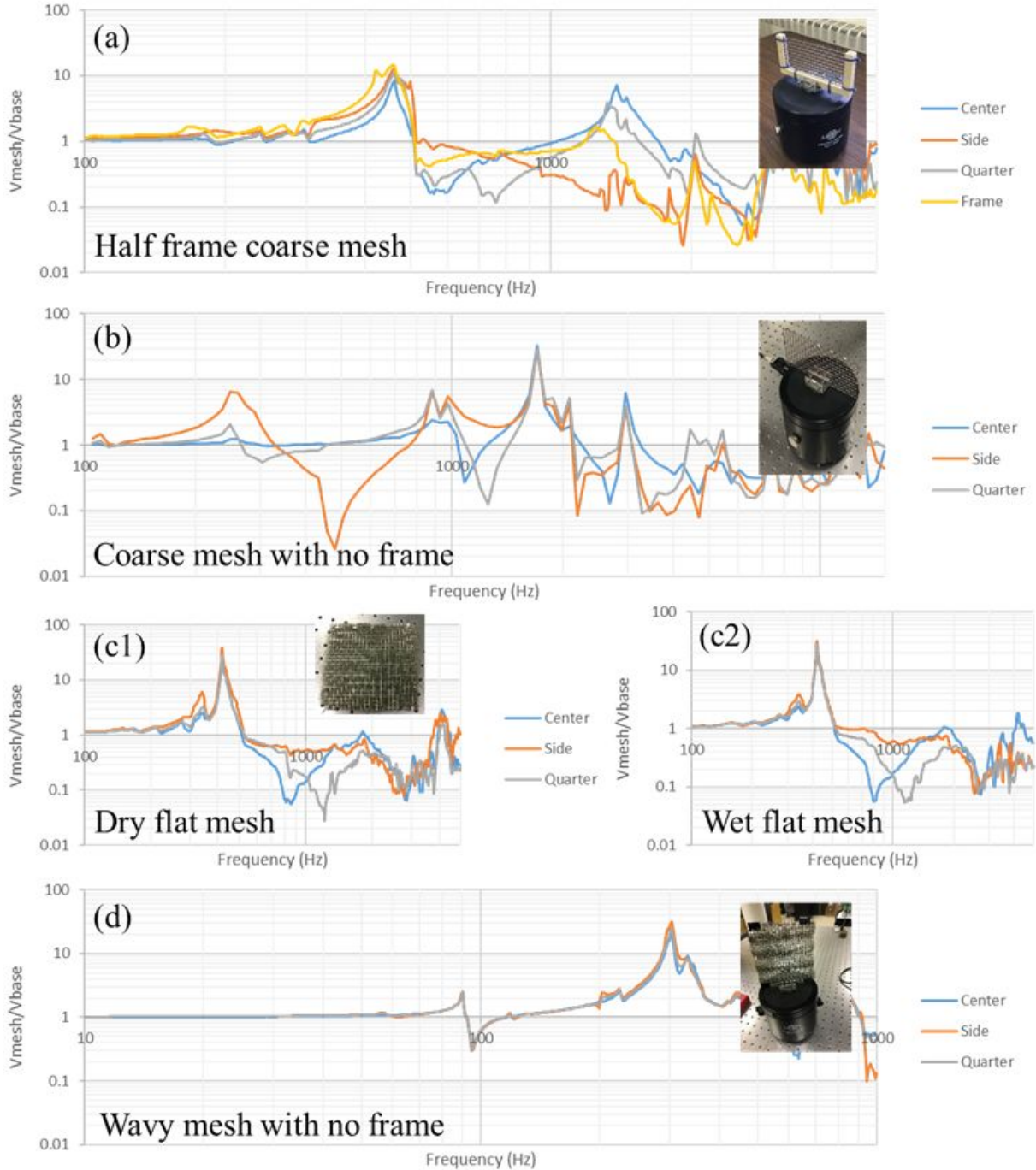


Figure 5. Experimental results obtained from the frequency response tests for various mesh designs; horizontal axis is frequency and vertical axis is velocity of the mesh/velocity of the base. (a) Framed coarse mesh, (b) non-framed coarse mesh, (c1) dry and (c2) wet multilayered flat mesh, and (d) wavy mesh. The resonance frequency of each design is obtained and shown,

where the maximum oscillation amplitude occurs. The mesh in (d) was made from raw material in the laboratory but tried to be close to the pattern and texture of the commercial mesh.

#### Computational methods on a vibrating mesh:

For this approach, we used multiphysics finite element (FE) 3D models to simulate two of the designed mesh filters in COMSOL. Modal analysis, as well as frequency sweep simulations were performed on the computer models. Figures 6 and 7 show the mode shapes of the two meshes under investigation occur for each frequency. The results show the deformation of the mesh happen during frequency sweep in experiments. These results give information about the mesh elements vibration which automatically set up the relevant physics and multiphysics couplings. From one side of the fluid-solid boundary, the acoustic-structure boundary interfaces handle the fluid pressure that acts on the solid domain and, from the other, the structural accelerated displacement that acts on the fluid domain and the flowing particles in the surrounding area. Multiphysics couplings encompass applications involving acoustic-solid within the frequency and time domains. The couplings involving structural shells are available when combining the Acoustics Module with the Structural Mechanics Module, where we are also able to access more advanced structural modeling capabilities. Having obtained the information about the mesh deformation, highly coupled and governing partial differential equations can be applied to resolve pressure distribution and flow patterns in the surrounding area of each element of the vibrating mesh. We can also expand this simulation to analyze particle collision on the vibrating mesh and the results can be given for various excitation frequency, mesh density and mesh material.

The results of the frequency sweep excitations for the experiments and FE simulations are shown in Figs. 8a and 8b, respectively. In Fig. 8, the peak frequencies and curve trends of the experiments and simulations showed a great agreement which is a promising result for further investigations. In addition, the agreement between the results confirmed the validity of our experimental approaches to realize the optimal frequency of the vibrating mesh.

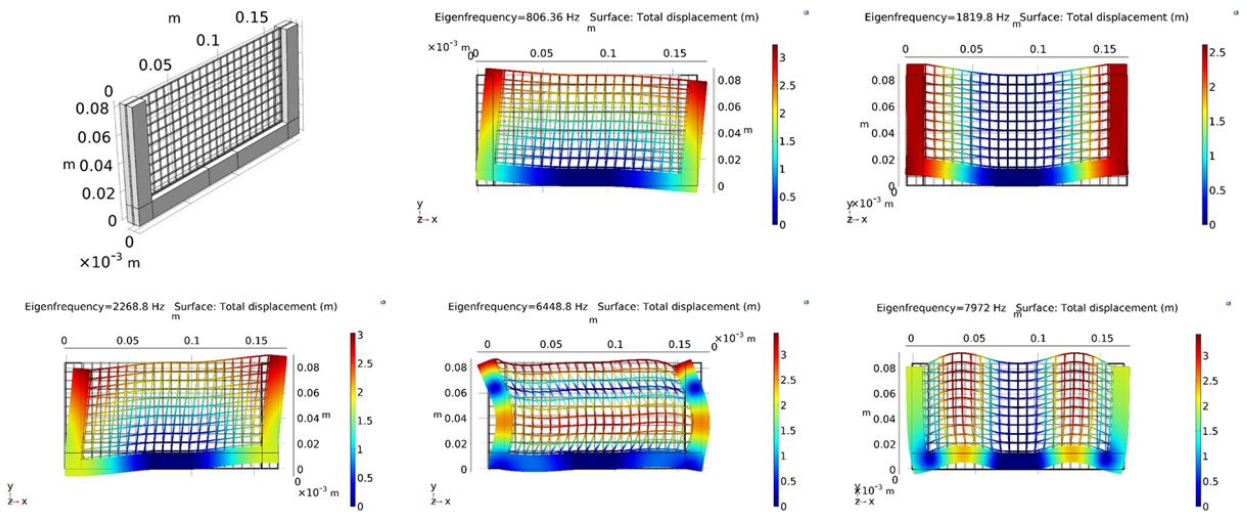




Figure 6. Results from FE simulations for a framed coarse mesh. Each mode shape is corresponding to a natural frequency of the mesh.

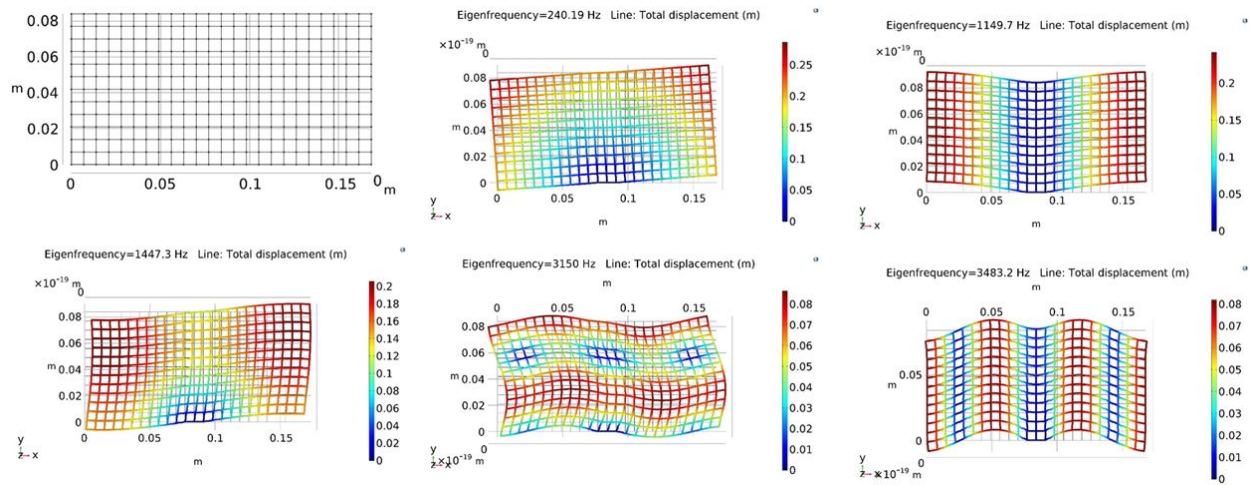


Figure 7. Results from FE simulations for a non-framed coarse mesh. Each mode shape is corresponding to a natural frequency of the mesh.

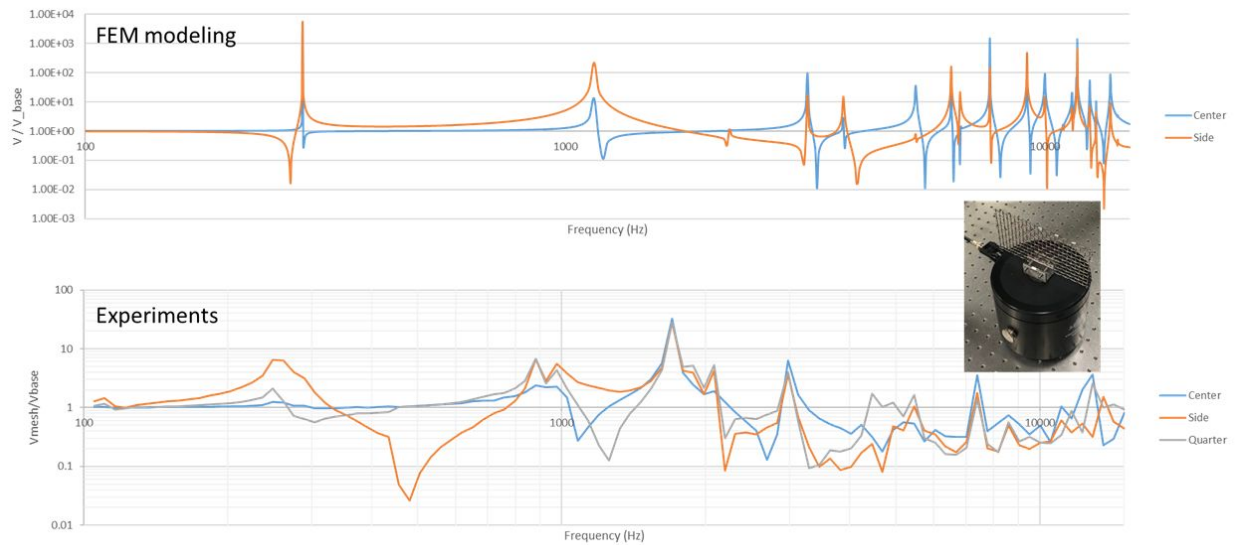


Figure 8. Results obtained from FEM simulations and experiments for a non-framed coarse mesh under base excitation by a shaker; relative velocity of the mesh vs. frequency. The first resonance frequency happens around 240 Hz.

## 4.2. Laboratory Scrubber System:

### 4.2.1 System Overview:

Following the microscopic and macroscopic test programs, a bench-scale, proof-of-concept scrubber system was designed and constructed to validate the conclusions derived from the fundamental studies in a realistic, yet controlled laboratory environment. The small-scale scrubber test apparatus ( $0.152\text{ m} \times 0.152\text{ m}$  in cross section) was designed and fabricated in a manner similar to the NIOSH unit described by Colinet and Jankowski (2000). As shown in Fig. 9, the bench-scale scrubber unit consists of three distinct ductwork sections: an upwind section where the feed is introduced, a middle section where the shaker panel is housed, and a downwind section where the clean air is discharged. The upwind and downwind panels are 1.22 meter in length and provide sufficient travel distance to stabilize the airflow. In addition, these panels provide access for dust sampling and process monitoring. Alternatively, the middle section is only 0.304 meter in length and contains an adjustable manifold to house the filter panel and the shaker.

In addition to the ductwork, other notable components of the system include: an innovative dust feed system, an air handling fan, the scrubber chamber, and air sampling ports. The dust feeding system is composed of a volumetric screw feeder and a Trost jet mill. This system was designed and placed at the entrance of the upwind section to effectively generate ultrafine dust particles, with fresh surfaces, and disperse them into the wind tunnel during testing. Air handling in the system is driven by a small axial fan that is attached to the downwind end of the ductwork. Lastly, the scrubber unit contains a spray manifold that is fed by a peristaltic pump. The pump rate can be varied from 0.175 L/min to 0.275 L/min. During testing, dust samples are collected at sampling ports located in both upwind and downwind of the scrubber unit using a linear IAQ sampling pump and air sampling cassettes. The remainder of this section describes the individual components of the bench-scale scrubber unit in further detail.

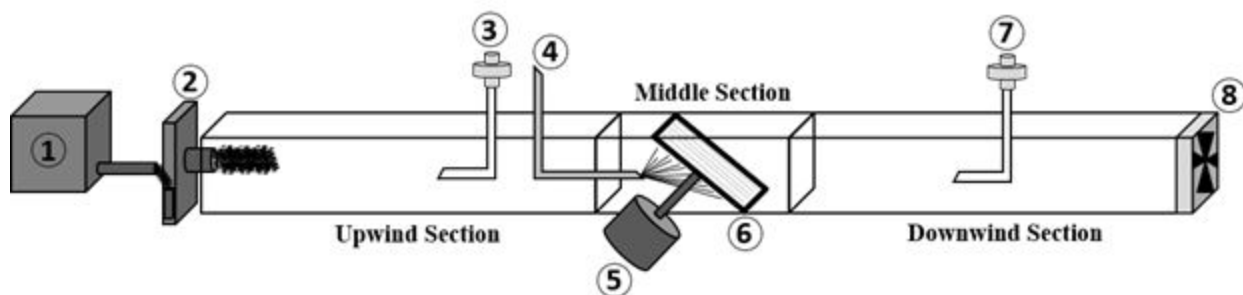


Figure 9. Schematic representation of the bench-scale, proof-of-concept, scrubber test facility: (1) volumetric screw feeder; (2) jet mill; (3) upwind sampling station; (4) spray manifold; (5) filter panel shaker; (6) Komatsu filter panel; (7) downwind sampling station; and (8) axial fan

#### 4.2.2 Wind tunnel structure:

The bench-scale scrubber unit was fabricated in three individual ductwork sections. Each section has a similar cross-section dimensions ( $0.152\text{ m} \times 0.152\text{ m}$ ). As shown in Fig. 10, the casting was constructed from 80/20 aluminum framing with the walls made from clear acrylic. The transparent acrylic walls provided the maximum visibility for the effective process monitoring and observation. The materials and assembly were chosen to maximize the design flexibility and ease the difficulty of design modifications during testing.

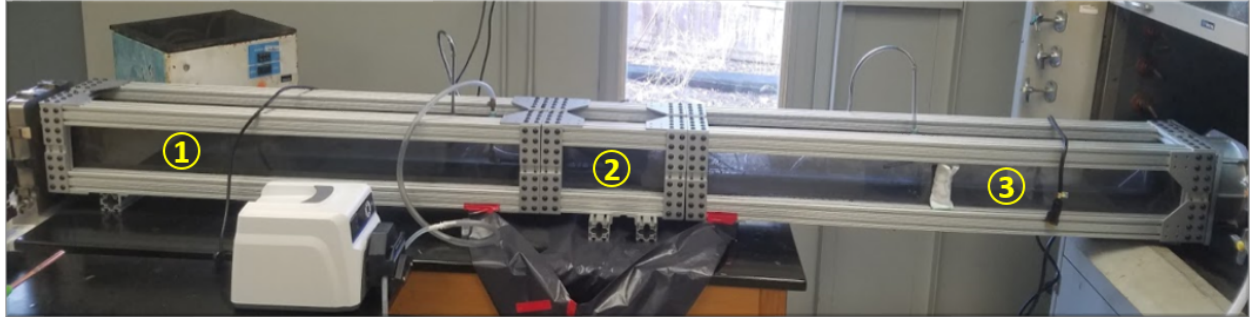


Figure 10. Bench-scale scrubber test facility: (1) upwind section; (2) mesh panel section; and (3) downwind section

#### 4.2.3 Axial fan:

Airflow through the tunnel was driven by an equipment-cooling fan. This axial fan was selected according to desired flows and expected pressure drop through the wind tunnel. The fan was positioned at the ending tail of the downwind section serving as the outlet of the wind tunnel. The air leaving the wind tunnel was then discharged into a laboratory fume hood normally used for coal crushing and coal sample preparation. Fig. 11 shows the fan and its position in the bench-scale scrubber unit. To estimate the flow rate in the wind tunnel, 20 measurements of air velocity were taken at the sampling stations in both tails of the scrubber unit using an Extech heavy duty hot wire cfm thermo-anemometer. The average air velocity in each section was determined by taking velocity readings at different heights in the ductwork and calculating the simple numeric average from readings. As shown in Table 4, the average air flow rate was 157 and 204 CFM (cubic-foot-meter) for the upwind and downwind section, respectively.

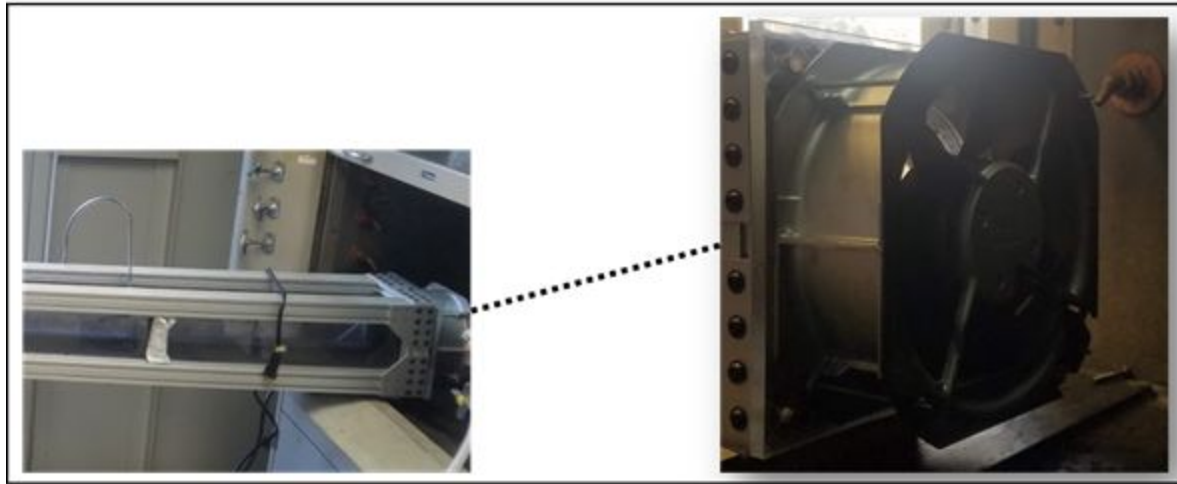


Figure 11. The axial fan used to pull the air through the scrubber unit (right panel) alongside its position in the testing setup (left panel).

Table 4. Air flow measurements in the upwind and downwind sections at different heights.

Air Flow Rate - CFM										
Upwind Section						Downwind Section				
Measurements	156.73	158.23	159.03	157.56	154.95	205.88	202.66	201.79	204.47	203.98
	159.25	156.96	157.88	155.23	156.73	206.73	206.13	202.64	203.66	206.05
	156.21	158.15	158.61	159.89	154.21	201.77	203.84	202.98	206.01	202.70
	155.89	155.08	157.79	158.55	157.77	201.69	204.55	201.98	205.45	203.88
Average	157.24					203.94				
Standard Deviation	1.58					1.66				

#### 4.2.4 Feeding system:

Coal dust particles were injected into the scrubber by an innovative feeding system composed of a volumetric screw feeder and a Trost jet mill (Fig. 12). Initially, a vibratory feeder was used to introduce material into the jet mill; however, preliminary shakedown testing showed that this method provided poor stability and control with regard to the actual mass feed rate. Later, an

alternate system was designed using a volumetric auger feeder. Later shakedown testing showed that this system provided a constant rate of 27.5 g/min throughout operation.

To reduce the size of original coal particles and create fresh dust surfaces, a laboratory-scale jet mill was employed. The Trost jet mill employs high velocity jets of compressed gas to impart energy to particles for size reduction. Interestingly, this device contains no moving parts in the grinding chamber, and the energy for size reduction is solely brought by the carrier gas. The primary grinding action is by particle-particle attrition, and as such, no contamination is introduced during the grinding process. The compressed air, typically 50 to 55-psi, sweeps the original feed particles around the grinding chamber. The particle interactions reduce the size of particles until the particles are fine enough to leave through the centrifugal classifier located in the grinding chamber. The main advantages of this novel feeding system for the current application can be summarized, as follows:

- The mill generates ultrafine particles, typically finer than 40-micron.
- The mill generates ultrafine particles with fresh surface. Surface oxidation has been reported as a common challenge in dust capture studies. This solution abates this issue, as the mill generates dust and feeds the wind tunnel in real time.
- The mill effectively disperses ultrafine particles and delivers them to the tunnel.
- The compressed air can be used as an auxiliary air handling mechanism by creating an additional air flow rate in the scrubber unit.
- The mill allows proper control of particle size and distribution by internal classification.
- The mill can maintain a constant feed flow rate by using a volumetric screw feeder.
- The mill is mechanically simple with no moving parts.



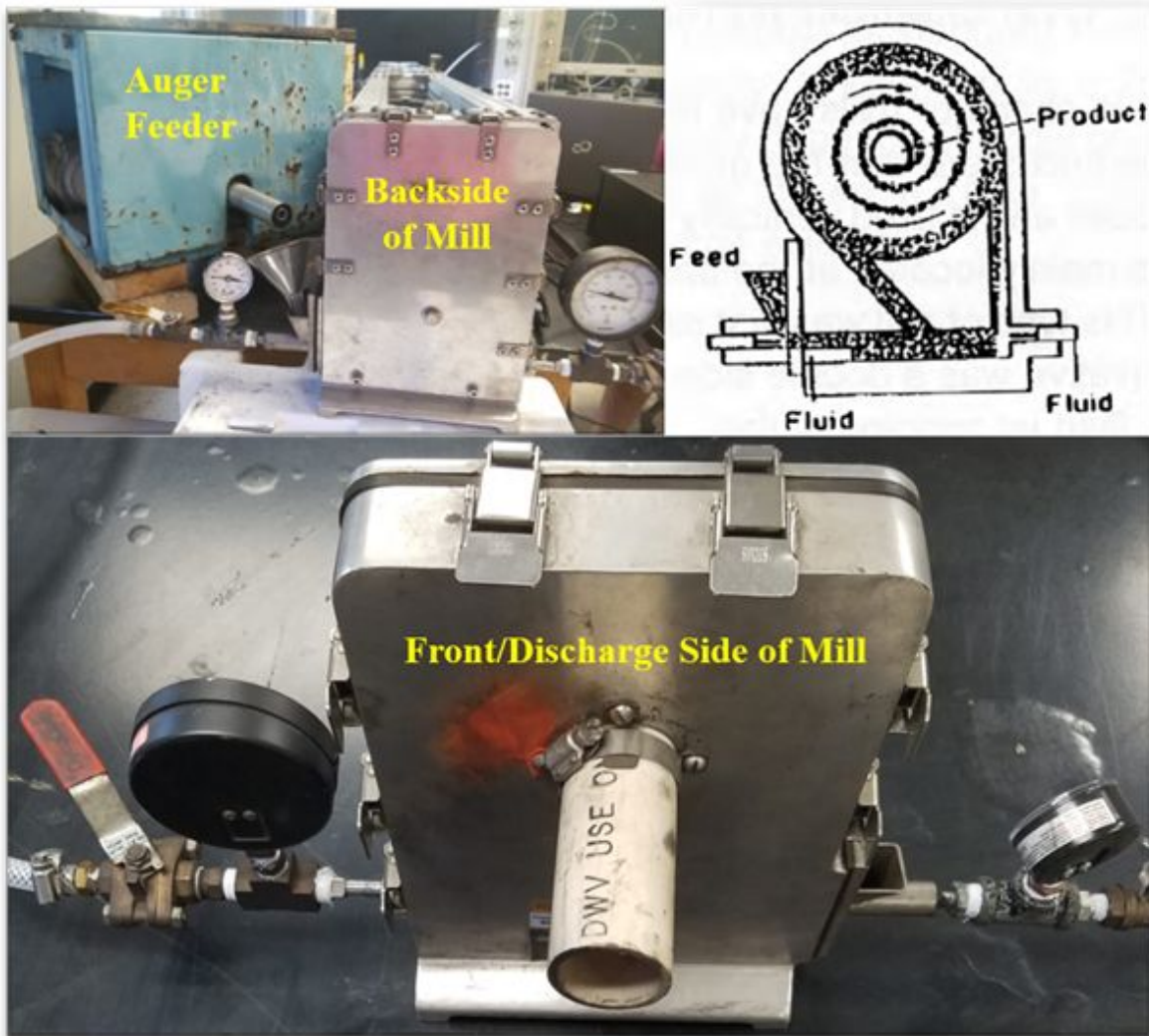


Figure 12. AccuRate volumetric screw feeder and Trost jet mill used to feed the scrubber.

#### 4.2.5 Sampling system:

During the capture tests, dust samples were collected at sampling stations located upwind and downwind of the bench-scale scrubber unit, as shown in Fig. 13. The upwind sampling location was approximately 0.9-meter downstream of the ductwork entrance, and the downwind sampling station was 0.6-meter downstream of the filter panel. Sampling glass tubes were located in the centerline of the ductwork at 0.9-meter height. Additionally, sampling tubes were inserted into the inlet of 37-mm preloaded air sampling cassettes containing Teflon filters. The outlet of the cassettes was connected to a linear IAQ sampling pump operating at a flow rate of 30 L/min. During the testing, dust samples were continuously collected on Teflon filters. These samples were then removed and weighed to calculate the collection efficiency.

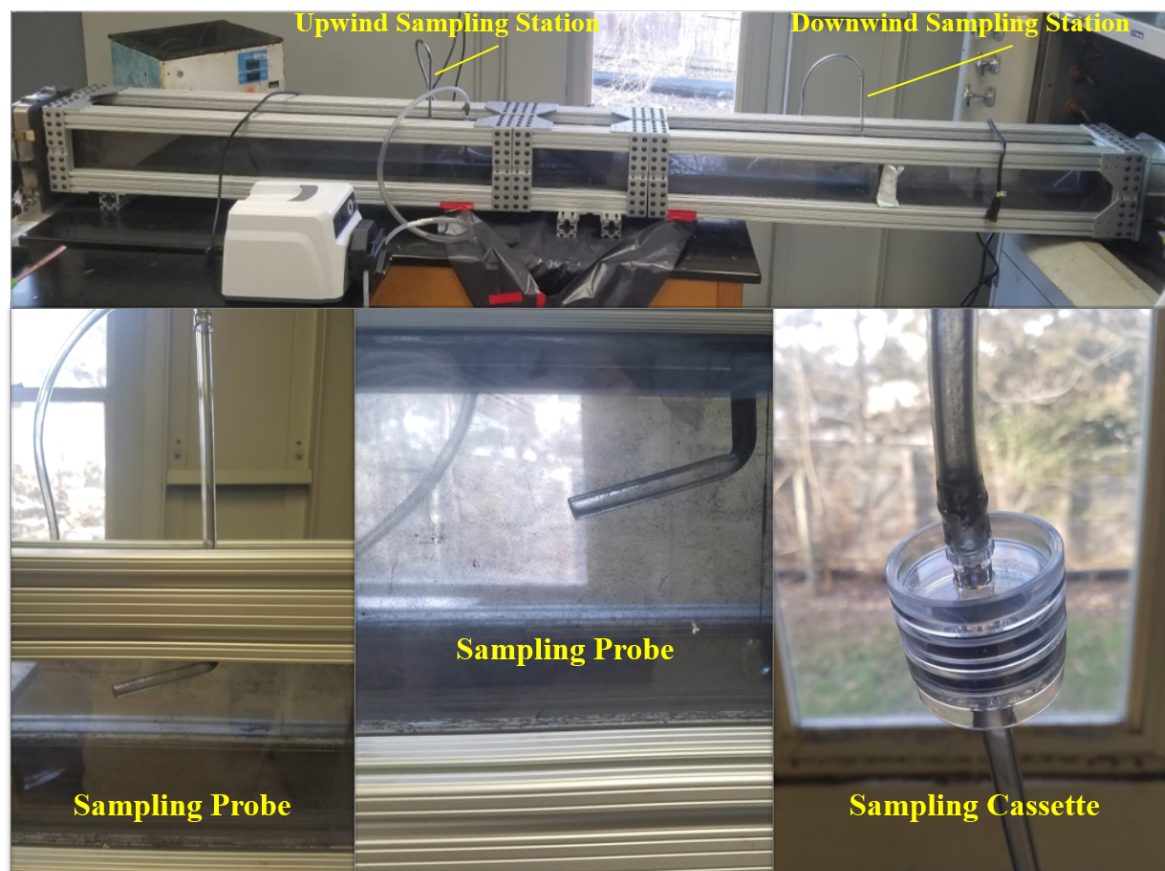


Figure 13. Sampling system and sampling stations at upwind and downwind sections.

#### 4.2.6 Water management system:

To properly control the flow rate of the water spray in the scrubber unit, a peristaltic pump was used. The Masterflex L/S Precision pump system is capable of producing a wide range of flow rates from 17 to 1700 mL/min at 6 to 600 rpm. For the experimental testing, C-Flex tubing with 4.8-mm inside diameter was used to deliver water to the spray nozzle at the maximum water pressure. As indicated in Fig. 14, the spray nozzle was located inside the middle panel ductwork spraying water on the surface of the mesh filter. To effectively spray water droplets on the surface of the mesh panel, a full-cone spray nozzle with 3.175-mm inside diameter was used. The spray nozzle was capable of spraying water at the range of pressure from 69 to 100 kPa.

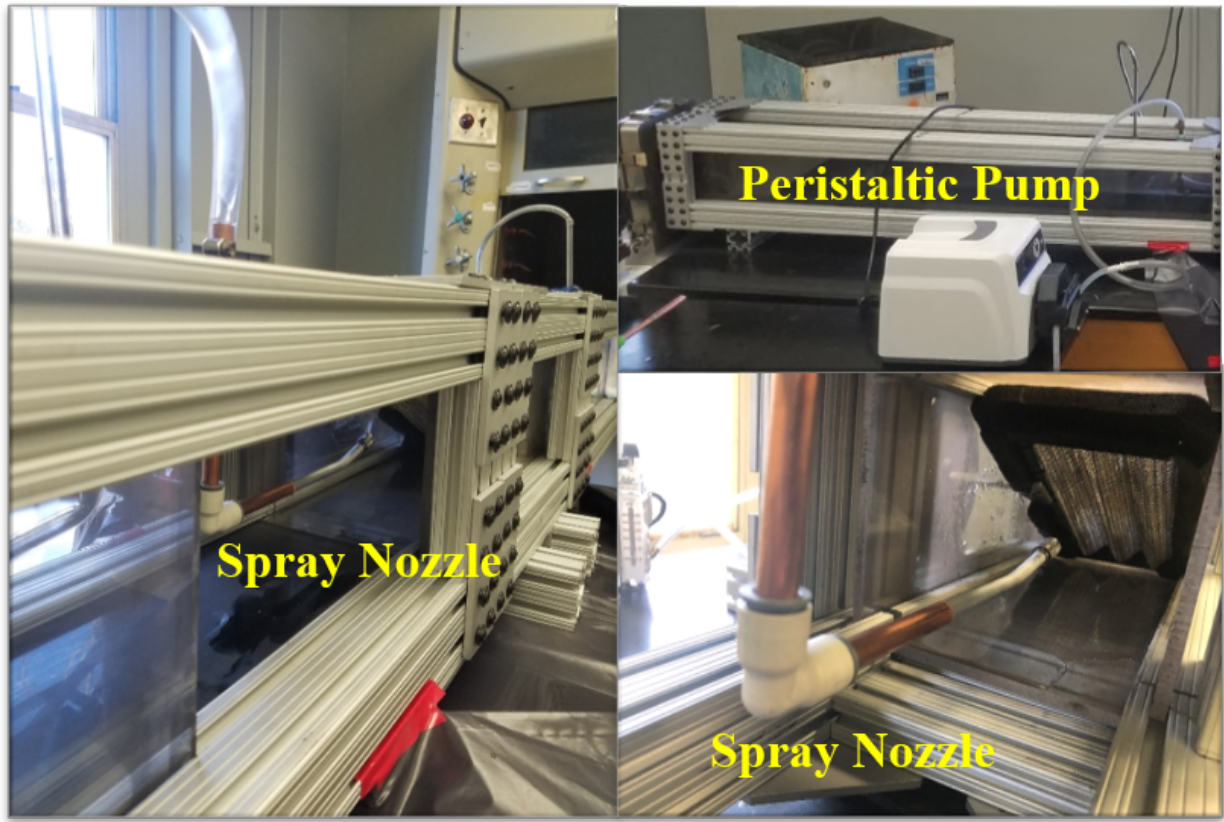


Figure 14. Components and location of water management system in the scrubber unit.

#### 4.2.7 Mesh and Shaker:

The filter mesh used in this study was a small section of an industrial-grade, steel-woven scrubber mesh used on continuous miners. The panel is approximately 6 mm thick with 14 layers of wire screen. Each wire screen has seven wires per centimeter with a wire diameter of 0.009 cm. The panel is tilted at an angle between 45 and 50 degrees and its face area is 0.074 m<sup>2</sup>.

During testing, the mesh was mounted to an electromechanical shaker (Brüel and Kjær Type 4809) by an aluminium rod and a clamp. A harmonic excitation was generated by a keysight 33500B model waveform generator and applied to the shaker through a Krohn-Hite Corp. 7500 amplifier for base excitation over a range of frequencies covering the fundamental mode of the mesh filter. To identify these fundamental modes, series of experiments were performed using Polytec OFV-505 Laser Doppler Vibrometer for measuring the amplitude of vibration of the oscillating mesh (Figs. 15a and 15b). The geometric properties of the mesh panel are presented in Fig. 15c. The desktop vibration test results, performed for the framed mesh (in Fig. 15b), showed that the optimal response of the mesh occurs in the range of 30 to 550 Hz frequency, from the lowest to highest. After installing the mesh in the tunnel, because of adding more constraints, the boundary conditions were changed and the optimal frequency range narrowed



down to 100 to 400 Hz. Therefore, 130 (low), 240 (mid) and 350 (high) Hz frequencies were selected for vibration of the mesh for the following experiments. The mesh panel was attached to the shaker and placed inside the mesh section of the wind tunnel (Fig. 16a). The aluminum rod, passing through a hole in the sidewall of the tunnel, transferred the motion of the shaker to the mesh panel (Fig. 16b) while the mesh panel was placed with a 40 degree angle in front of the air flow (Fig. 16c).

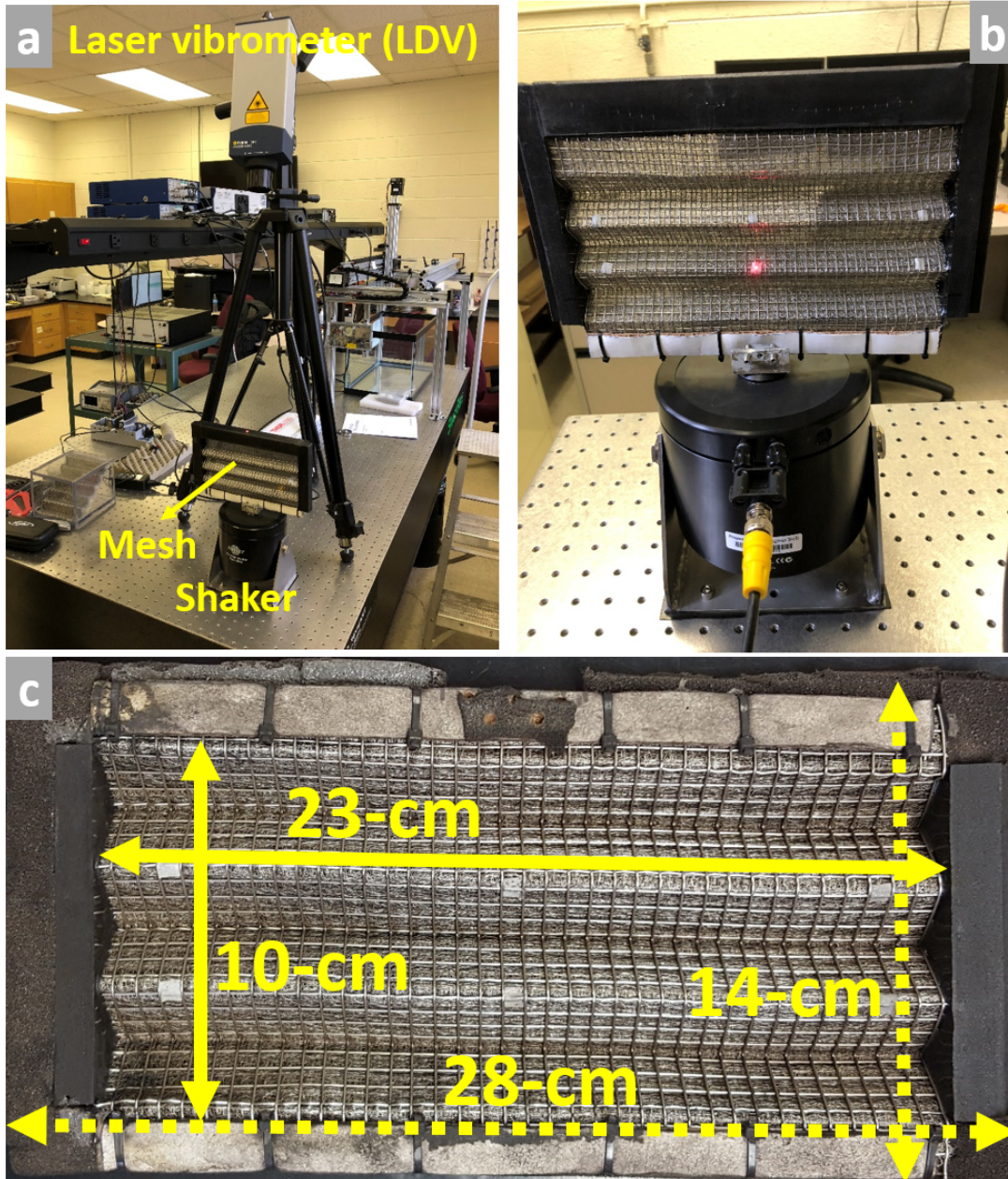


Figure 15. Experimental set-up for estimating the vibration resonance frequencies of the mesh panel with (a) arrangement of laser head with respect to the mesh, (b) close up view of the mesh mounted of the shaker and placement of the laser, and (c) dimensions of the mesh panel and its frame.

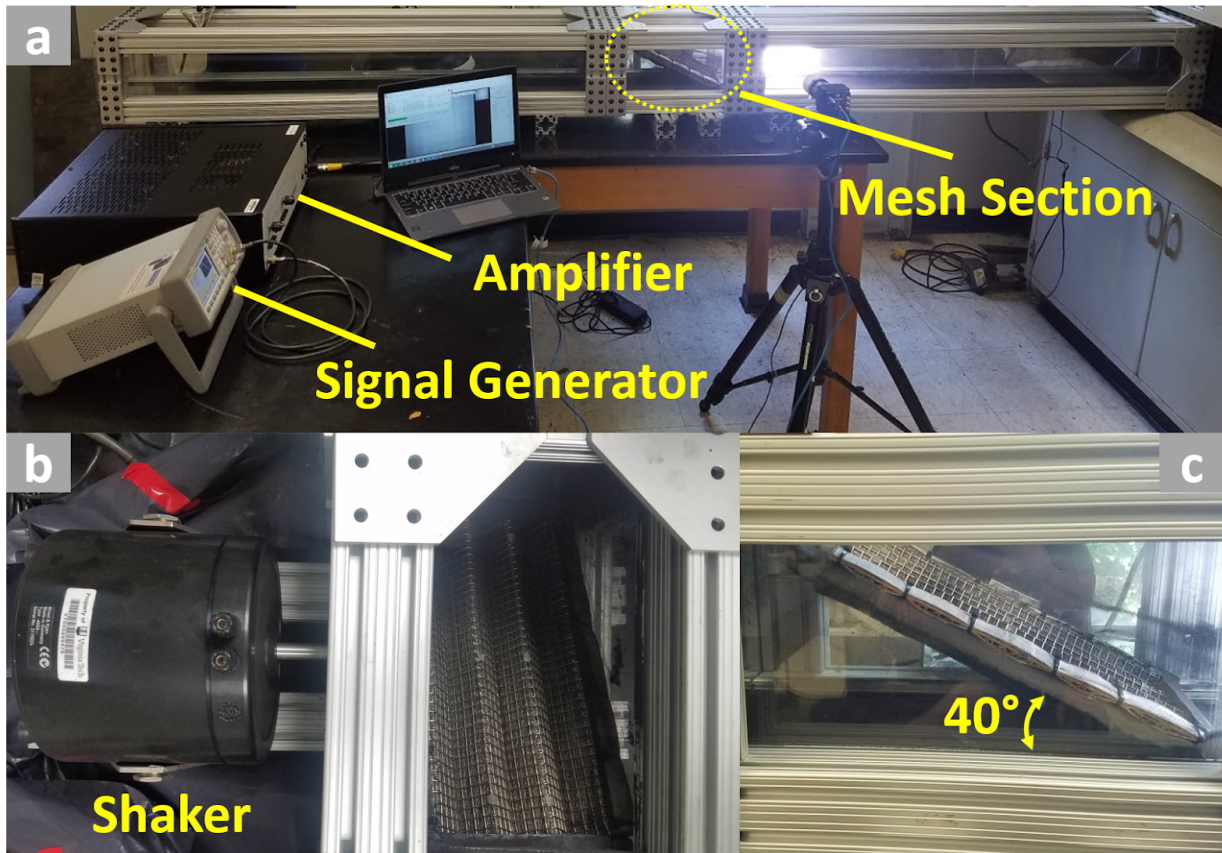


Figure 16. (a) The Location of the mesh panel section in the wind tunnel; (b) components of the mesh panel section and (c) the angle of mesh panel against the air flow inside the mesh section.

#### 4.2.8 Process monitoring system:

In order to identify, trace, and characterize the dust particles passing the filter mesh, a visual monitoring system process was implemented. This system consisted of a high-speed camera (Redlake N3 and Photron Fastcam Mini UX100), located right after the mesh section in the opposite side of a high intensity LED light panel and was operated by the PFV software (Fig. 17a and 17b). In addition, a marked piece of transparent tape, attached to a string and hung from the top of the tunnel through magnets, was used to locate and keep the exact focal area for each set of experiment runs, while also providing a calibration frame for analyzing the images (Fig. 17c). A pair of magnets were attached to microfiber cloths (Fig. 17d) and used to clean the side panel in front of the high-speed camera between every set of the experiments, to keep the field-of-view clear and improve the quality of images. In each experimental trial, a series of 1000 frames with frequency of 4000 fps were captured for 30 seconds after the injection of coal dust particles was initiated inside the wind tunnel.



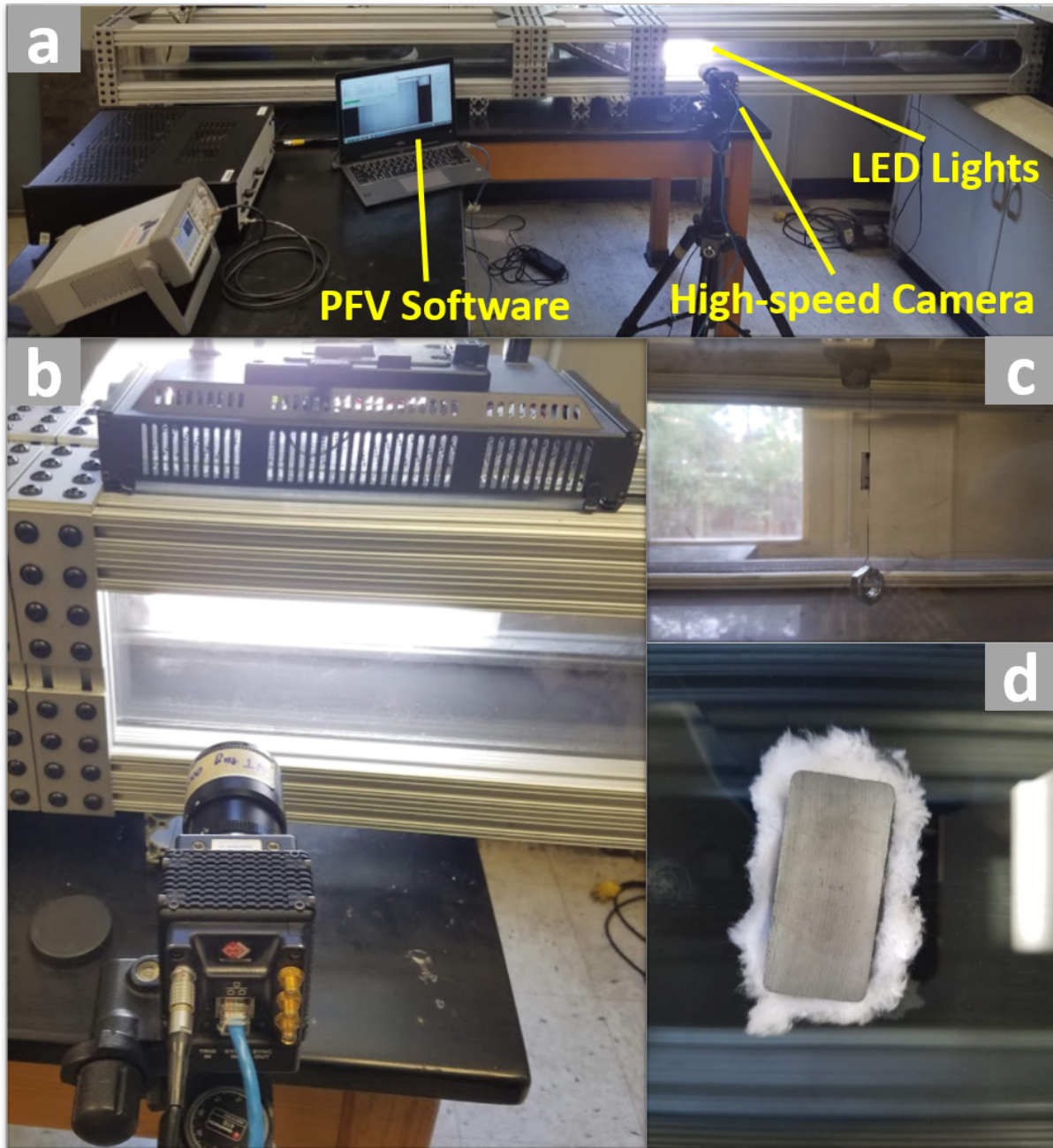


Figure 17. Components of the process monitoring system (a and b); Camera focus and calibration mechanism (c); and the cleaning component for improving the quality of images (d).

## 5.0. Proof of Concept Evaluation:

### 5.1 Materials and Methods:

#### 5.1.1 Coal dust characteristics:

The coal dust sample used throughout the experimental testing was obtained from Keystone Filler & Mfg. Co. Upon arrival, the sample was split into representative 1-lb lots using a Jones riffle splitter. Several representative lots were delivered to each project participant for use in individual testing activities. Baseline analyses showed that the sample has a low inherent moisture content of  $1.4\% \pm 0.10\%$  with a dry ash content of  $14.6\% \pm 0.04\%$ .

The particle size analysis of the surrogate dust was carried out using a Microtrac S3500 laser particle size analyzer. The particle size distribution data (Table 5) show that the top size is approximately 1 mm, and the majority of particles, approximately 78%, are coarser than 20 microns. Given this relatively coarse size, further grinding of the sample was necessary to properly simulate mining conditions. This finding prompted the addition of the jet mill to the wind tunnel design. Subsequent particle size analysis of the mill product showed that the jet mill significantly reduced the size of the feed material to 97% passing 20 micron. Fig. 18 shows the particle size distribution before and after milling. This finer product dust size was deemed adequate for proper demonstration testing.

Table 5. Particle size-by-size analysis of the original dust sample.

Particle size (micron)	Incremental (%)	Weight	Cumulative (%)	Weight
+500	0.85		0.85	
300x500	2.98		3.83	
200x300	2.32		6.15	
125x200	7.29		13.44	
75x125	19.55		32.98	
50x75	16.89		49.87	
35x50	13.76		63.63	
20x35	13.88		77.51	
10x20	12.91		90.42	
-10	9.58		100.00	

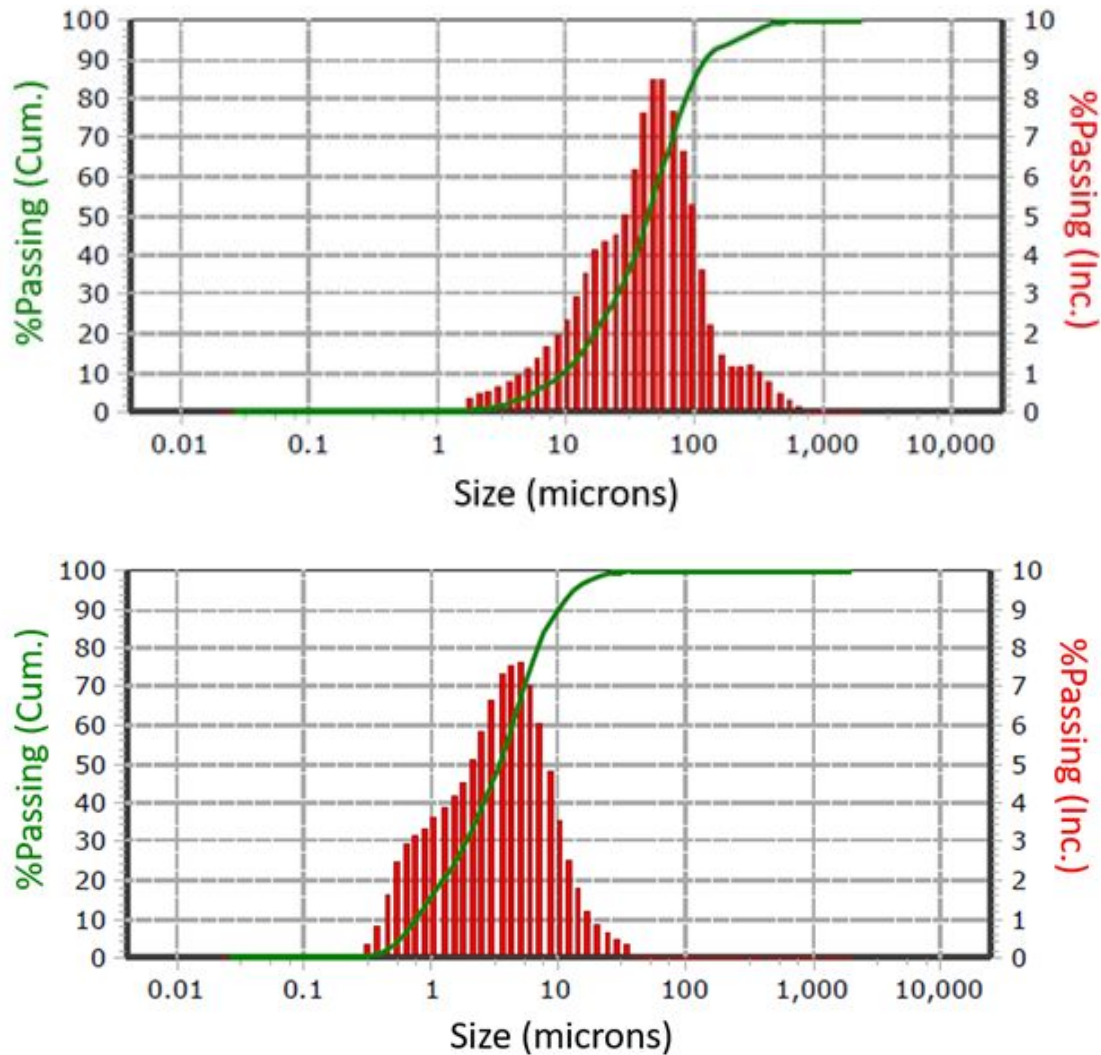


Figure 18. Particle size analysis of the original coal dust sample (top panel) and jet mill product (bottom panel)

### 5.1.2 Experimental Design

Experimental design methods and response surface techniques have been widely applied for process analysis to determine the relationship between process parameters and the performance efficiency indicators. These methodologies may employ full factorial, fractional factorial and central composite rotatable design. Of all three methodologies, the fractional factorial and central composite rotatable designs require fewer number of experiments and as a result they are considered time and cost efficient strategies. In the current study, the Box-Behnken design, as a fractional factorial experimental design method, was used to evaluate various factors affecting the collection efficiency of the bench-scale, proof-of-concept scrubber unit. The results of this



part of the study were then used to identify the optimal conditions under which the scrubber system suppressed the maximum mass of dust particles.

Box-Behnken designs, as rotatable or nearly rotatable designs, are employed based on three-level fractional factorial designs. The number of required experiments in a Box-Behnken design can be calculated as  $N = 2k(k - 1) + C_0$ , where  $k$  and  $C_0$  are the number of variables and the number of central points, respectively. In the current study, three parameters were selected for investigation: water flow rate, surfactant (Triton X-100) concentration, and vibration frequency of filter mesh. As a result, 12 unique tests, as well as three repeat trials (for the determination of the associated experimental error) were required to complete the experimental program. High, medium, and low levels for the three variable parameters are shown in Table 6. Additionally Fig. 19 graphically illustrates the design as a central point (C) with three interlocking  $2^2$  factorial designs. The test numbering in this illustration shows how the Box-Behnken design can be arranged into orthogonal blocks indicating the influence of the three parameters.

Based on the conclusions from the initial fundamental studies, water flow rate, surfactant (Triton X-100) concentration, and vibration frequency of the mesh panel were selected for investigation in proof-of-concept testing. Previous studies in the literature showed that the ratio of air flow rate to the water flow rate in the scrubber can be an influential factor in determining the scrubber collection efficiency [6]. To address this finding, the air flow rate was kept constant for all experimental runs, while the water flow rate was varied as an experimental parameter. Additionally, the fundamental studies (Section 4.1.2) showed that different contact angles can be produced from different surfactant concentrations (Triton X-100). As such, surfactant concentration was considered as another important factor to parametrically be evaluated in the proof-of-concept tests. Lastly, the impact of vibration frequency of the mesh panel in the dust collection procedure was demonstrated in Section 4.1.2. The initial testing indicated that the vibration of the mesh panel may significantly improve the dust suppression process. The individual and combinatory impact of these factors may significantly influence the dust collection efficiency of the scrubber unit performance. The experimental design was thus selected to fully reveal the effects of these factors on the collection efficiency and determine the optimal conditions under which the maximum collection efficiency is achieved.

Table 6. Parameter value ranges investigated in the Box-Behnken test program.

Parameter	Level		
	Low (-1)	Medium (0)	High (1)
Water Flow Rate (L/min)	0.175	0.225	0.275
Triton X-100 Concentration (mM)	0.00	0.05	0.10
Vibration Frequency (Hz)	130	240	350

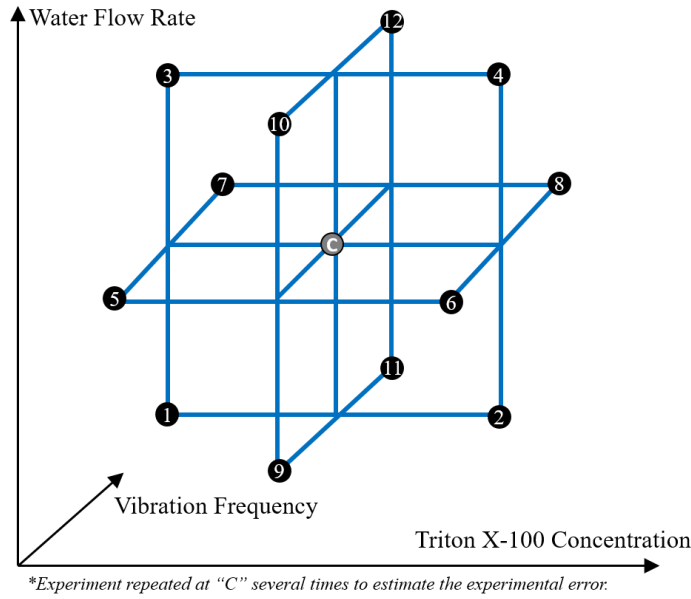


Figure 19. Graphical representation of a Box-Behnken design.

Following the results of this optimization study, additional dust suppression tests were conducted to establish the baseline scrubber performance under various conditions including: (1) a static mesh panel under dry conditions; (2) a static mesh panel under wet condition with no surfactant addition to water; and (3) a dynamic mesh panel vibrating at the highest level of frequency under dry conditions. Results from these three control tests were compared against the optimal test result found after the evaluation of parametric testing of the vibrating mesh. This final data set was used to evaluate the efficacy of vibrating mesh panels and prove the overall concept proposed in this project.

### 5.1.3 Laboratory Test Procedures

Table 7 shows the fixed test parameters and experimental values used during all tests. During the experimental runs, the surfactant concentration was first adjusted to the desired value for each experimental run. The axial fan was then turned on, and peristaltic pump and signal generator were operated at the specified level for each test trial. Next, the coal dust particles were continuously fed into the jet mill, and ultrafine particles were generated and injected into the wind tunnel at a constant rate. After achieving steady-state conditions, the upwind and downwind streams were sampled simultaneously for 2-minutes. Meanwhile, the high-speed camera recorded the flow of particles in the downwind section of the scrubber. After the completion of each test run, the sample cassettes were weighed, and the coal dust particles were removed from the Teflon filters and for further analyses. The collection efficiency associated with each test trial was then quantified as follows:

$$\text{Collection Efficiency (\%)} = \left(1 - \frac{\text{weight of downwind sample}}{\text{weight of upwind sample}}\right) \times 100$$

Table 7. Fixed operating parameters for the bench-scale testing.

Parameter	Value
Dust Feed Rate	27.5 gr/min
Upwind Flow Rate	157 CFM
Downwind Flow Rate	204 CFM
Sampling Time Interval	2 min
Sampling Pump Flow Rate	30 L/min

Finally, upwind and downwind dust samples were analyzed for particle size, shape, and composition using a MicroTrack particle size analyzer, an optical microscope, and a thermo-gravimetric analyzer.

#### **5.1.4 Experimental Data Analysis**

To evaluate the scrubber unit operational sensitivity, the experimental data were statistically analyzed and three dimensional plots were developed to show the relationship between operating factors (i.e. water flow rate, surfactant (Triton X-100) concentration, and vibration frequency of mesh panel) and collection efficiency.

To properly analyze the experimental data, the “lack of fit” test was conducted. Lack of fit compares the process variability (pure error) with the variation of results obtained from the statistical model (lack of fit), and a value greater than 0.10 is considered adequate (i.e. lack of fit is not significant.). In addition, the coefficient of determination ( $R^2$ ) and the adjusted coefficient of determination ( $R^2_{adj}$ ) were used to evaluate the reliability of the statistical analysis procedure for the results obtained from the proof-of-concept scrubber experiments.

Given the lack of fit, coefficient of determination, and adjusted coefficient of determination values, the statistical model with the lowest degree of error and the highest level of reliability was selected for the evaluation of the scrubber unit performance. Given the complexity of the statistical models, response surface plots (3D surface plots) were generated and used to effectively investigate the individual and combinatory effects of various operational parameters in estimating the collection efficiency of bench-scale scrubber units. According to these analyses, the optimal conditions were identified for maximizing the scrubber dust collection efficiency.

The statistical modeling and analyses results do not necessarily indicate that the models have predictive capacity. Since the statistical analysis was only based on a limited number of experimental runs, the model is not suitable for extrapolation beyond the current range of conditions. Nevertheless, this analysis provides a rigorous means of determining parameter

influences and exploring combinatory effects. The knowledge gained from this analysis may be later used to guide fundamental modeling efforts, but the development of a fully predictive model was beyond the scope of the current effort.

## 5.2 Experimental Results

The experimental test results obtained from the Box-Behnken design are shown in Table 8. These results describe the scrubber collection efficiency as a function of the three operational parameters. Overall, the wide range of collection efficiency values demonstrates the importance of operational factors in determining the performance of the bench-scale scrubber unit. For instance, while the scrubber unit was capable of suppressing over 75% of dust particles in Trial #12, slight changes in the level of water flow rate, surfactant concentration, and vibration frequency dramatically dropped the collection efficiency to nearly 20% in Trials #4 and #8. Moreover, the comparison between repeat experimental trials (i.e. C1, C2, and C3) demonstrates the significance of controlling the fixed operational parameters in the propagated pure error in the experimental program. While all three repeat trials were conducted under identical levels of water flow rate, surface concentration, and vibration frequency, it is speculated that the improper control of air flow rate in each trial resulted in different values of collection efficiency.

To effectively evaluate the individual and combinatory effects of operational parameters in estimating the collection efficiency, a 2 factor interaction model (2FI), with the “Lack of Fit F-value” of 0.27, was selected. This value of lack of fit implies that the lack of fit is not significant relative to the pure error in the experimental program. Considering the complexity of the model, the effects of operating parameters were difficult to directly interpret from the empirical relationship. Alternatively, the relationship between collection efficiency and the performance variables are illustrated in a series of 3-D response surface plots (Fig. 20).

Evaluation of the response surface plots in Fig. 20 indicate that the individual effects of all three operational parameters, when compared with their interactive influences, were insignificant for the estimation of collection efficiency values. For example, as shown in panel A of Fig. 20, an increase in the water flow rate may result in either improving or diminishing the scrubber performance efficiency based on the level of surfactant concentration and vibration frequency. Similar trends for all operational factors are observed in the 3-D surface plots indicating the insignificance of the individual impacts of these parameters.

On the other hand, analysis of combinatory impacts of operational variables reveals that the maximum collection efficiency often occurred under the highest level of water flow rate and vibration frequency when maintaining the zero concentration of Triton X-100. This observation is demonstrated in the red-colored surfaces in the right panel of Fig. 20a and 20c as well as the left panel of Fig. 20b. According to the results of the experimental program (Table 8 and Fig 20), an individual dust suppression test was conducted under optimal conditions (water flow rate (+1 or 0.275 L/min); surfactant concentration (-1 or 0 mM); and vibration frequency (+1 or 350 Hz)) to further evaluate the importance of operational parameters under study. The scrubber performance efficiency under optimal conditions was then compared against the ones resulted from distinct experimental runs in dry and wet environments with static and dynamic mesh

panels. Table 9 summarizes the performance of scrubber under various operational parameters in distinct individual dust collection experiments.

The comparison between collection efficiency values achieved from the individual experiments further illustrates the importance of the interactive effects of water flow rate and vibration frequency on the performance of the scrubber unit. As shown in Table 9, the maximum collection efficiency of over 90% was achieved when the scrubber unit was operated under optimal conditions. The comparison between experimental trials under optimum conditions and dry-no vibration environment indicates the significant combinatory effect of water flow rate and vibration frequency in improving the performance of the scrubber unit (as collection efficiency was improved by 14%). Moreover, these data show that the individual effect of water flow rate on the scrubber performance could be more significant in improving the scrubber performance, when compared with the impact of vibration frequency factor. Maintaining the water flow rate at the highest level resulted in an improvement in the collection efficiency factor (from 76.60% to 81.54%) while vibration of the mesh panel in the dry environment caused a reduction of 15% in the collection efficiency (from 76.60% to 62.38%).

Table 8: Summary of collection efficiency achieved using the bench-scale proof-of-concept scrubber unit

Trial Order#	Parameters			Collection Efficiency (%)
	Water Flow Rate (L/min)	Surfactant Concentration (mM)	Vibration Frequency (Hz)	
1	0.175	0.00	240	27.02
2	0.175	0.10	240	61.17
3	0.275	0.00	240	51.54
4	0.275	0.10	240	19.71
5	0.225	0.00	130	58.25
6	0.225	0.10	130	42.74
7	0.225	0.00	350	62.61
8	0.225	0.10	350	18.52
9	0.175	0.05	130	48.16
10	0.275	0.05	130	32.06
11	0.175	0.05	350	38.78
12	0.275	0.05	350	75.70

C1	0.225	0.05	240	60.48
C2	0.225	0.05	240	46.04
C3	0.225	0.05	240	64.17

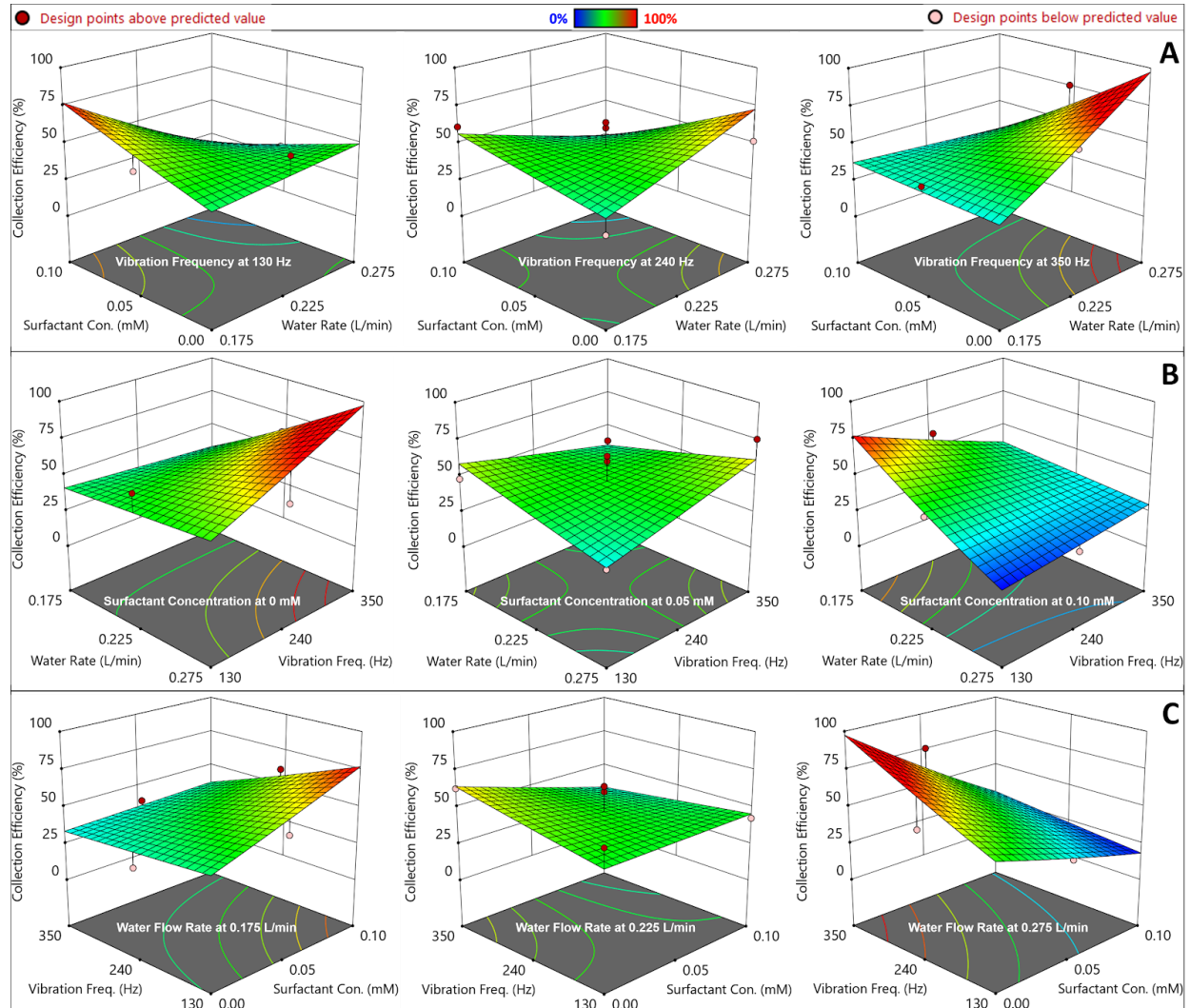


Figure 20. Predicted interactive effects of (A) surfactant concentration and water flow rate at different vibration frequency values; (B) water flow rate and vibration at different levels of surfactant concentration; and (C) surfactant concentration and vibration frequency at distinct levels of water flow rate.

Table 9. Collection efficiency values achieved under optimal conditions and dry/wet environment with static and dynamic mesh panel

Individual Trial	Parameters			Collection
Description	Water	Surfactant	Vibration	Efficiency
	Flow Rate (L/min)	Concentration (mM)	Frequency (Hz)	(%)
Optimal Trial	0.275	0	350	90.48
Dry-No Vibration	0.000	0	0	76.60
Dry-With Vibration	0.000	0	350	62.38
Wet-No Vibration	0.275	0	0	81.54

To further evaluate the influential parameters on the performance of the scrubber unit, an optical microscopy analysis was conducted on the upwind and downwind samples. Fig. 21 shows a characteristic image from these two samples. As shown in the images, both micrographs show very similar particle shapes (nearly spherical), indicating that the mesh panel does not selectively segregate particular particle shapes. Given this observation, no further quantitative assessment of particle shape was conducted.

Finally, the upwind and downwind samples were both subjected to ash analysis to determine if vibrating filter mesh selectively captures particles of a particular composition. Results from this analysis show a very similar ash content (16.78% and 17.17% ash content in upwind and downwind samples, respectively) indicating that selective separation is not occurring. Given this finding, no further quantitative assessment of selective separation was conducted.

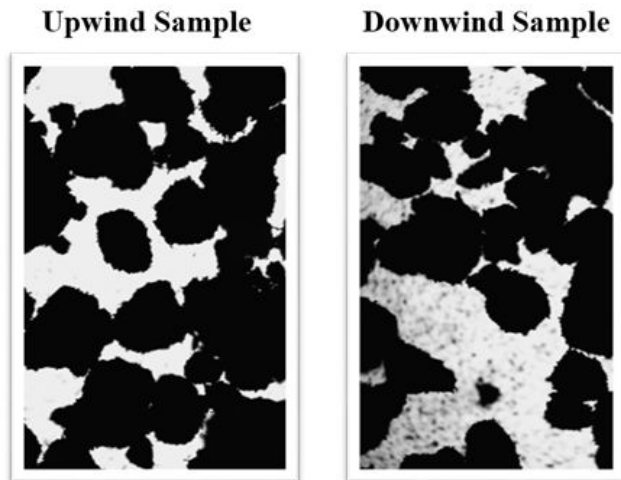


Figure 21. Optical microscopy images showing the shape of dust particles in upwind and downwind samples.

Following each experimental trial, a comprehensive particles size analysis was performed on

individual upwind and downwind samples to investigate the performance of scrubber unit in different size fractions. While the detail size-by-size analysis and distribution plots are presented in the appendices section (Section 7.0), Table 10 summarizes the collection efficiency of individual test trials for three size fractions. Overall, these results show that the dust particle size is not a significant factor in defining the collection efficiency.

Table 10. Summary of the particle size analysis and collection efficiency data for the experimental test runs and the test conducted under optimal conditions.

Trial Order #1						Trial Order #2				
Size (μm)	Upwind Sample Wt.		Downwind Sample Wt.		Collection Efficiency	Upwind Sample Wt.		Downwind Sample Wt.		Collection Efficiency
	%	gr	%	gr	%	%	gr	%	gr	%
+22	17.33	0.007	20.41	0.006	14.01	28.38	0.017	18.11	0.004	75.22
11×22	39.79	0.016	38.17	0.011	29.99	31.44	0.018	32.73	0.007	59.58
-11	42.89	0.017	41.42	0.012	29.52	40.18	0.023	49.16	0.011	52.49
Total	100.00	0.040	100.00	0.029	27.02	100.00	0.058	100.00	0.023	61.17
Trial Order #3						Trial Order #4				
Size (μm)	Upwind Sample Wt.		Downwind Sample Wt.		Collection Efficiency	Upwind Sample Wt.		Downwind Sample Wt.		Collection Efficiency
	%	gr	%	gr	%	%	gr	%	gr	%
+22	14.49	0.008	27.11	0.007	9.30	16.32	0.009	18.90	0.008	7.00
11×22	31.27	0.016	38.13	0.010	40.92	27.33	0.015	30.99	0.014	8.97
-11	54.24	0.028	34.76	0.009	68.94	56.35	0.031	50.11	0.022	28.59
Total	100.00	0.052	100.00	0.025	51.54	100.00	0.055	100.00	0.044	19.71



Table 10 (continued). Summary of the particle size analysis and collection efficiency data for the experimental test runs and the test conducted under optimal conditions.

Trial Order #5						Trial Order #6				
Size (μm)	Upwind Sample Wt.		Downwind Sample Wt.		Collection Efficiency	Upwind Sample Wt.		Downwind Sample Wt.		Collection Efficiency
	%	gr	%	gr	%	%	gr	%	gr	%
+22	22.88	0.015	13.22	0.004	75.88	18.47	0.002	17.23	0.001	46.58
11×22	41.13	0.027	39.54	0.011	59.86	23.14	0.003	23.96	0.002	40.71
-11	36.00	0.024	47.25	0.013	45.19	58.39	0.007	58.81	0.004	42.33
Total	100.00	0.066	100.00	0.028	58.25	100.00	0.012	100.00	0.007	42.74
Trial Order #7						Trial Order #8				
Size (μm)	Upwind Sample Wt.		Downwind Sample Wt.		Collection Efficiency	Upwind Sample Wt.		Downwind Sample Wt.		Collection Efficiency
	%	gr	%	gr	%	%	gr	%	gr	%
+22	13.62	0.006	14.61	0.003	59.89	14.28	0.002	16.12	0.002	8.02
11×22	36.43	0.017	40.88	0.007	58.03	32.40	0.004	29.68	0.003	25.36
-11	49.95	0.023	44.51	0.008	66.68	53.32	0.007	54.20	0.006	17.17
Total	100.00	0.047	100.00	0.018	62.61	100.00	0.014	100.00	0.011	18.52
Trial Order #9						Trial Order #10				
Size (μm)	Upwind Sample Wt.		Downwind Sample Wt.		Collection Efficiency	Upwind Sample Wt.		Downwind Sample Wt.		Collection Efficiency
	%	gr	%	gr	%	%	gr	%	gr	%
+22	12.01	0.006	11.34	0.003	51.08	15.82	0.002	16.49	0.001	29.18
11×22	33.03	0.017	27.42	0.007	56.96	26.34	0.003	28.25	0.003	27.14
-11	54.96	0.028	61.24	0.016	42.23	57.85	0.008	55.27	0.005	35.09
Total	100.00	0.052	100.00	0.027	48.16	100.00	0.013	100.00	0.009	32.06

Table 10 (continued). Summary of the particle size analysis and collection efficiency data for the experimental test runs and the test conducted under optimal conditions.

Trial Order #11						Trial Order #12				
Size ( $\mu\text{m}$ )	Upwind Sample Wt.		Downwind Sample Wt.		Collection Efficiency	Upwind Sample Wt.		Downwind Sample Wt.		Collection Efficiency
	%	gr	%	gr	%	%	gr	%	gr	%
+22	27.54	0.020	6.20	0.003	86.22	26.50	0.018	29.24	0.005	73.20
11 $\times$ 22	20.15	0.015	10.50	0.005	68.09	30.31	0.020	27.61	0.005	77.87
-11	52.32	0.038	83.30	0.037	2.52	43.18	0.029	43.15	0.007	75.72
Total	100.00	0.074	100.00	0.045	38.78	100.00	0.068	100.00	0.016	75.70
Trial C1						Trial C2				
Size ( $\mu\text{m}$ )	Upwind Sample Wt.		Downwind Sample Wt.		Collection Efficiency	Upwind Sample Wt.		Downwind Sample Wt.		Collection Efficiency
	%	gr	%	gr	%	%	gr	%	gr	%
+22	14.76	0.004	11.81	0.001	68.38	24.92	0.017	29.75	0.011	35.57
11 $\times$ 22	22.61	0.006	21.14	0.002	63.07	33.78	0.023	30.45	0.011	51.37
-11	62.63	0.016	67.06	0.007	57.69	41.30	0.028	39.80	0.015	48.00
Total	100.00	0.025	100.00	0.010	60.48	100.00	0.068	100.00	0.037	46.04
Trial C3						Optimal Trial				
Size ( $\mu\text{m}$ )	Upwind Sample Wt.		Downwind Sample Wt.		Collection Efficiency	Upwind Sample Wt.		Downwind Sample Wt.		Collection Efficiency
	%	gr	%	gr	%	%	gr	%	gr	%
+22	39.12	0.024	8.50	0.002	92.21	19.32	0.018	16.88	0.001	91.68
11 $\times$ 22	7.85	0.005	11.79	0.003	46.18	46.57	0.043	30.88	0.003	93.68
-11	53.04	0.033	79.71	0.018	46.15	34.11	0.032	52.24	0.005	85.41
Total	100.00	0.061	100.00	0.022	64.17	100.00	0.092	100.00	0.009	90.48

As a follow-on analysis, we measured the number and velocity of particles passing the vibrating mesh using high-speed video. In Fig. 22, we overlaid image sequences over 5 ms for three different vibration frequencies (130, 240, and 350 Hz). Each color represents a trajectory of different particle individuals. Since our field-of-view is only about 2.5 cm, small particles ( $<100\ \mu\text{m}$ ) are detectable. Due to a high frame rate of the camera, we can continuously track each particle over time and calculate its velocity. In Fig. 22a, many particles were passed through the filter when the vibration frequency is low. It indicates that tests with a low frequency vibration allow many particles passed through, whereas tests with a high frequency filter out a lot of particles.

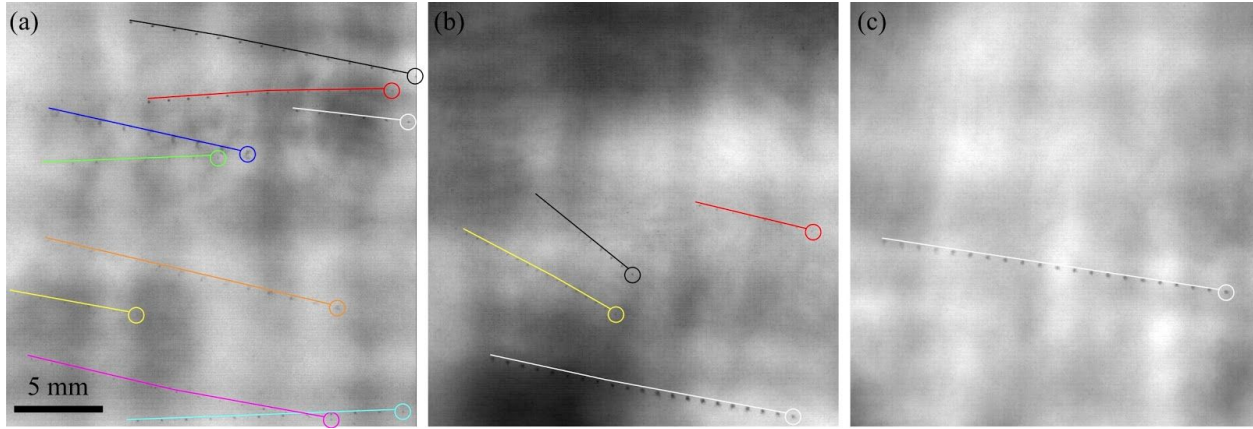


Figure 22. Three images show particle trajectories at different vibration frequencies over a time window of 5 ms: (a) 130, (b) 240, and (c) 350 Hz.

Furthermore, we counted the number and speed of particles over 14 different cases and plotted the results in Fig. 23. As shown in Fig. 23a, the number of particles decreases as the vibration frequency is increased. The same trend has been observed in the overlapping images above and the particle collection method in the previous section. This result further suggests that the particles are unlikely to pass through the filter at a higher frequency. Fig. 23b shows the velocity of particles at different frequencies. The particle velocity represents the air-flow speed too since the particle size is small and its corresponding Stokes number is less than 1. As shown, the particle speeds of three different vibrating frequencies are in a similar range, which shows that air flow speed was not affected by the vibration. In other words, we can maintain a similar range of air flow with mesh vibration.

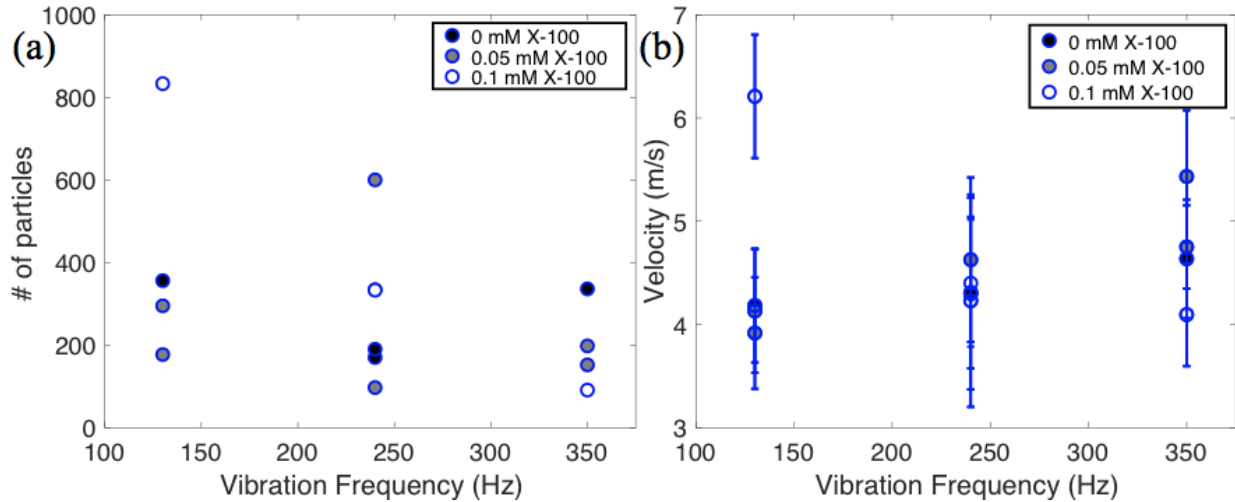


Figure 23. (a) the number of uncollected particles by a mesh versus the vibration frequency. (b) the particle velocity vs. the vibration frequency.

### 5.3 Experimental Challenges

The design and fabrication of the proof-of-concept scrubber, with a 152 mm x 152 mm cross-section, created considerable technical challenges for the construction of sampling and water supply system. Given the cross-section dimension of the wind tunnel, sampling probes were positioned in a singular point at the centerline of the upwind and downwind sections. Collecting samples from an individual point inside the tunnel may cause a considerable level of error as the sample may not be the true representation of the dust particles flowing in each section. An effective, reliable, and real-time sampling system that captured samples from several points in the upwind and downwind ductwork sections may minimize the associated error with the sampling procedure, thereby enhancing the reliability of data. Furthermore, the cross-section dimension of the wind tunnel indirectly determines and control the number of spray nozzles used in the scrubber and their diameter. The available spray nozzle alternatives may fail to produce a desirable water flow rate and pressure required to maximize the dust collection efficiency.

Another note regarding our results is related to clogging problem. Clogging is one of the major problems of meshes used in the field. However, we cannot directly measure or quantify clogging on our mesh. Two reasons; (1) Our test is run for 3 mins, and we observed clogging in the mesh. However, clogging happens in inner layers, which cannot be visualized easily. (2) From the particle tracking method described in page 27 and 28, we can infer the clogging effect. As shown in Fig. 23b, we can see that the particle velocity (same as air flow speed) does not change much as the vibration frequency changes. It means that the air flow is not blocked in all of our tests. In the future, we might need to develop another means to check the clogging in the mesh such as X-ray imaging technique.

## 6.0. Technology Readiness Assessment:

For reference, the descriptions of the technology readiness levels used in this study are provided in Table 11. These have been adapted from the US Department of Energy - National Energy Technology Laboratory. These descriptions will be used to characterize the technology readiness of the proposed technology.

Table 11. TRL Descriptions (National Energy Technology Laboratory)

TRL	Definition	Description
1	Basic principles observed and reported	Core Technology Identified. Scientific research and/or principles exist and have been assessed. Translation into a new idea, concept, and/or application has begun.
2	Technology concept and/or application formulated	Invention Initiated. Analysis has been conducted on the core technology for practical use. Detailed analysis to support the assumptions has been initiated. Initial performance attributes have been established.
3	Analytical and experimental critical function and/or characteristic proof-of-concept validated	Proof-of-Concept Validated. Performance requirements that can be tested in the laboratory environment have been analytically and physically validated. The core technology should not fundamentally change beyond this point. Performance attributes have been updated and initial performance requirements have been established.
4	Basic technology components integrated and validated in a laboratory environment	Technology Validated in a Laboratory Environment. The basic technology components have been integrated to the extent practical (a relatively low-fidelity integration) to establish that the pieces will work together, and validated in a laboratory. Performance attributes and requirements updated.
5	Basic technology components integrated and validated in a relevant environment	Technology Validated in a Relevant Environment. Basic technology component configurations have been integrated and validated in a relevant environment. Integration is similar to the final application in most respects. Data sufficient to support planning and design of the next TRL test phase have been obtained. Performance attributes and requirements have been updated.
6	Prototype validated in a relevant environment	Prototype Validated in Relevant Environment. A high-fidelity prototype, integrated to the extent practical, has been validated in a relevant environment. Data sufficient to support planning and design of the next TRL test phase have been obtained. Performance attributes and requirements have been updated.
7	Fully integrated prototype validated in an operational system	Fully Integrated Prototype Validated in Operational Environment. A high-fidelity unit, which addresses all scaling issues, has been built and tested in an operational environment. Data sufficient to support planning and design of the next TRL test phase have been obtained. Performance attributes and requirements have been updated.
8	Actual technology successfully commissioned in an operational system	Actual Technology Commissioned. The actual technology has been successfully commissioned for its target commercial application. In almost all cases, this TRL represents the end of true system development.
9	Actual technology operated over the full range of expected operational	Commercially Operated. The actual technology has been successfully operated long-term and has been demonstrated in an operational system, including (as applicable) shutdowns, startups, system upsets, weather ranges, and turndown

conditions

conditions. Technology risk has been reduced so that it is similar to the risk of a commercial technology if used in another identical plant.

During this project, the research team integrated and synthesized data from the fundamental studies and shakedown tests to design and construct a bench-scale, proof-of-concept scrubber system. Prior to the project, the technology readiness of the system was TRL 1, as the basic principles had been observed and reported. As described in the initial proposal, vibrating meshes should have a theoretical higher capture efficiency due to increasing effective area of contact between particles and the mesh. As shown in the results, we can see that the particle-capturing rate increases with vibration frequency range which covers the resonance frequency of the mesh. Although there is no explicit limit in vibration frequency, the resonance condition is crucial as the mesh elements experience large amplitude deformation at the resonance condition.

Throughout the initial six months of the project, fundamental studies were conducted on two key project elements, the role of surfactant in promoting water-particle collisions, and the role of vibrating meshes in intercepting particles. Through these fundamental assessments, the technology readiness was increased to TRL 2, as these studies largely confirmed the initial hypotheses and identified optimal test conditions to pursue.

During the final twelve months of the project, the data and information gained in the fundamental studies was used to design a small-scale testing apparatus to evaluate the capture performance in a laboratory environment. As shown in Section 5.2, the experimental data from the test campaign has largely confirmed the hypothesis and show that, when operated under optimal conditions, vibrating meshes can increase the dust capture performance of a standard flooded bed dust scrubber. While the technology does show promise, further laboratory testing is needed to validate and optimize the technical performance under different operational conditions and for longer test durations. Given these promising findings as well as the limitations of the current testing program, the current TRL level is 3.

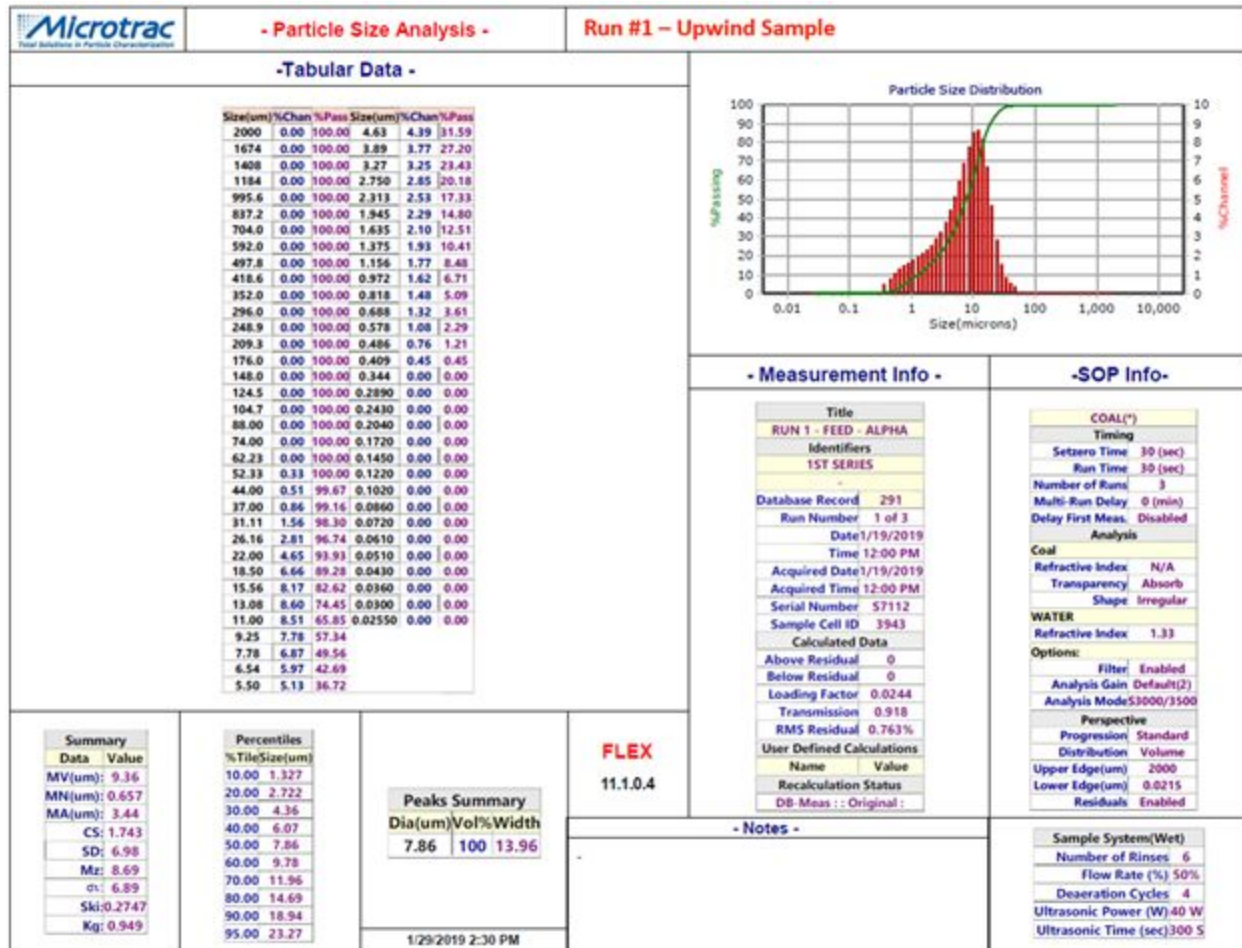
The data that was collected in our exploratory project can be used to design prototype components or a prototype system that can be deployed in a relevant environment, such as NIOSH's Dust Gallery. This continued scale-up testing and verification will seek to advance the technology to TRL 5-6. Considering the technical limitations and challenges experienced in the current study, the following items are recommended for the scale-up stage of this study:

1. The fabrication of the vibrating mesh section, as a key element of the wind tunnel, will be the first stage of the pilot-scale scrubber unit design. The mesh box will contain an industrial mesh panel, a properly sealed structure allowing the vibration of the mesh at desirable frequency levels, and an innovative design to attach the mesh panel to the vibration shaker.
2. Based on the dimensions of the mesh panel, an efficient water management system will be designed to properly spray water droplets on the surface of the mesh. Water spray nozzles will be capable of producing water flow rates at a wide range of pressures.
3. A reliable, industry standard, sampling methodologies will be followed to collect samples from different heights inside the wind tunnel and conduct real-time mass and size measurements of dust particles in a simulated coal mining operation condition.

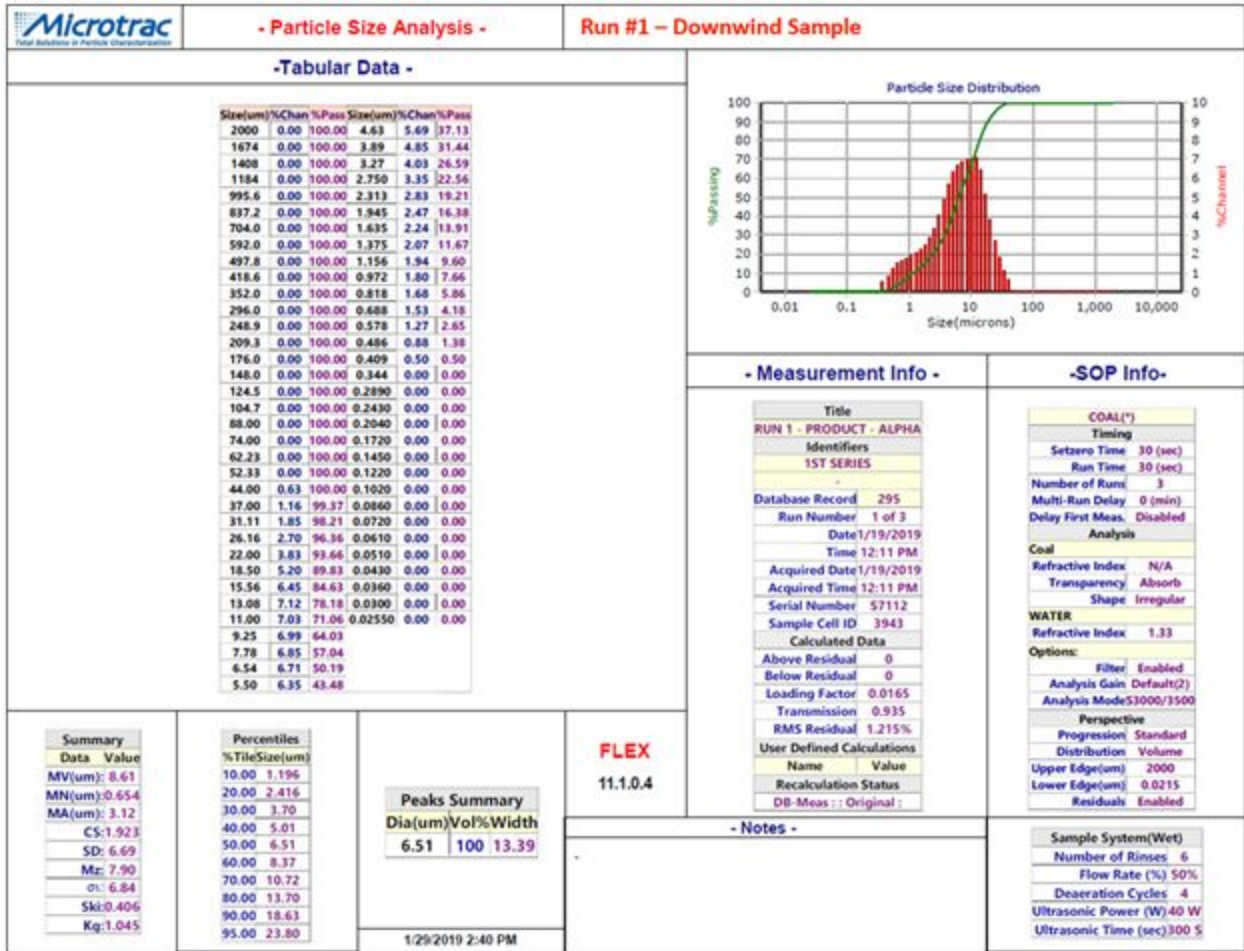
4. According to the specifications of the wind tunnel, a real-time air flow rate measurement system will be designed to meticulously monitor and control the air pressure at different sections of the scrubber unit. Also, surface treatments on windshields can avoid errors in flow measurements using a high-speed camera.
5. The design parameters alongside operational factors will be specified according to the real-world mine dust scrubbers. Fabrication of such a pilot-scale unit and an effective control system may result in the development of comprehensive models to adequately predict the performance of the scrubber under distinct operational conditions.

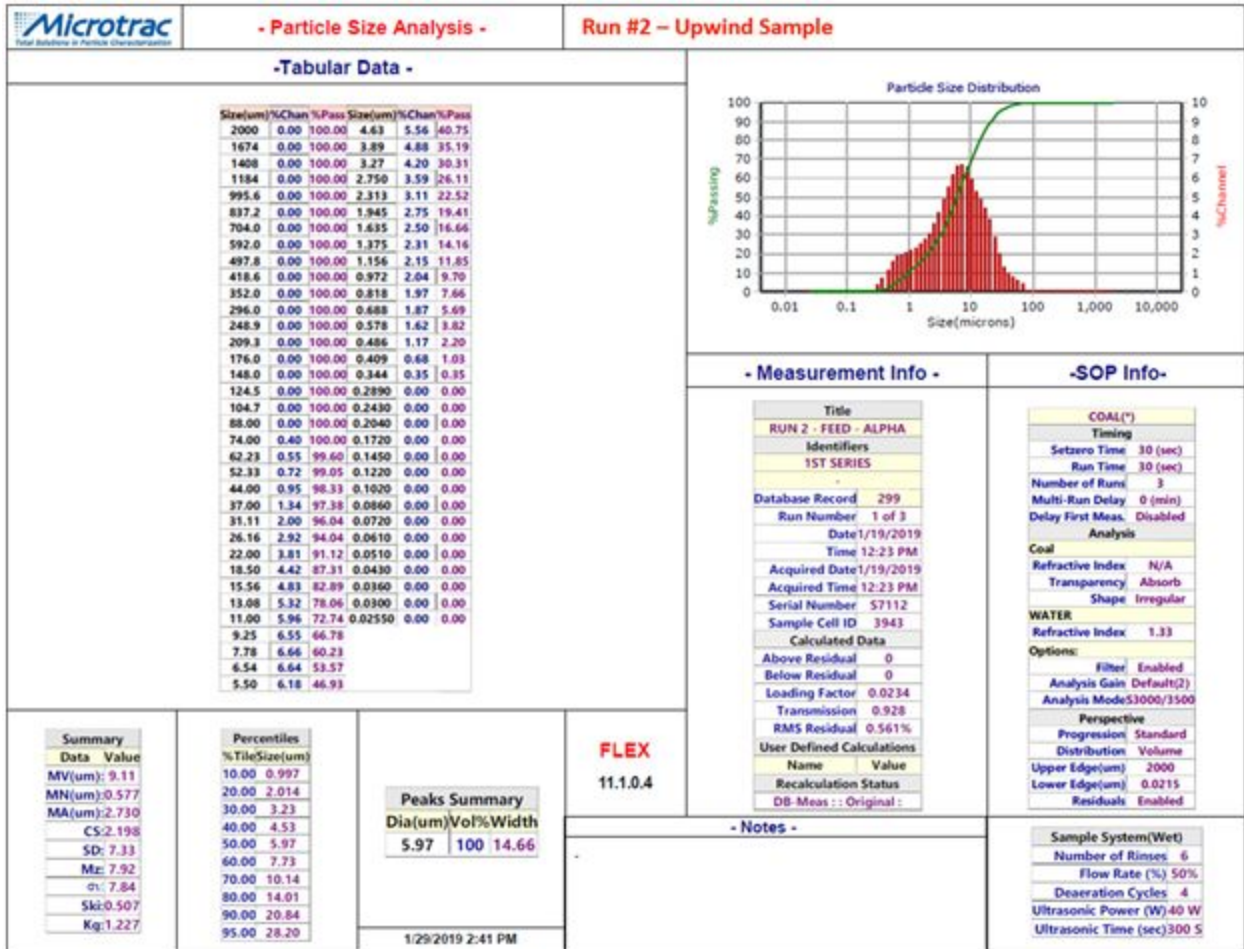
## 7.0. Appendices:

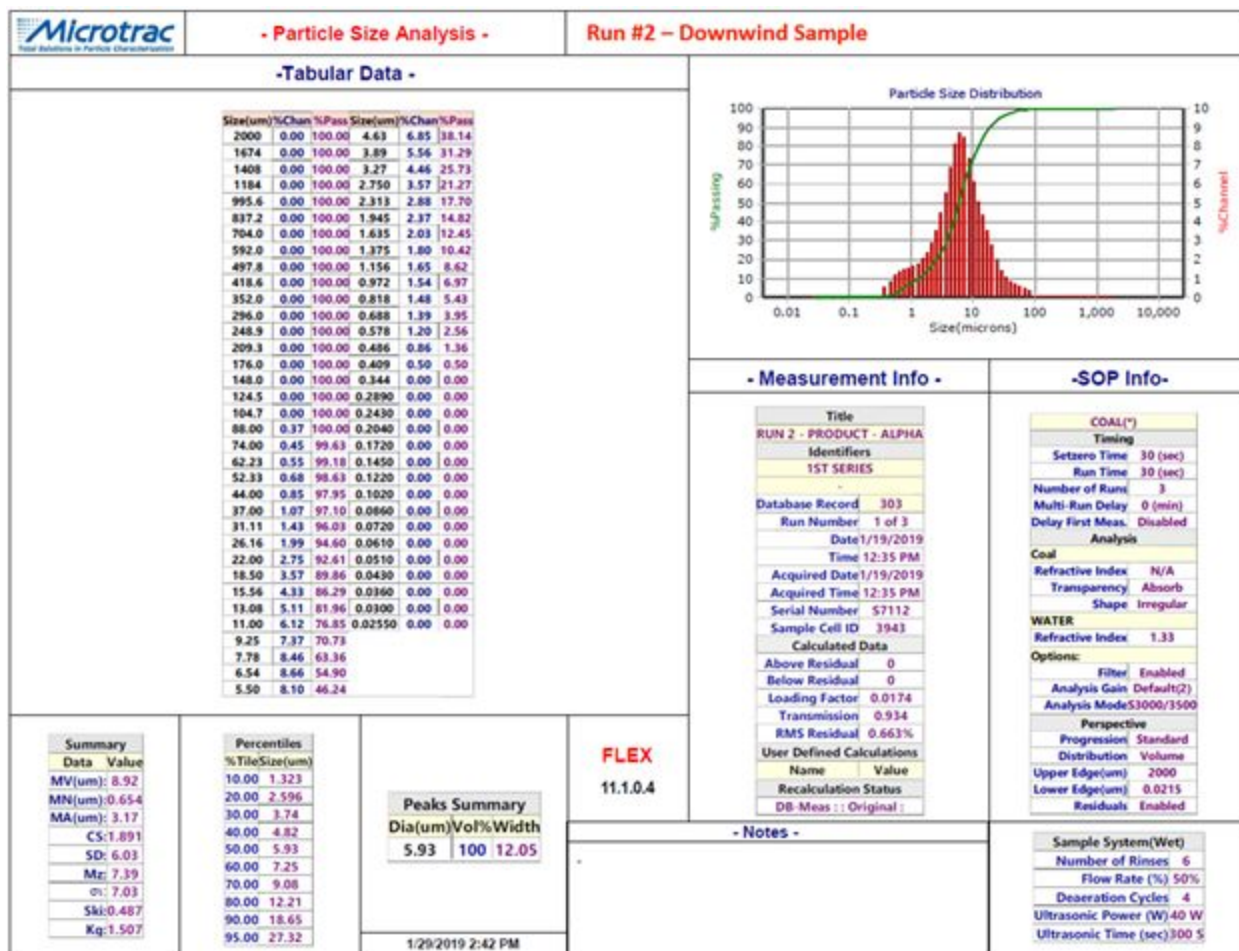
### 7.1 Particle Size-by-Size Analysis Data:

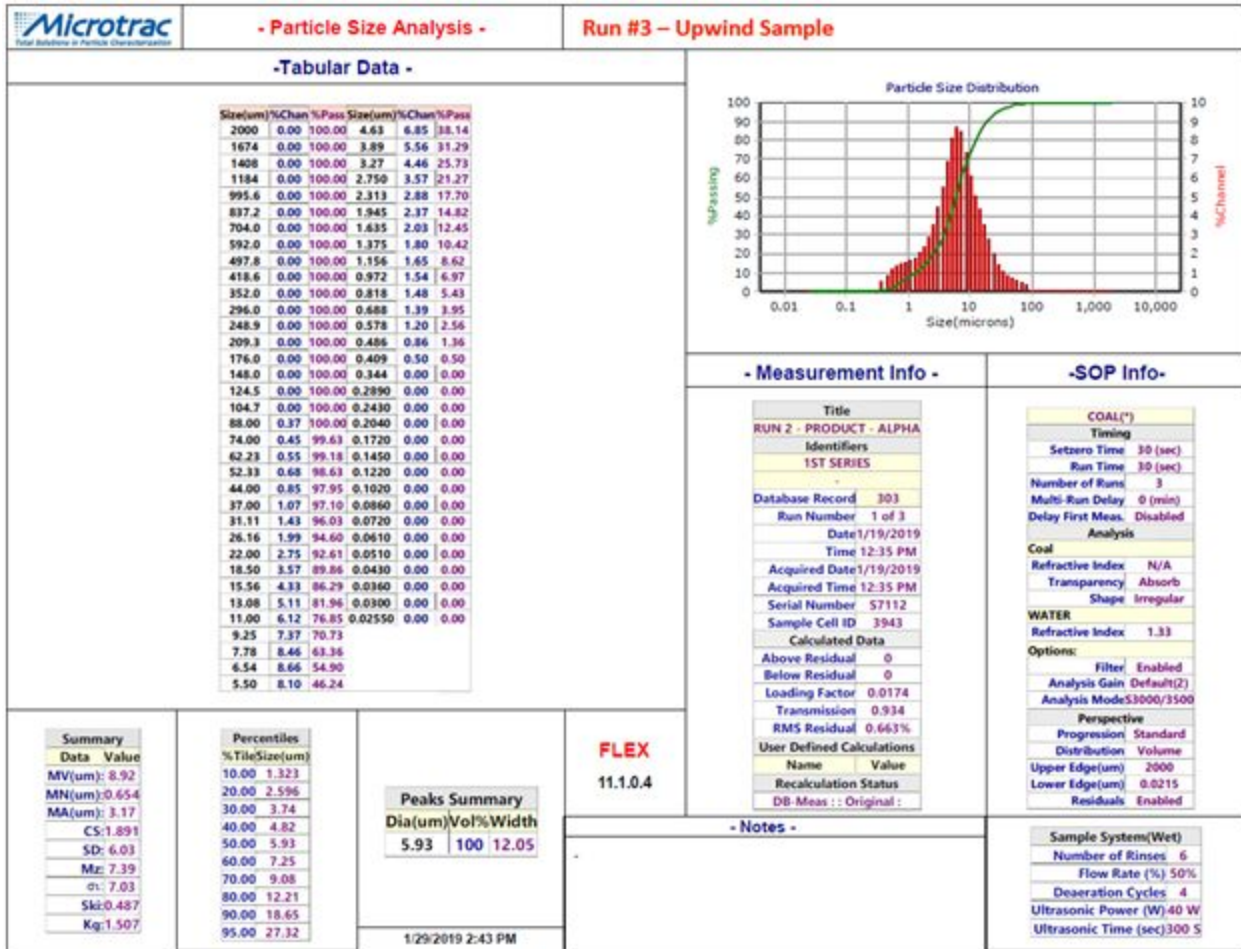




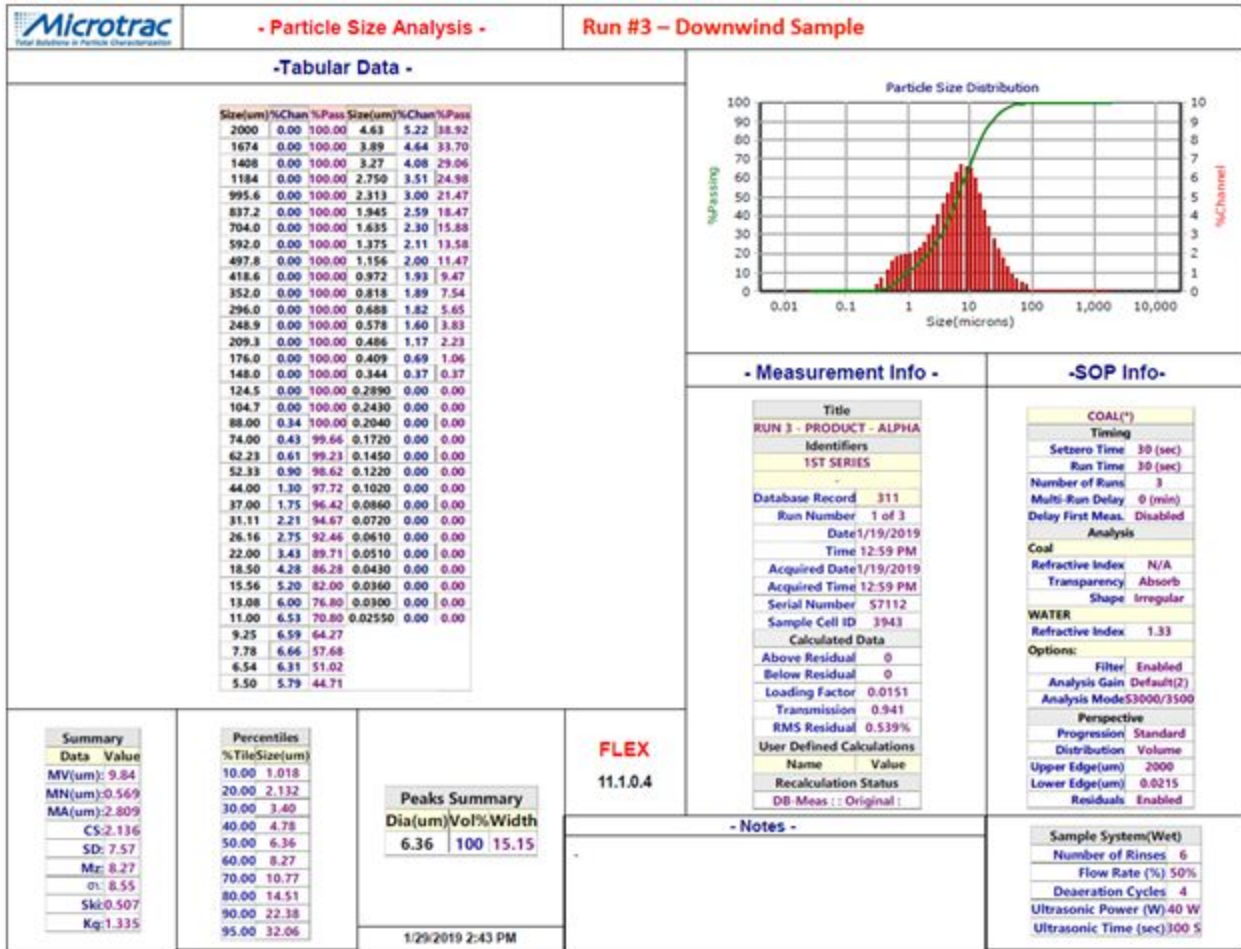


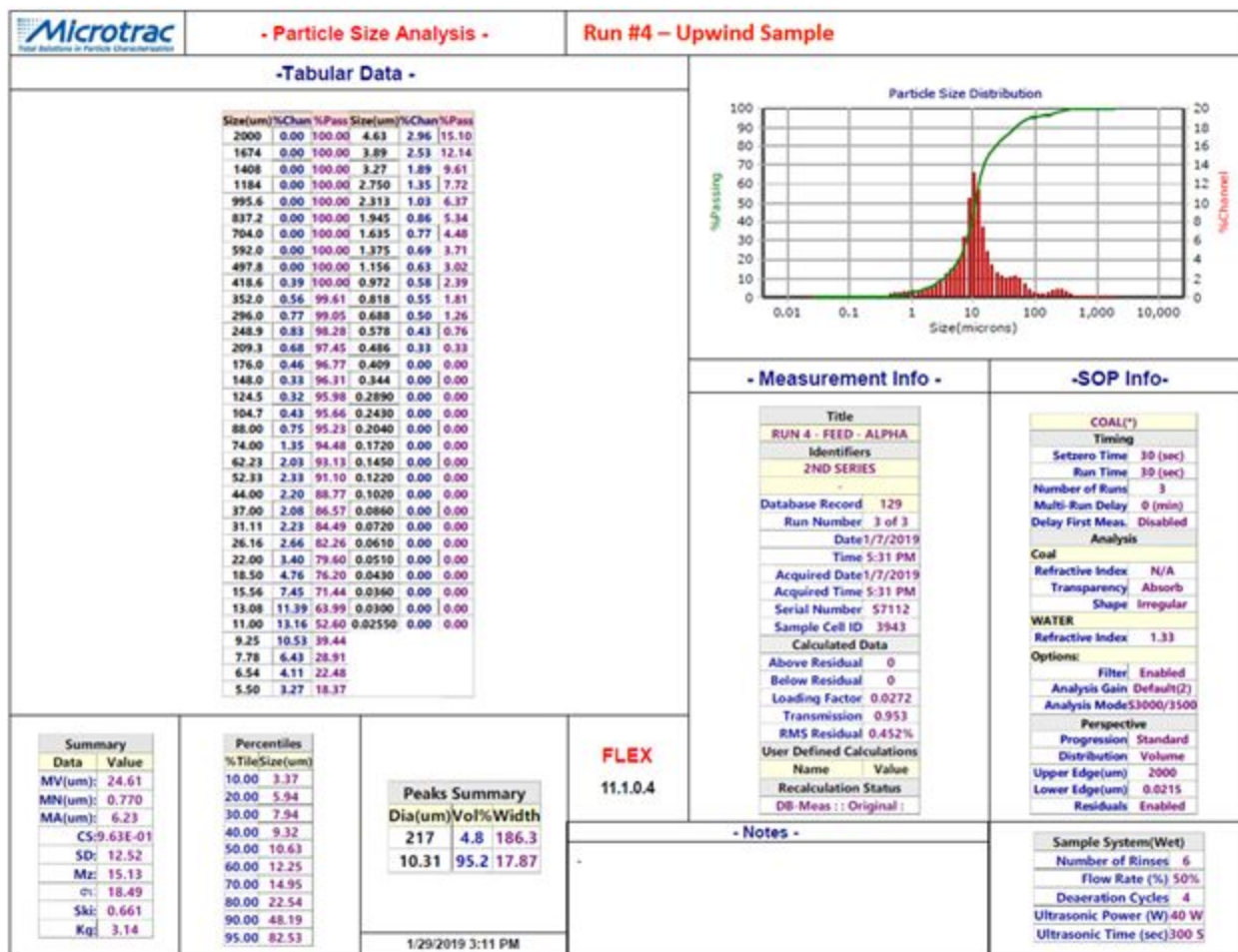




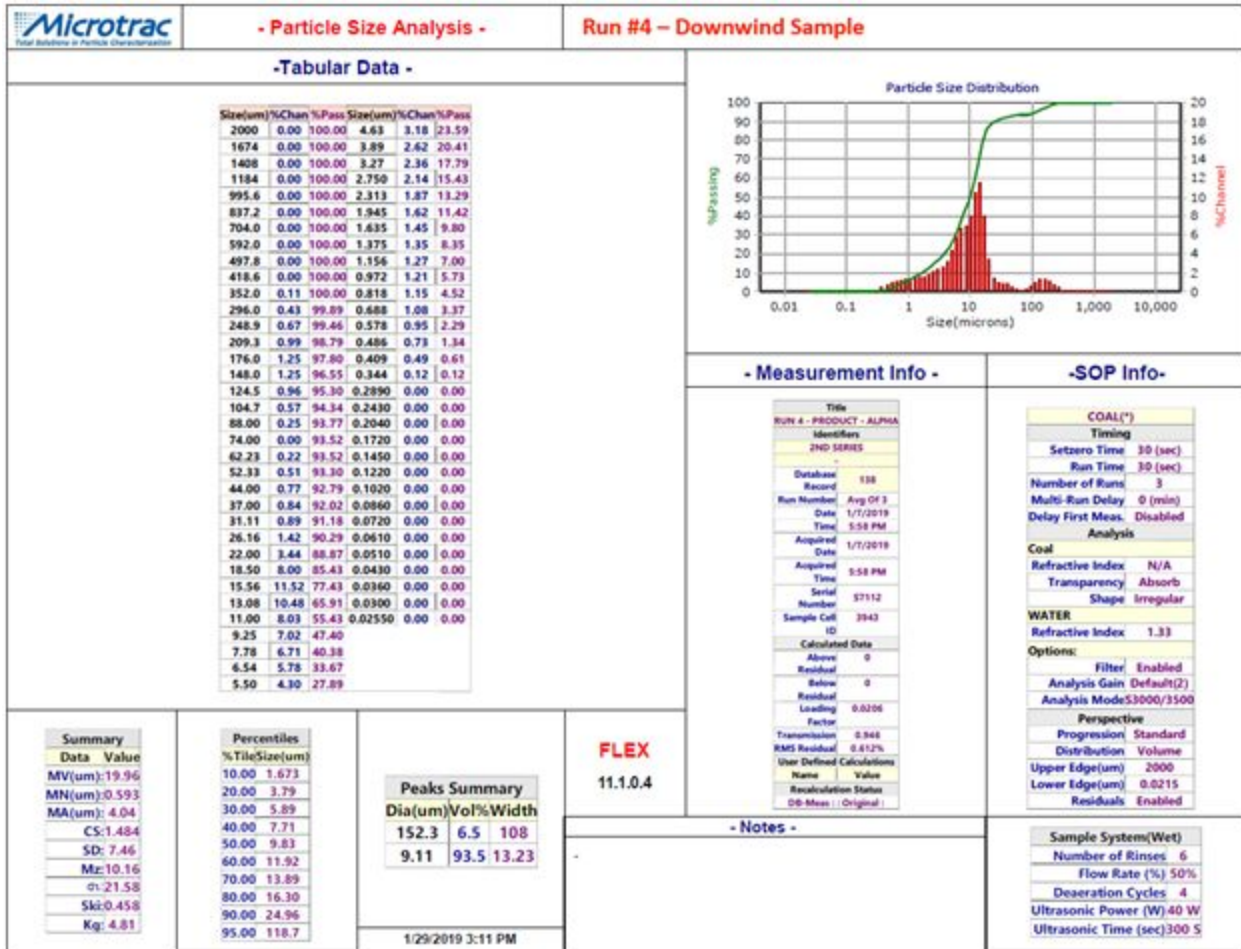


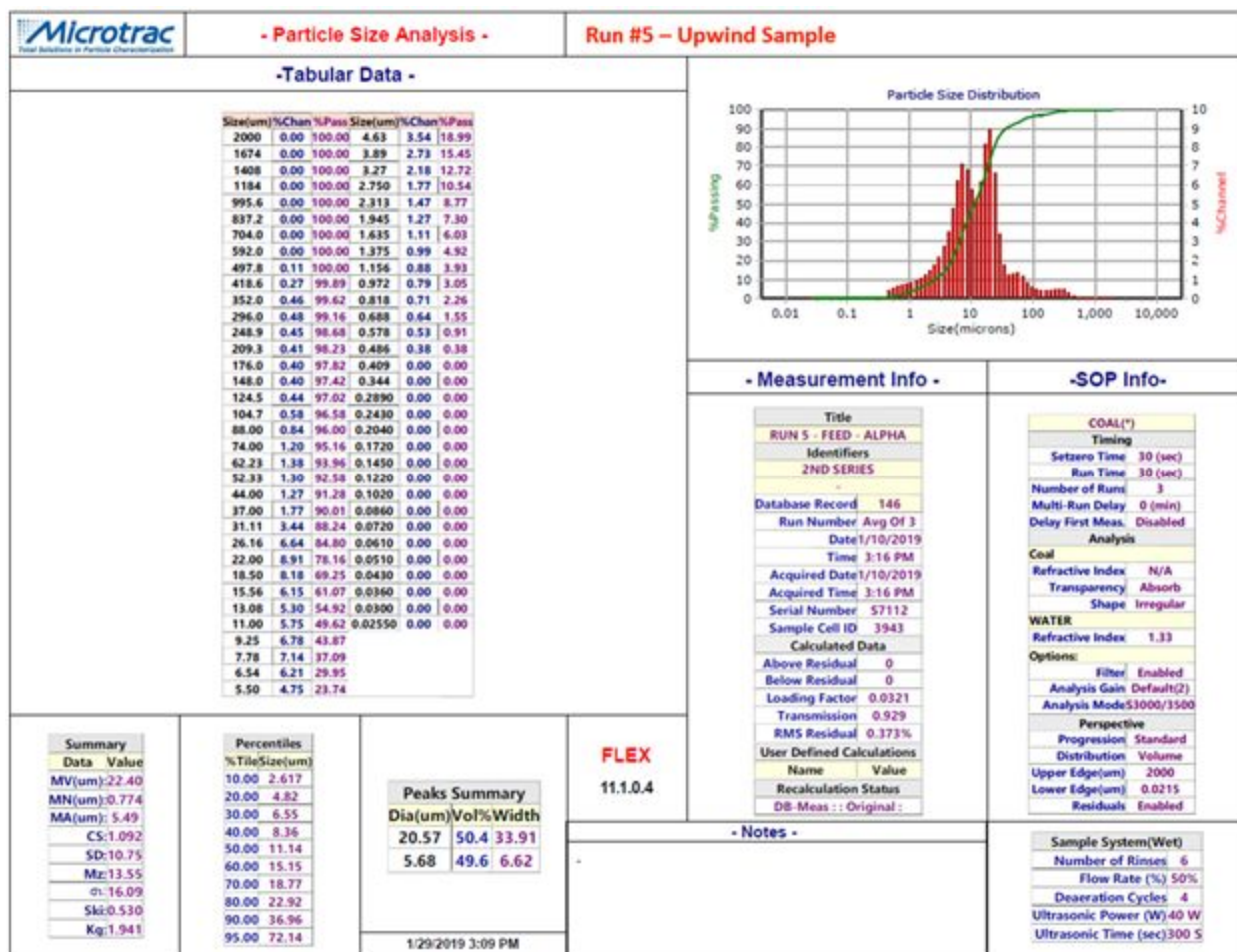


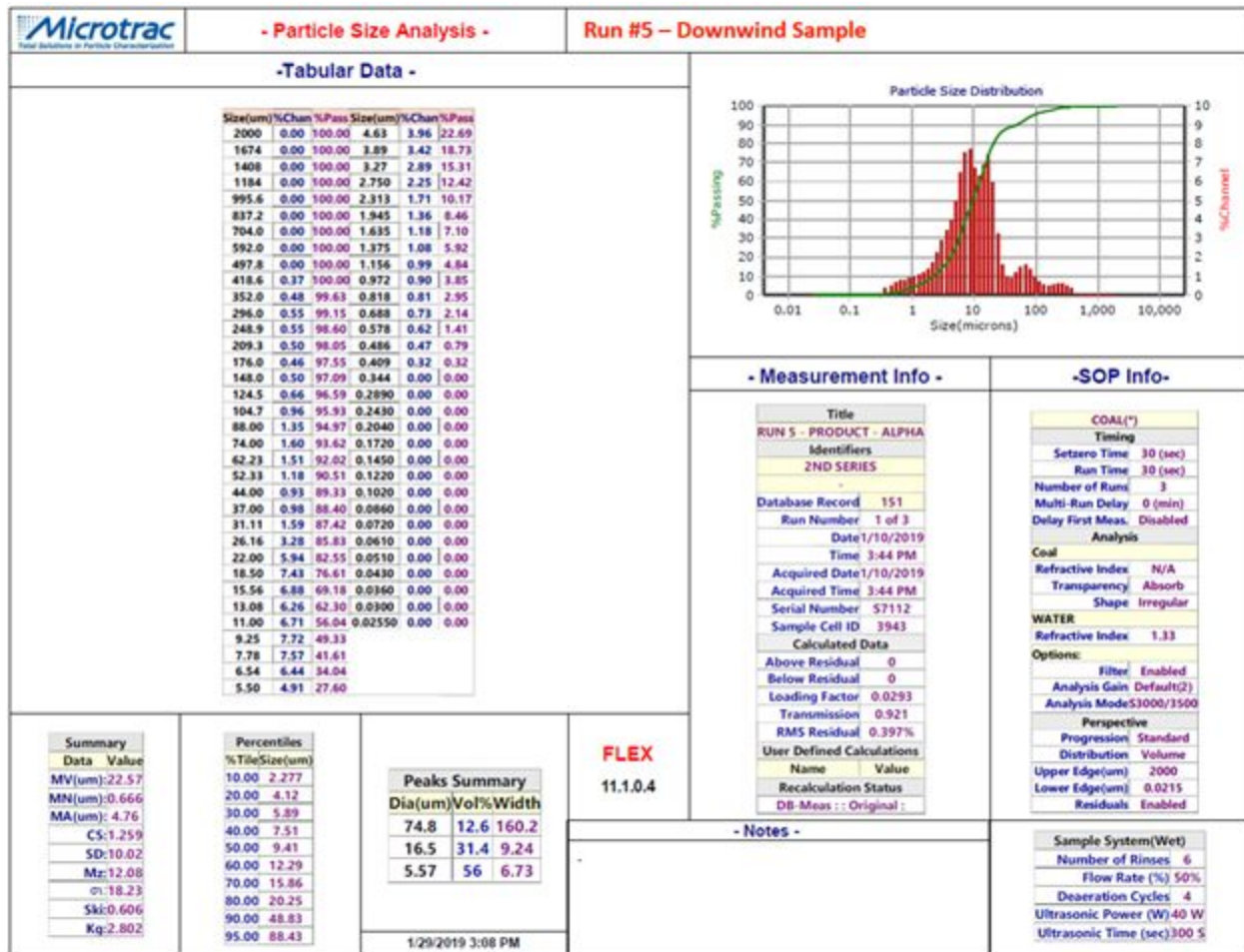


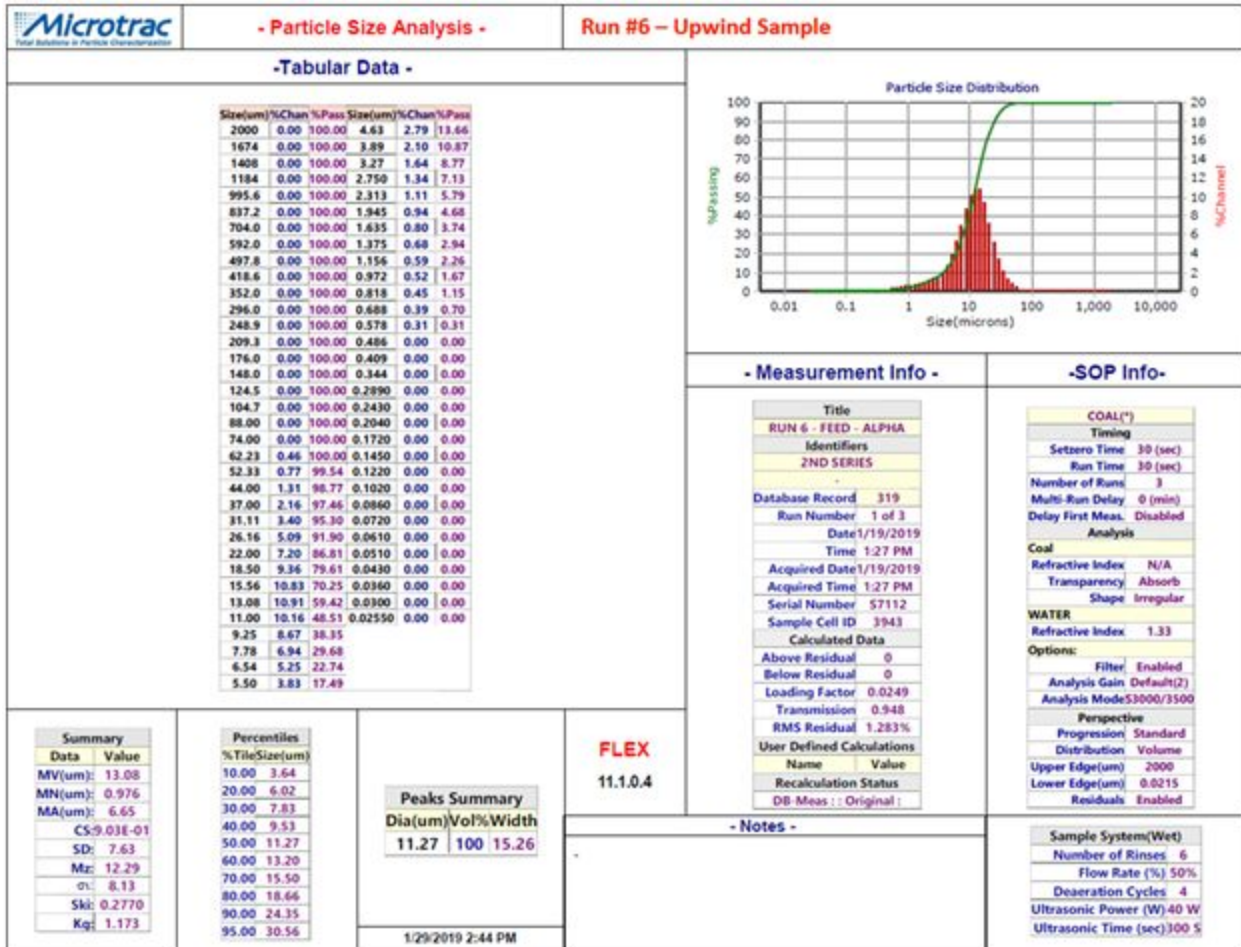




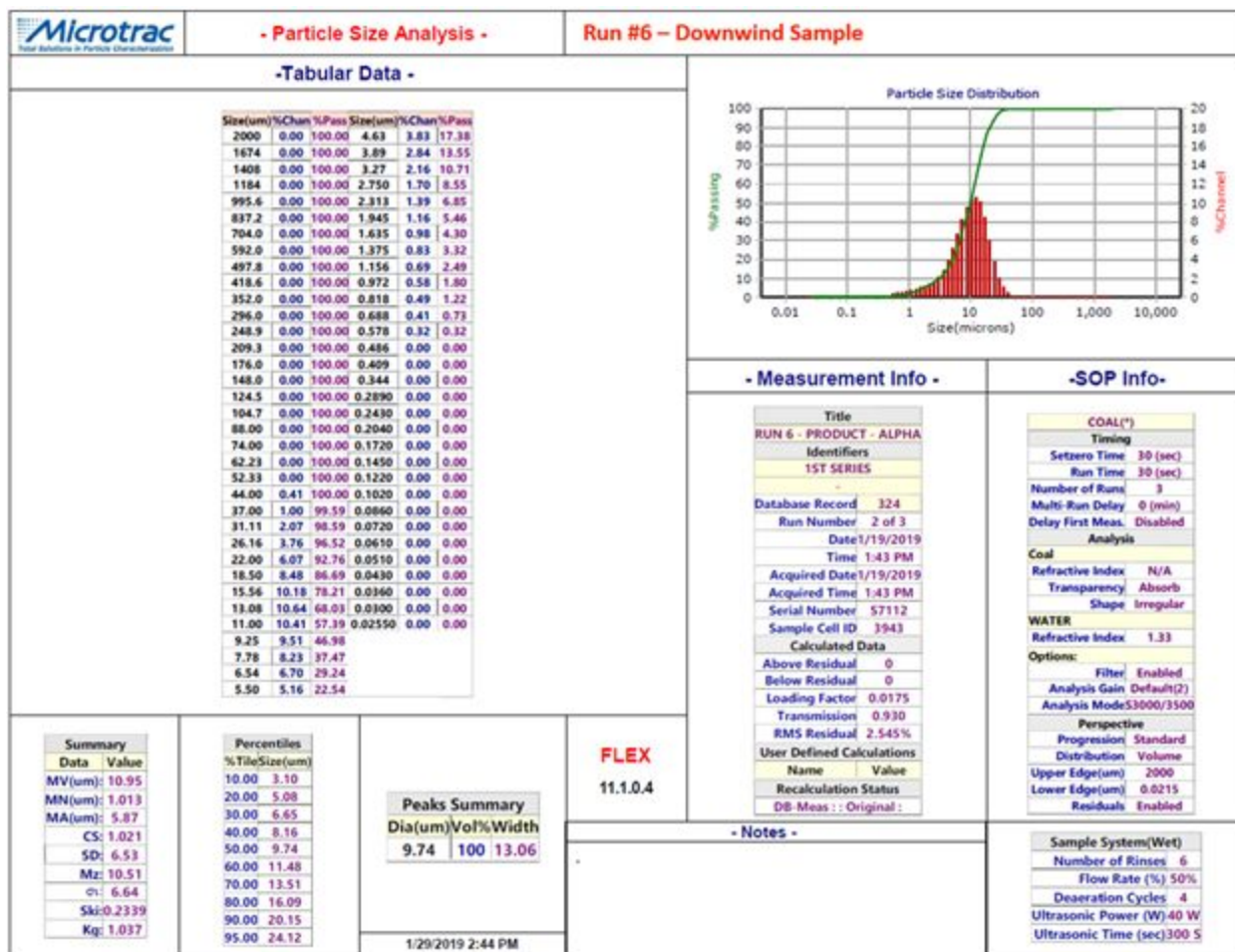


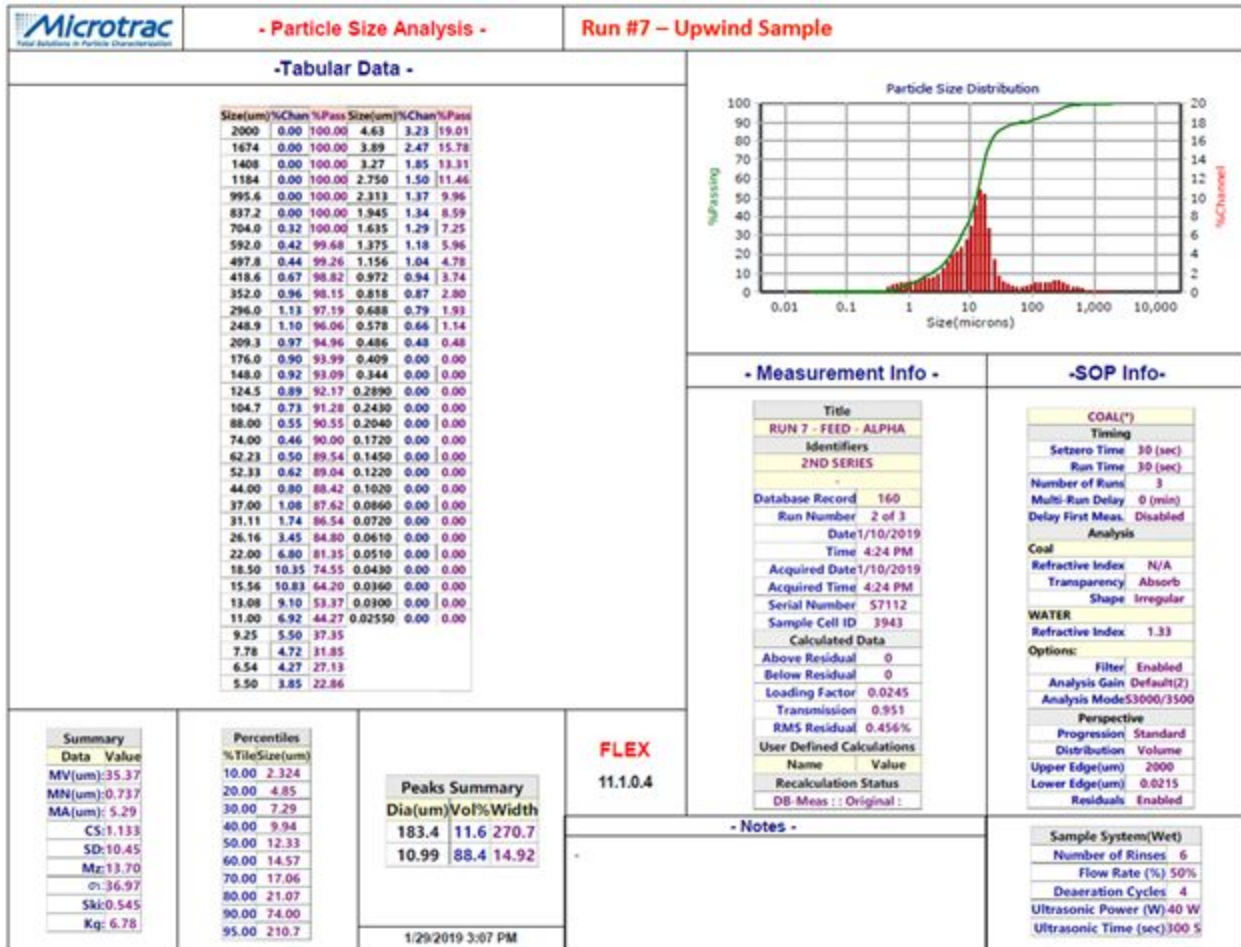




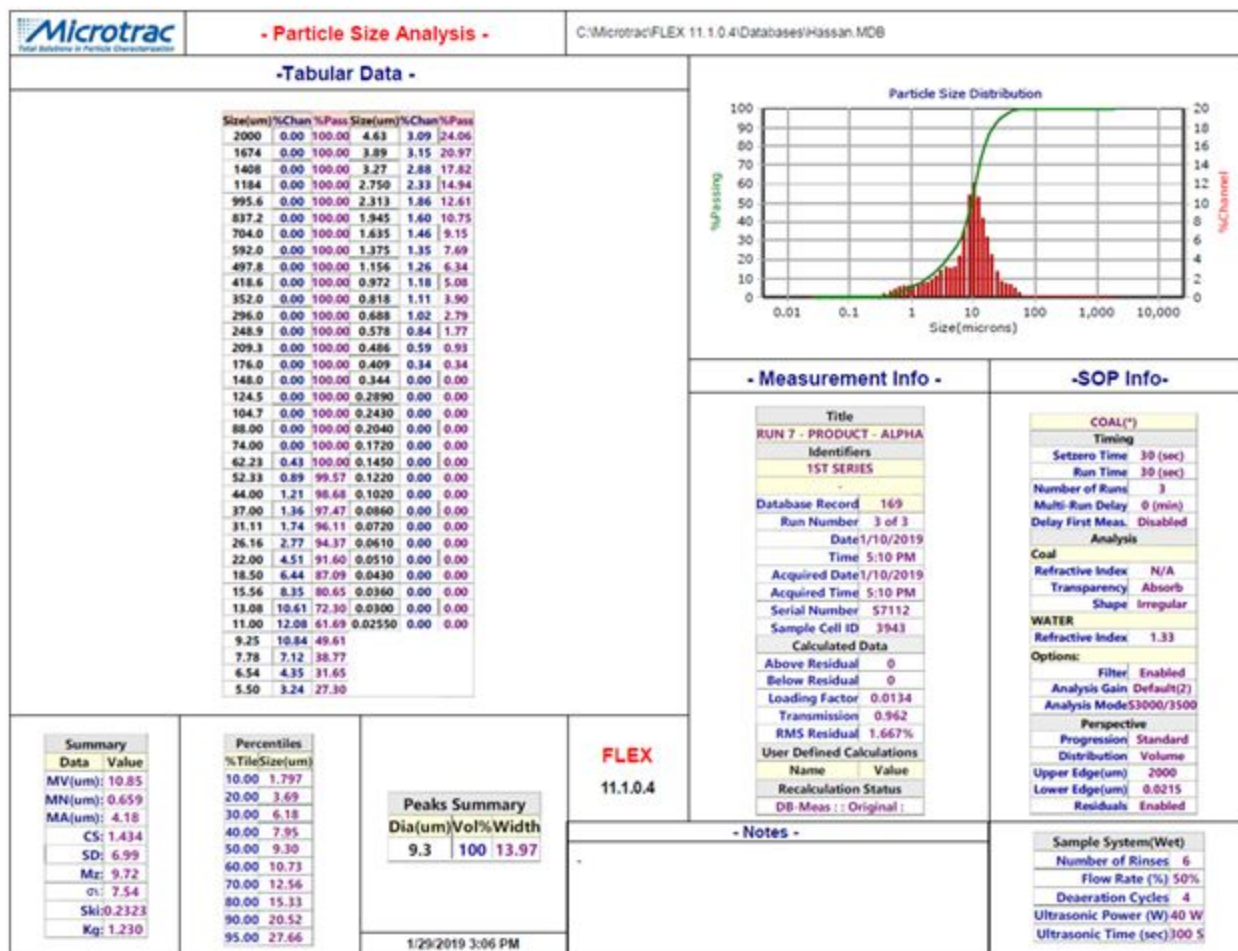


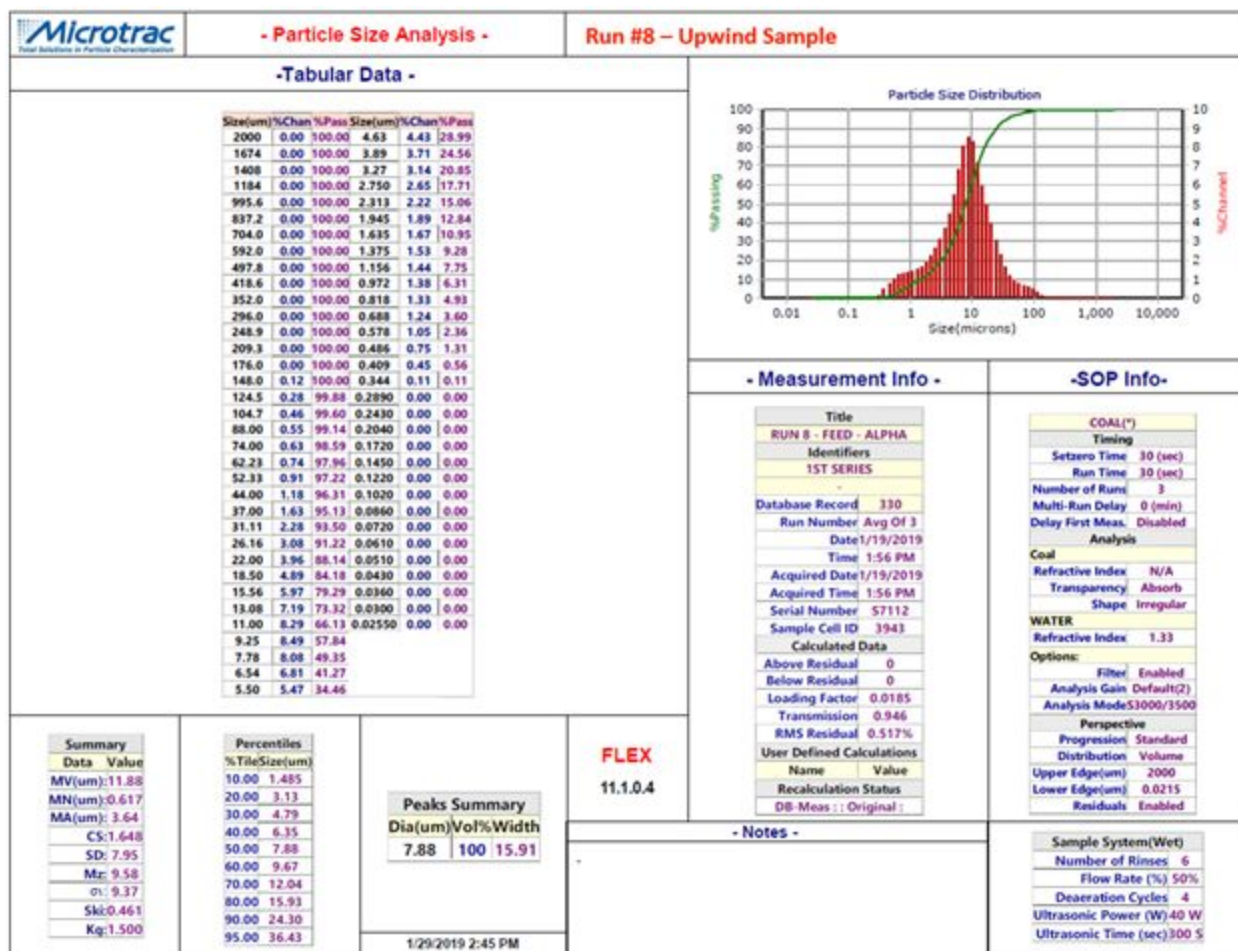


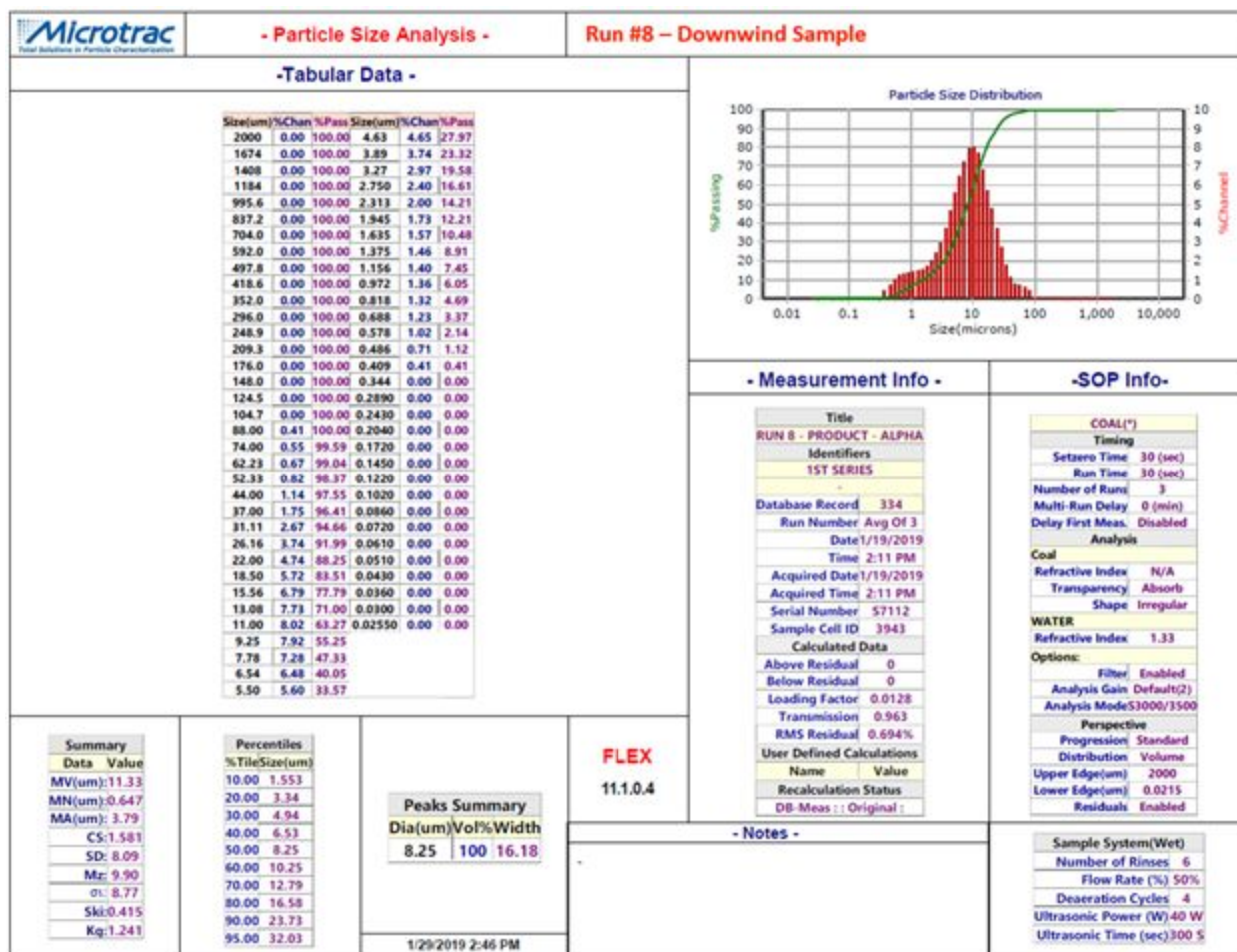


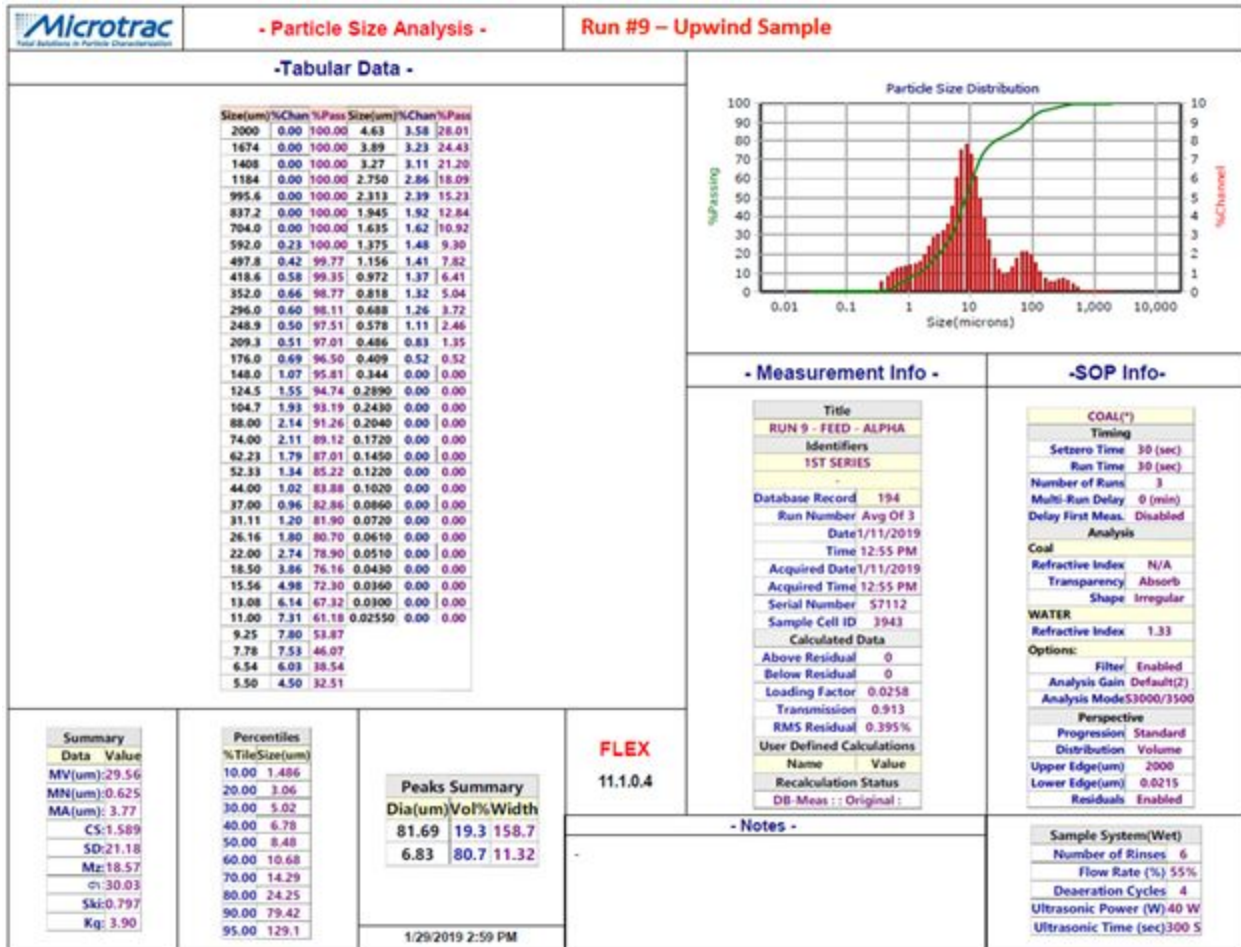




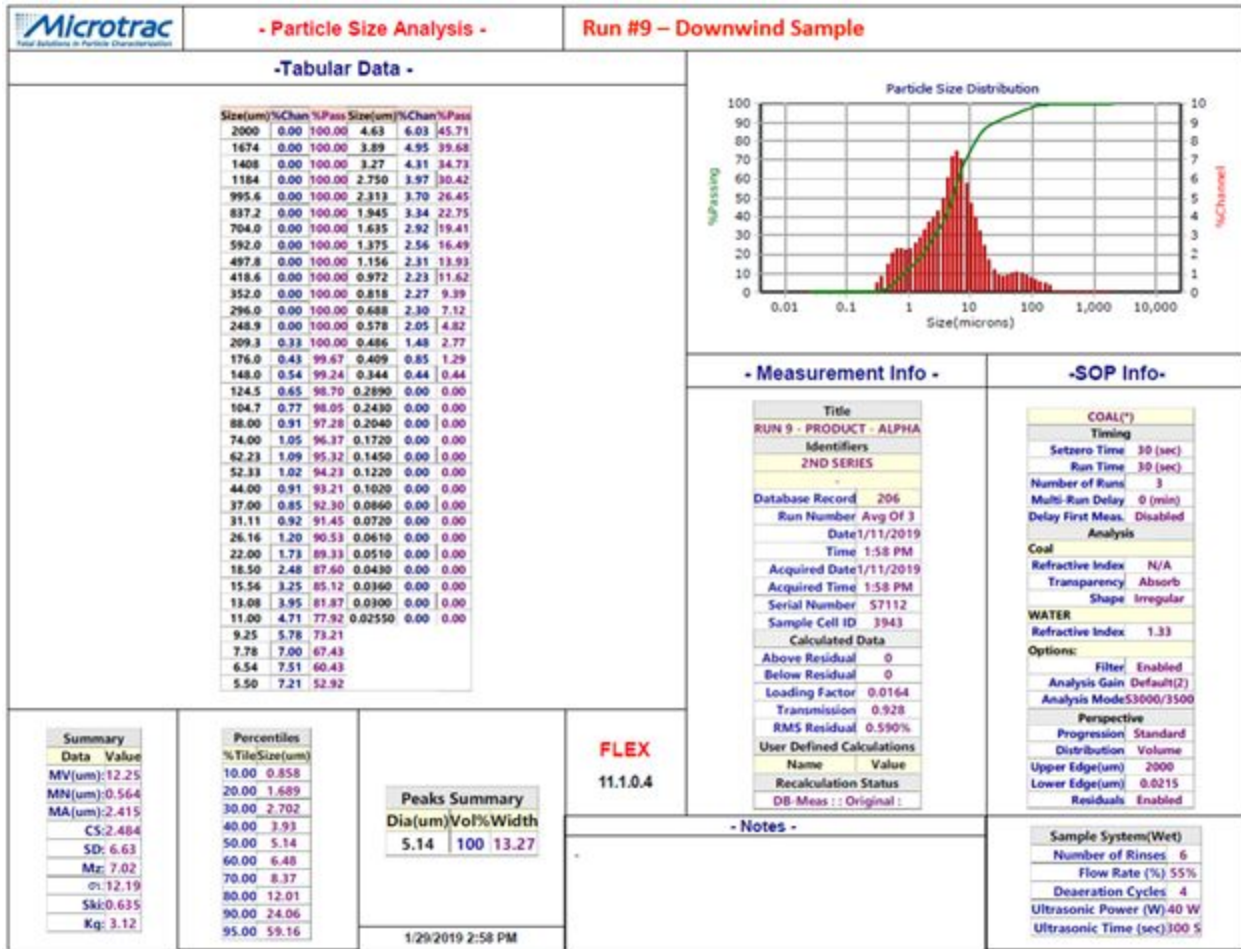


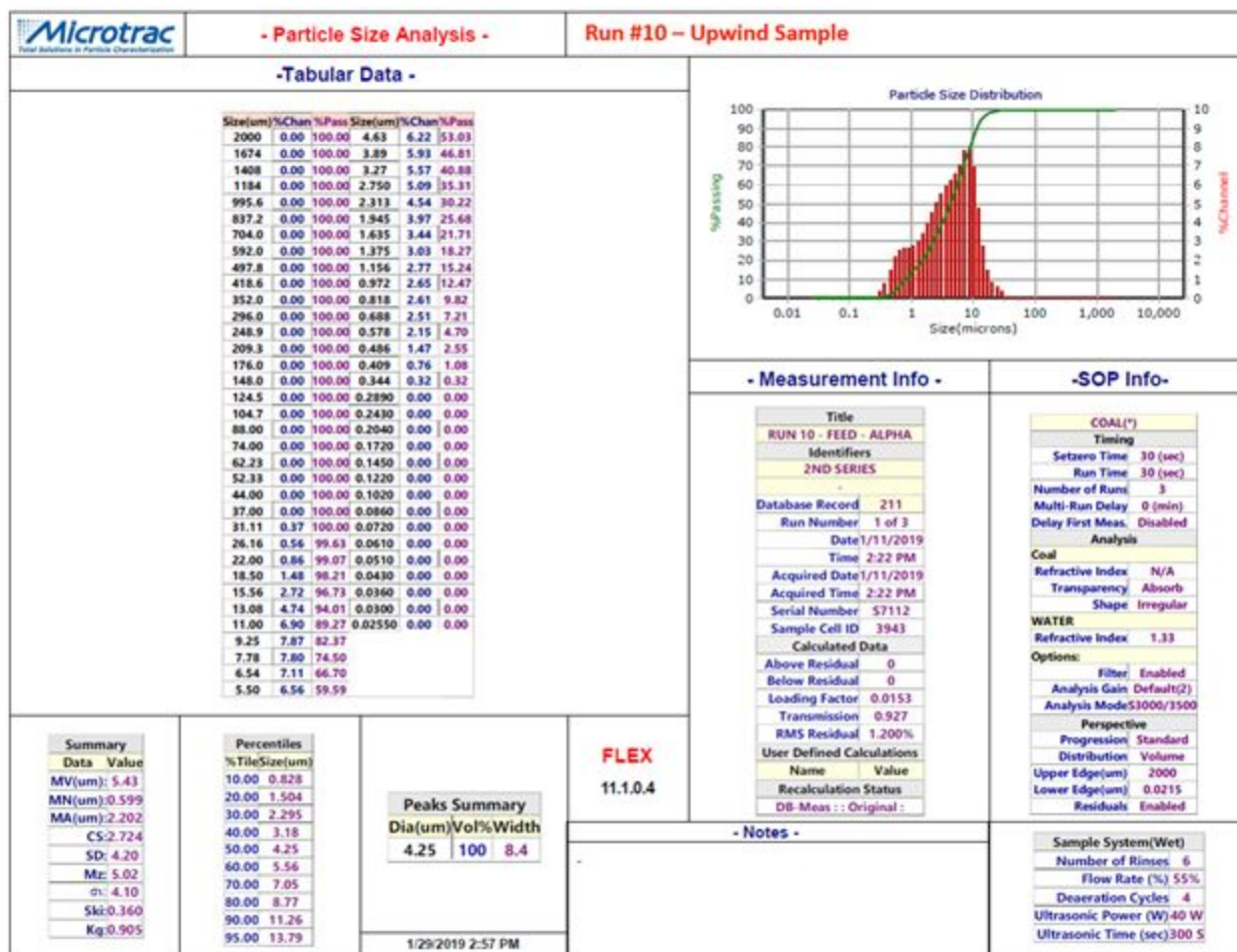




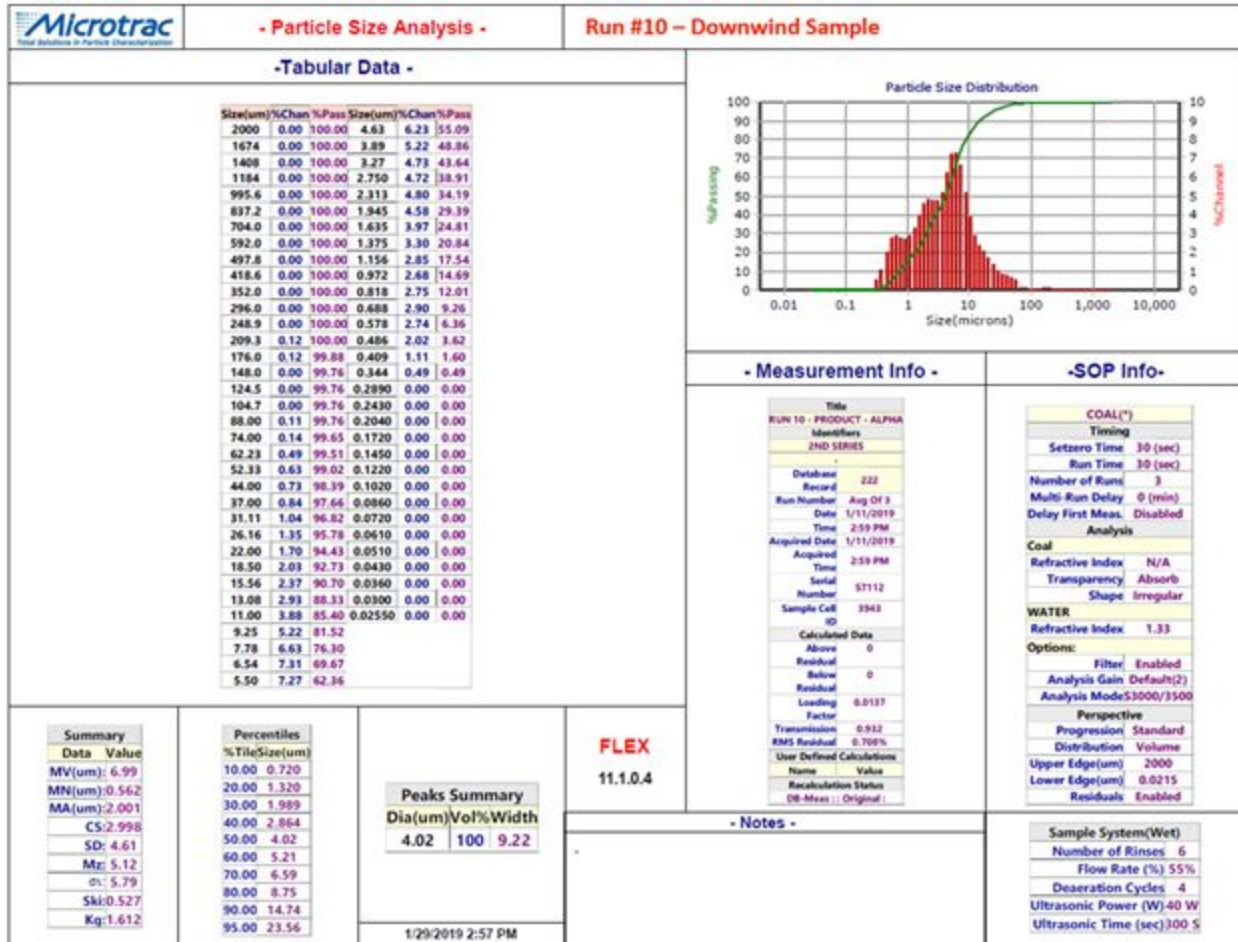


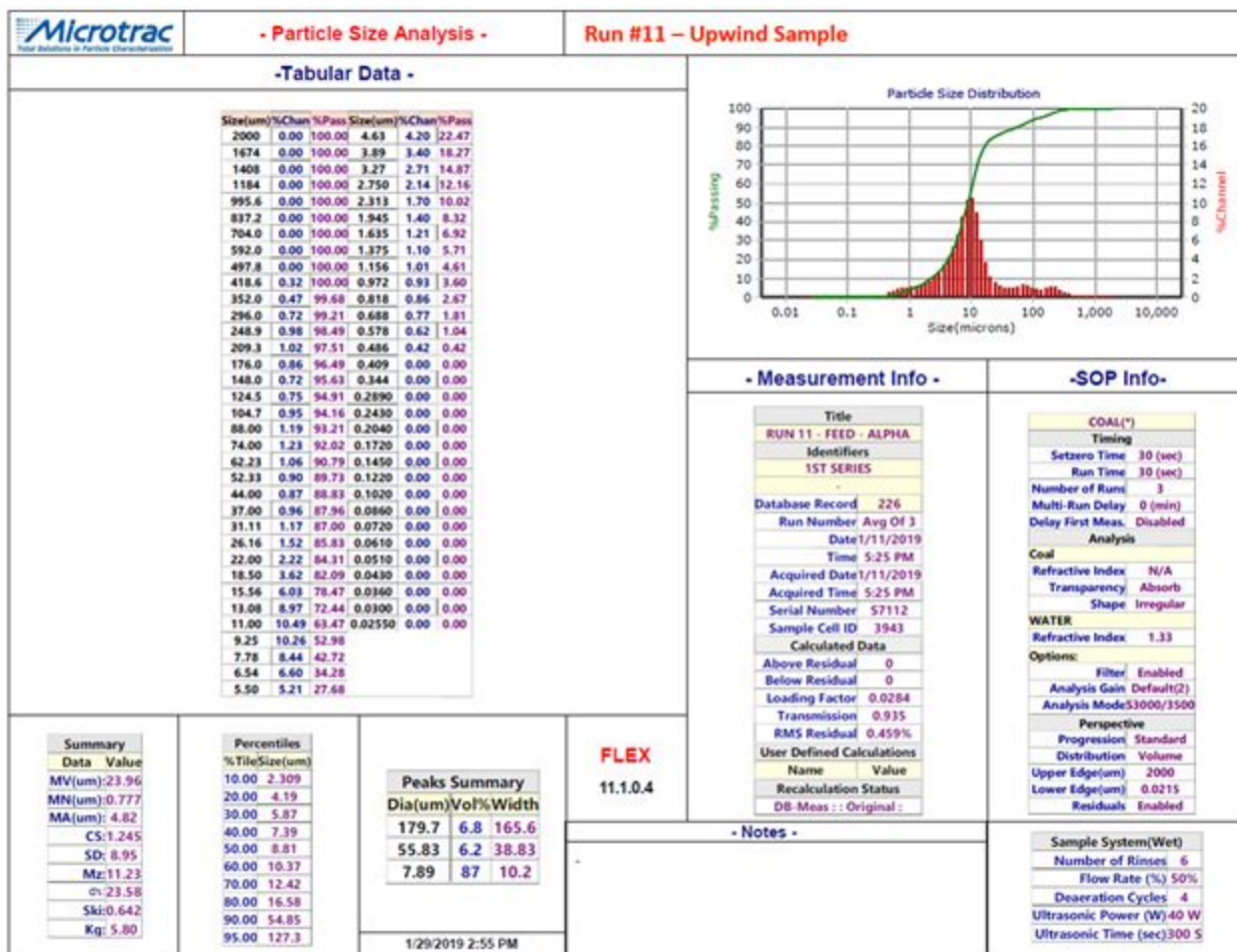


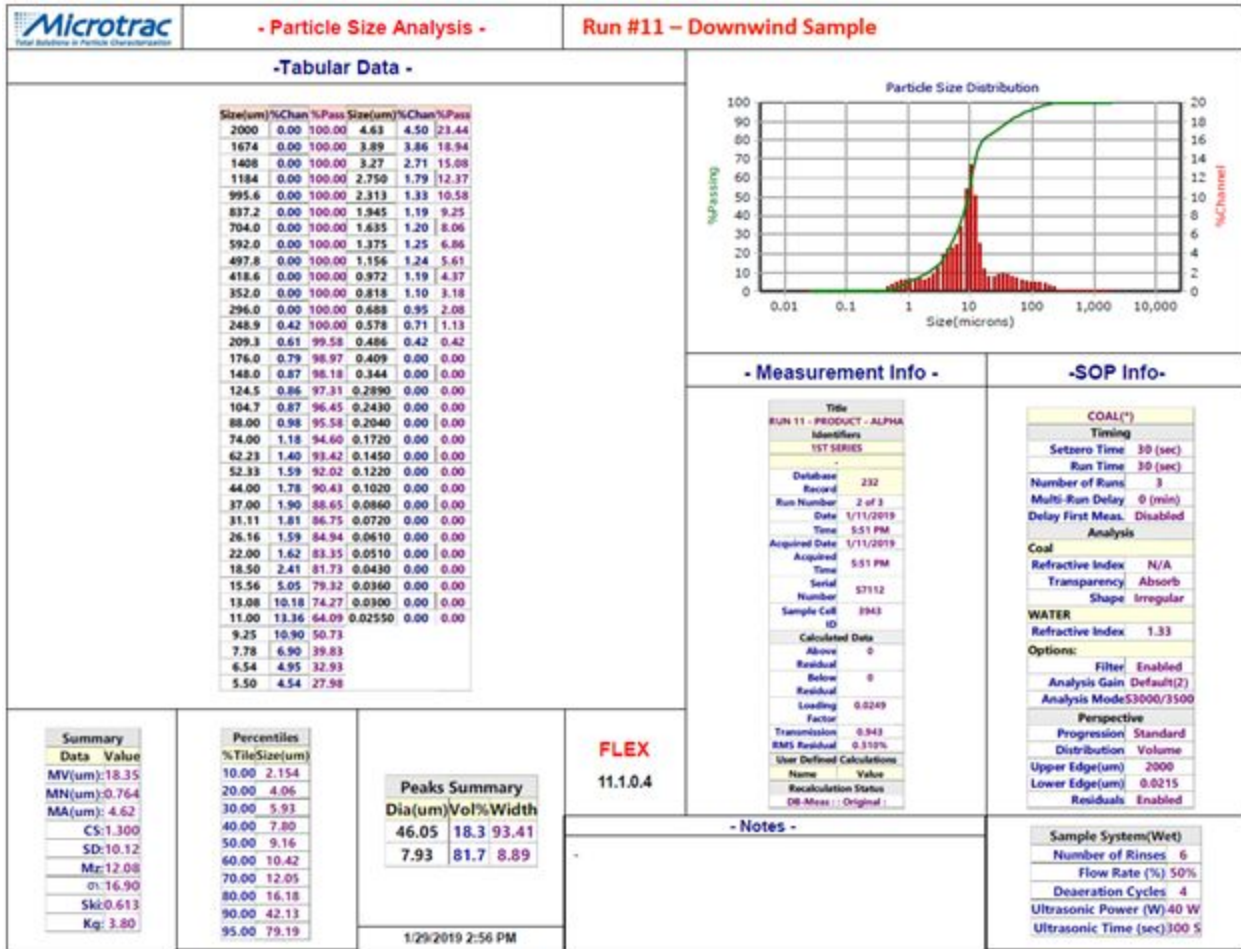


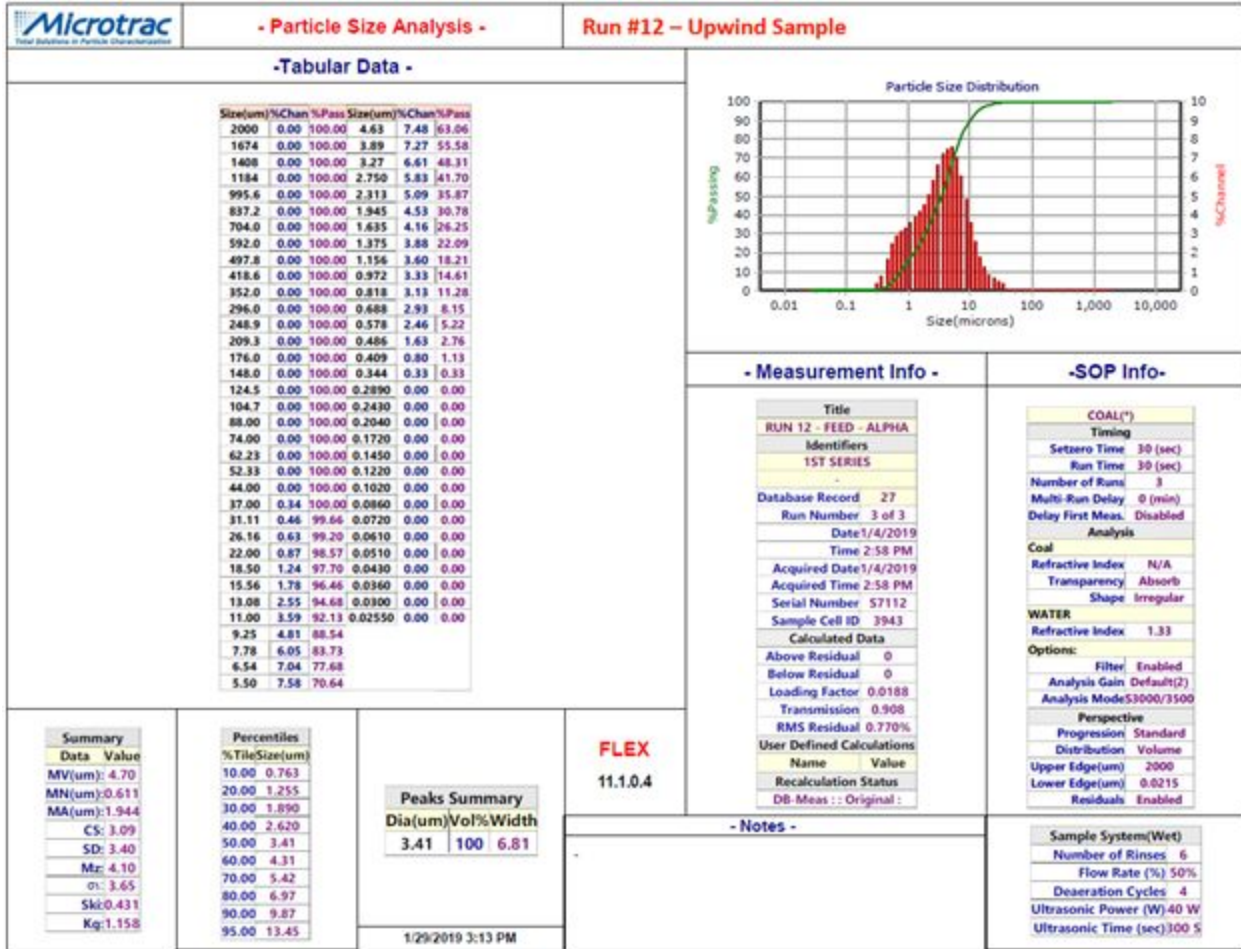




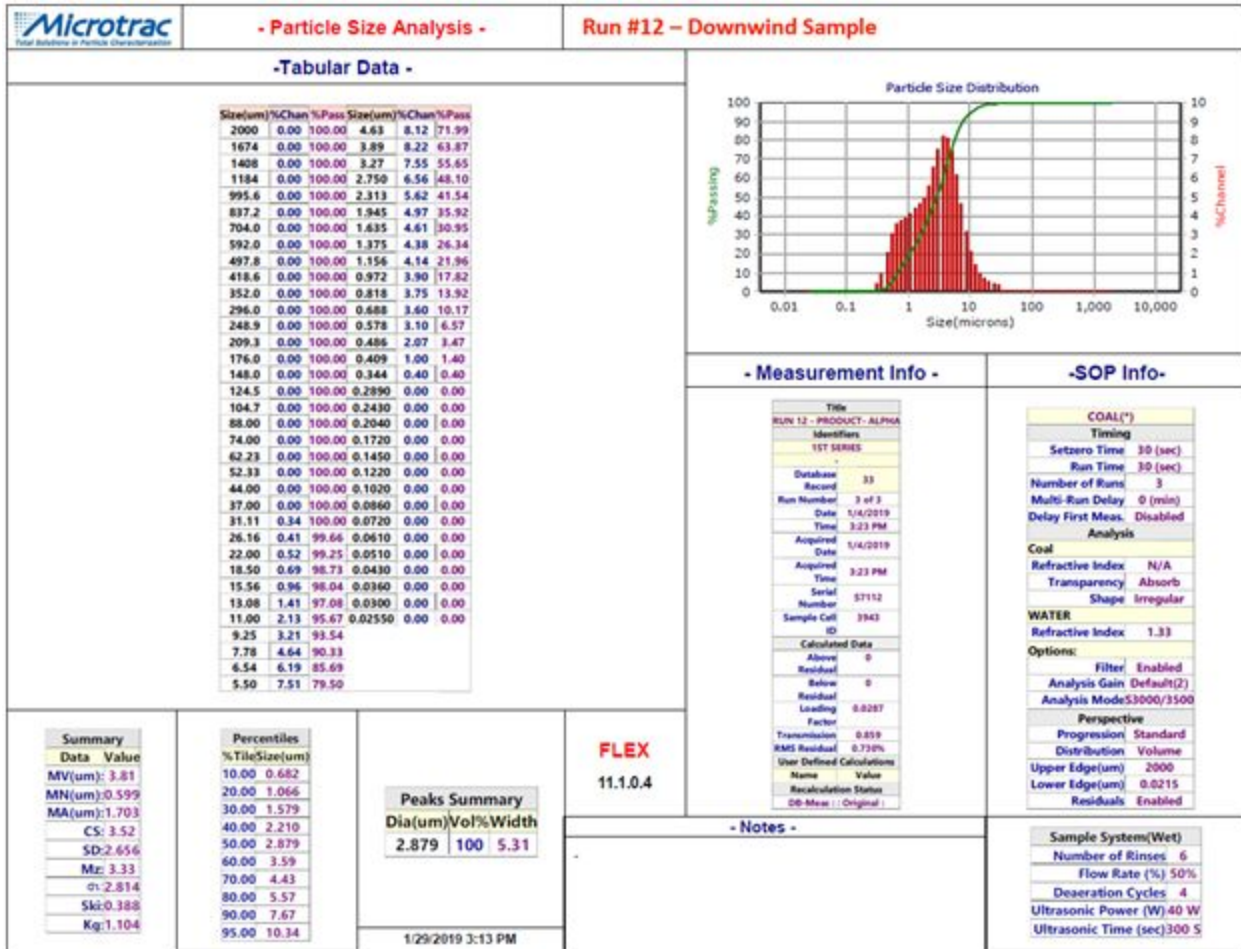


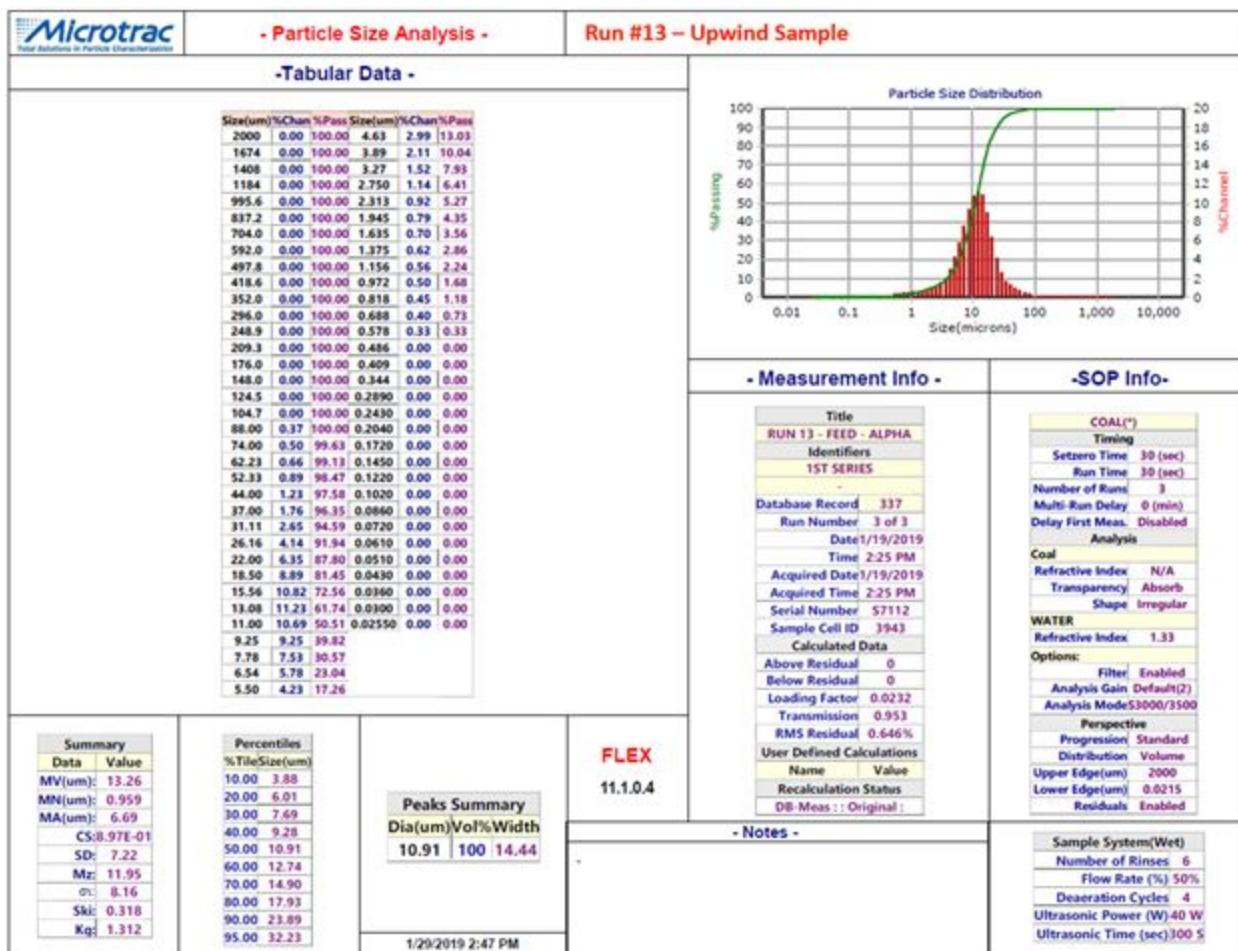




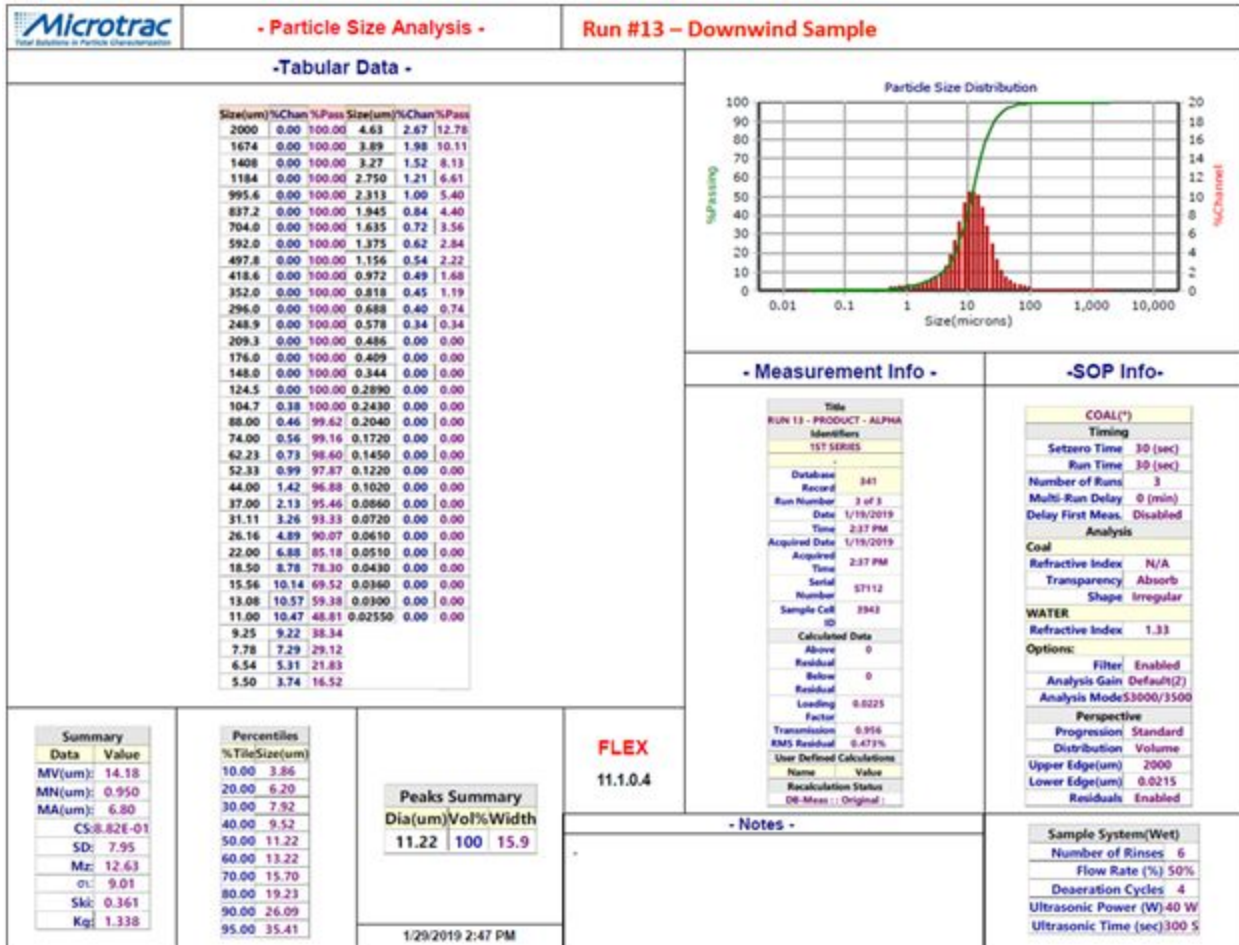


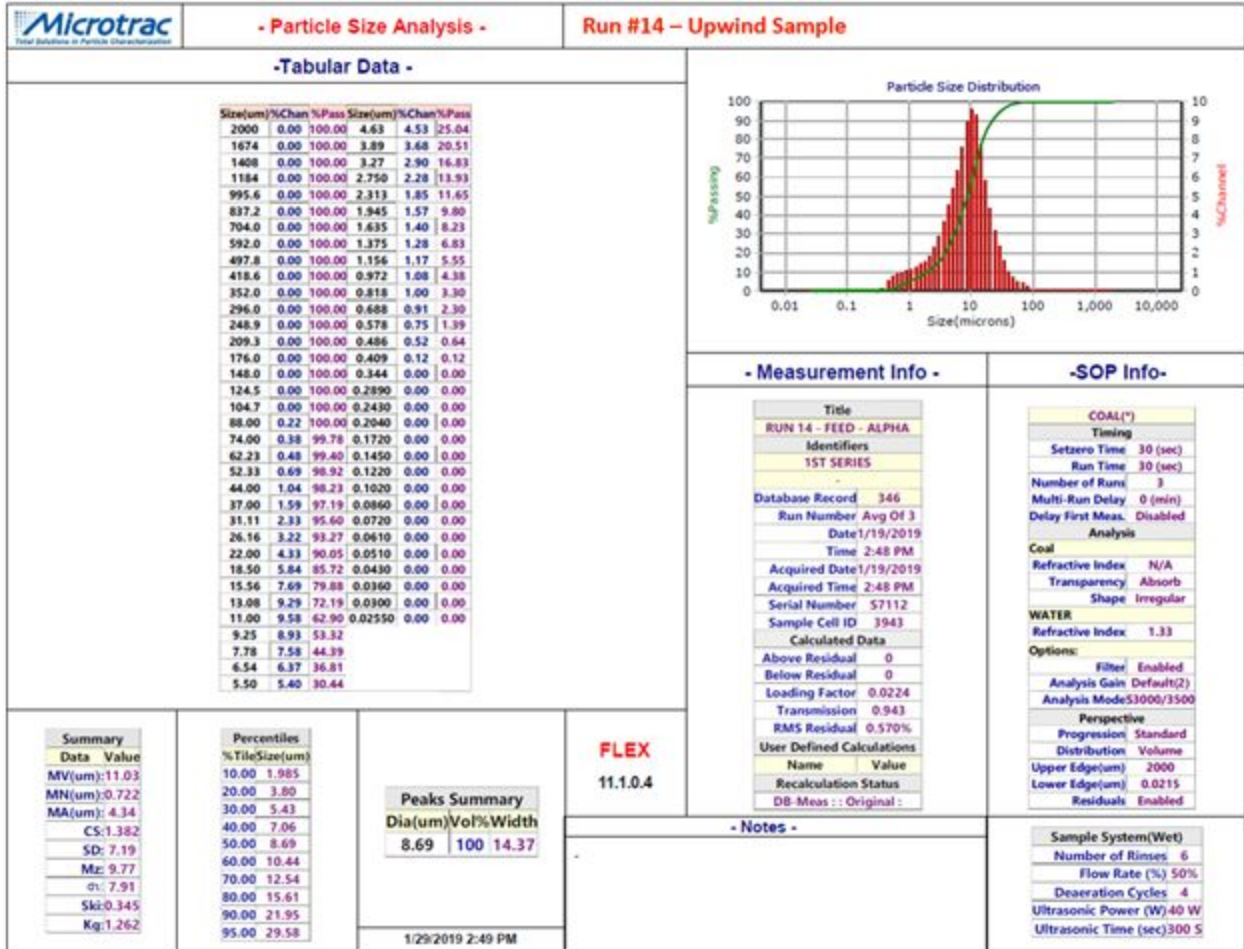


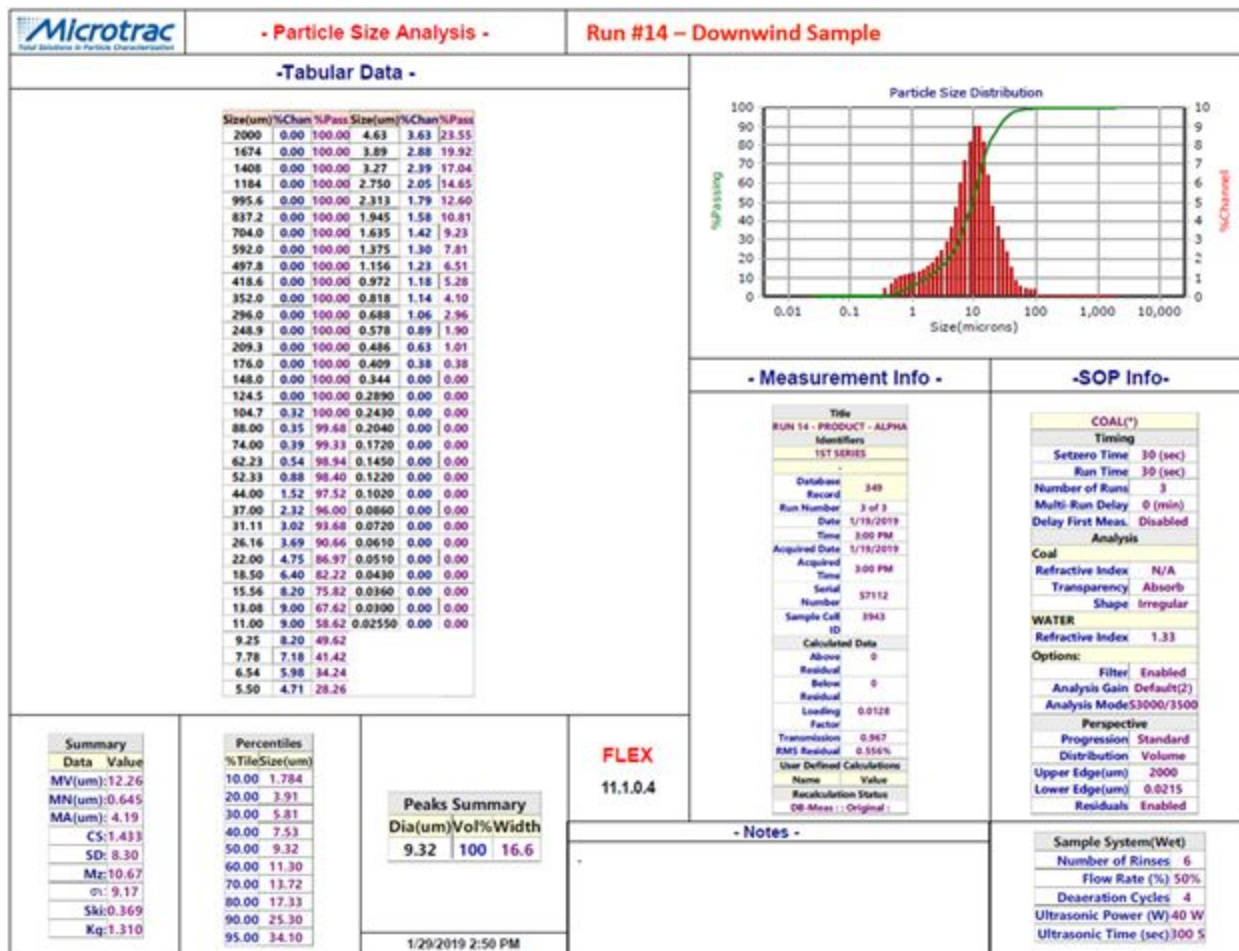


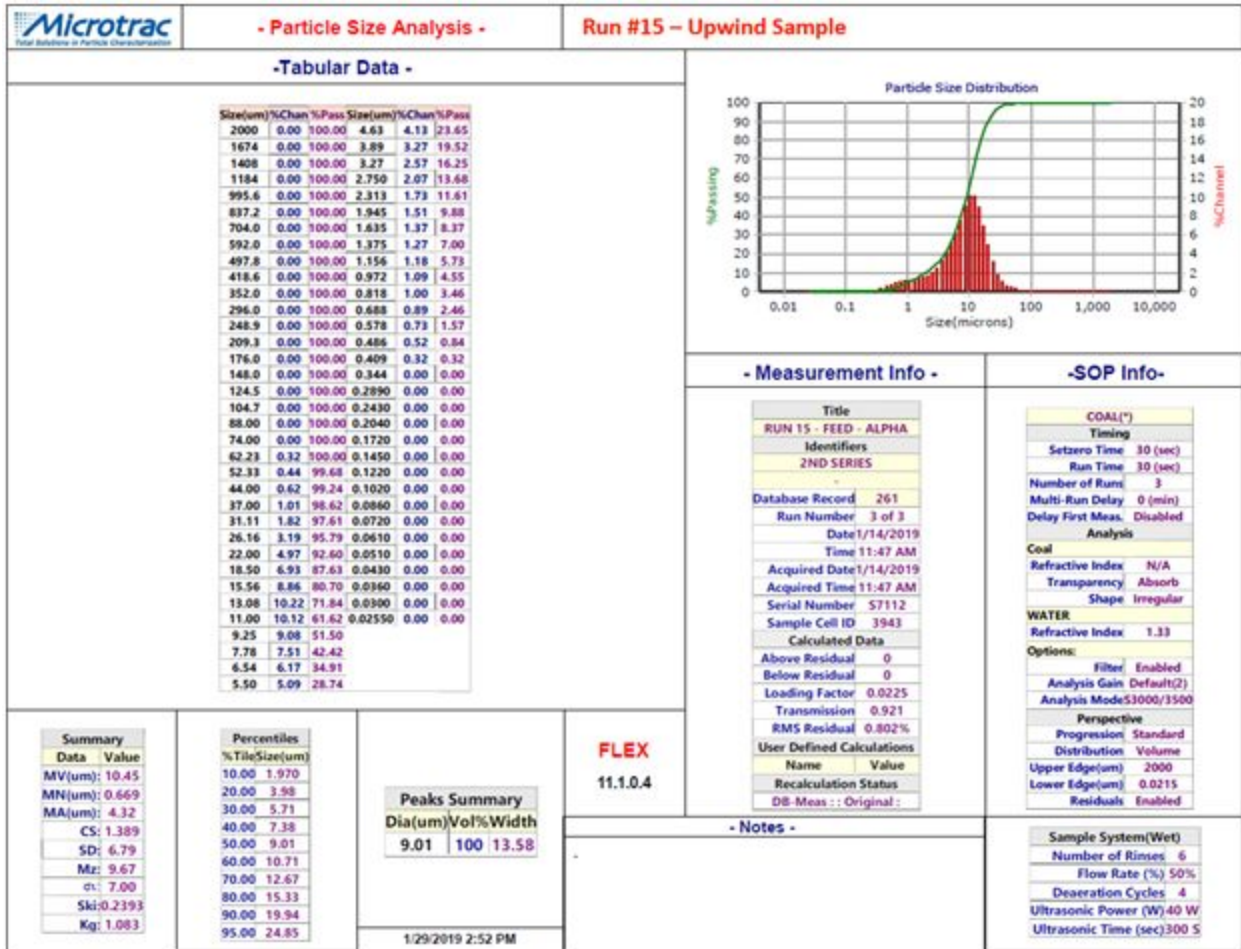




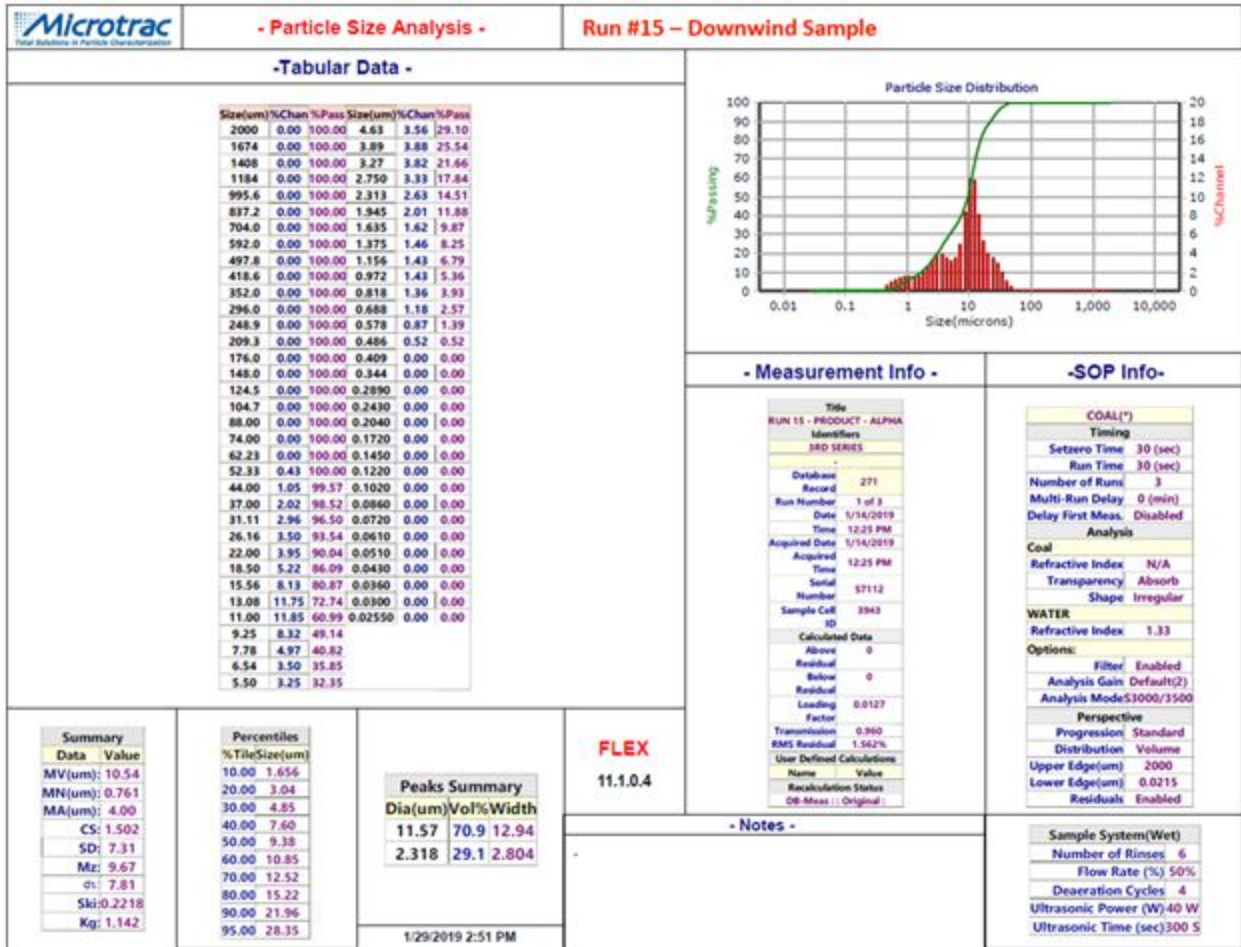












Summary

Data	Value
MV(um):	10.54
MN(um):	0.761
MA(um):	4.00
CS:	1.502
SD:	7.31
σ:	7.81
Mz:	9.67
Ski:	0.2218
Kg:	1.142

Percentiles

%TileSize(um)	
10.00	1.656
20.00	3.04
30.00	4.85
40.00	7.60
50.00	9.38
60.00	10.85
70.00	12.52
80.00	15.22
90.00	21.96
95.00	28.35

Peaks Summary

Dia(um)	Vol%	Width
11.57	70.9	12.94
2.318	29.1	2.804

FLEX

11.1.0.4

- Notes -

Sample System(Wet)

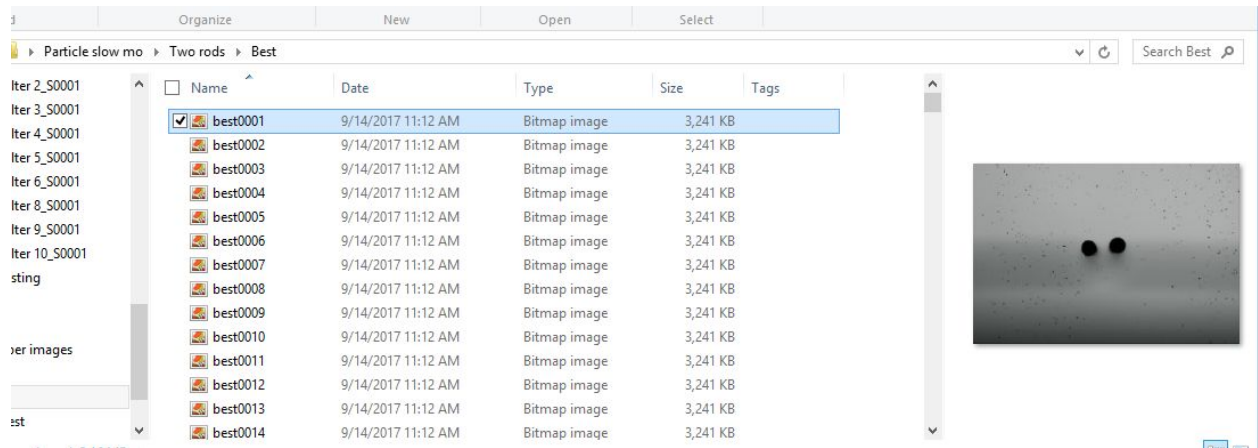
Number of Rinses	6
Flow Rate (%)	50%
Deaeration Cycles	4
Ultrasonic Power (W)	40 W
Ultrasonic Time (sec)	300 S

1/29/2019 2:51 PM

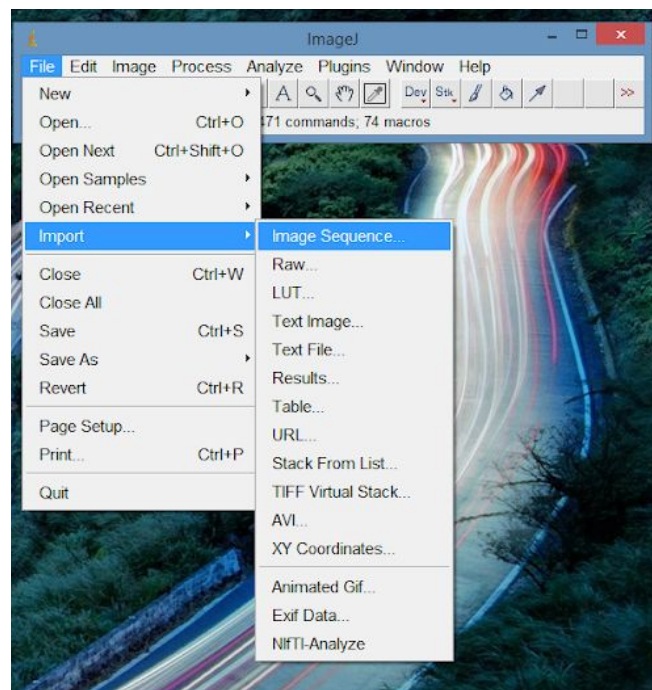
## 7.2. Image Analysis Technique for Tracking Particles:

Here are step-by-step instructions to track particles using a high-speed camera.

1. Convert or make sure that film is saved as image sequence in a single folder.



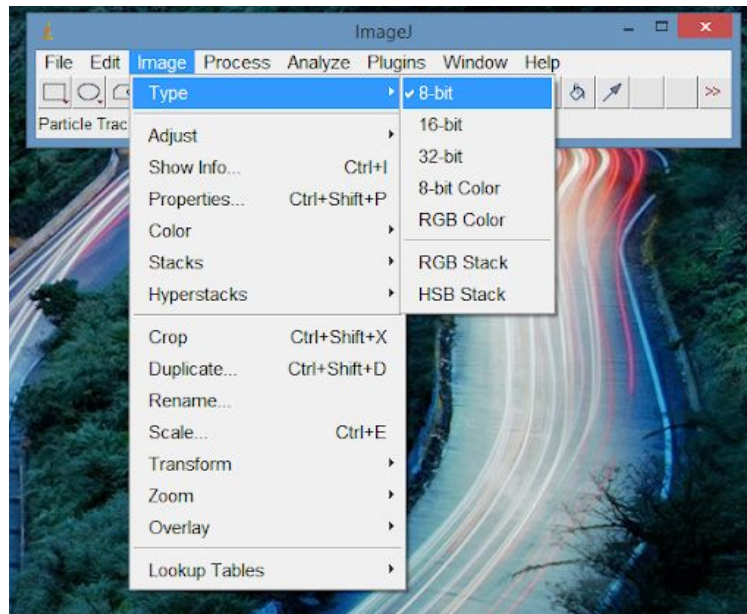
2. Open imageJ and import the image sequence by selecting File->Import -> Image sequence



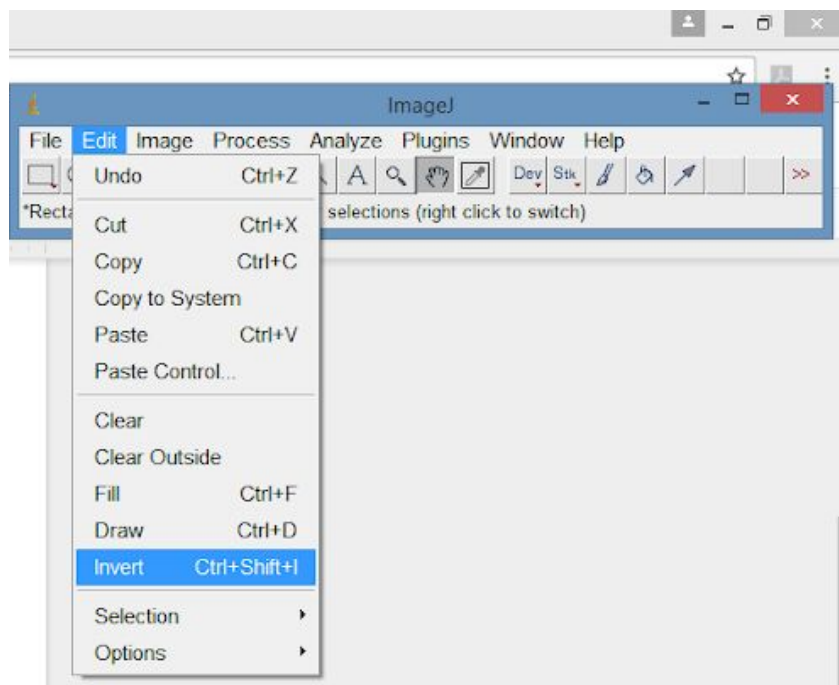
3. A menu for sequence option will open allowing you to select what images of the sequence you wish to select. (I find it best to upload all to allow you to see what frames you will actually want to analyze then repeat the steps above but select only the desired range of frames).
4. The next step is to prepare the image for use with the mosaic plugin.



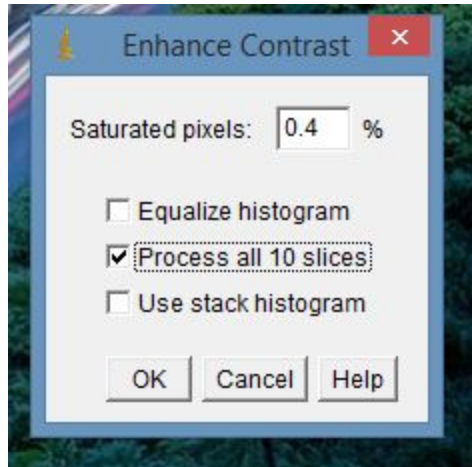
a. To do this you will need to convert the pictures to an 8 bit image, this is done by selecting Image-> Type-> 8-bit



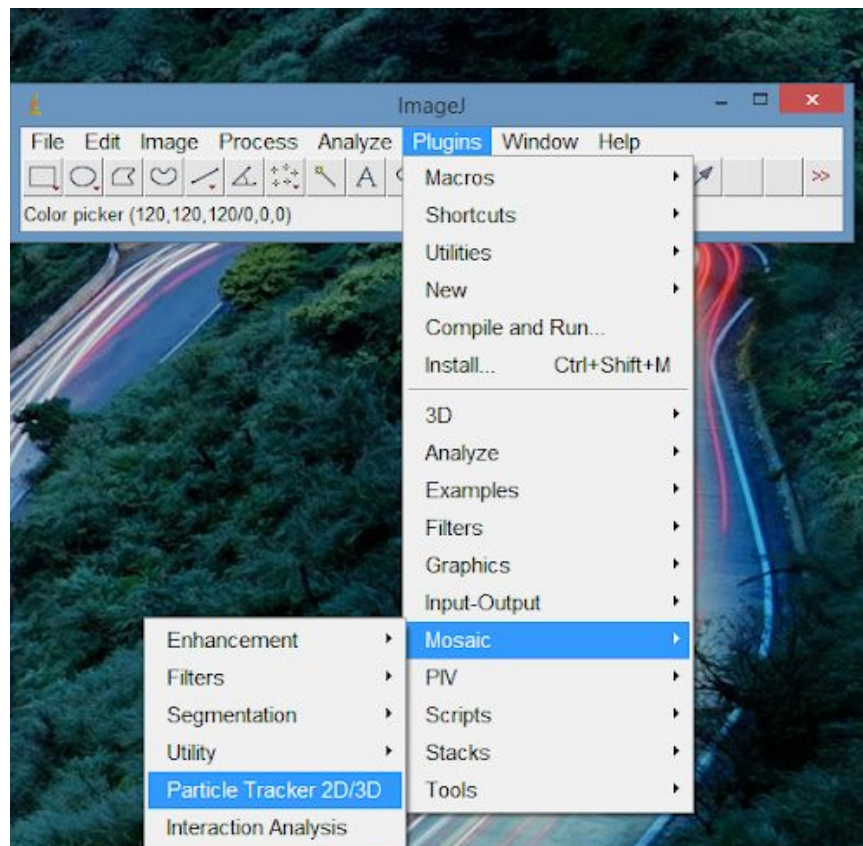
b. Next invert the image switching black and white, (we want the particles to be white, software works much better this way) to do this select Edit -> Invert then in the popup select process all images in stack.



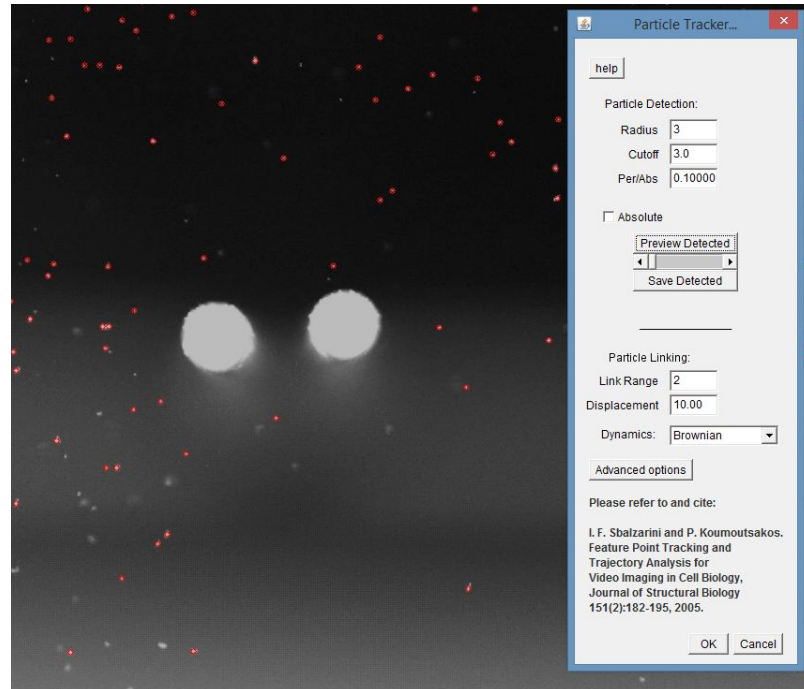
c. Next we will enhance the contrast, this is an optional step as I haven't found much of a difference in results by doing this but it helps us visually. To do this select Process->Enhance Contrast then in the pop up leave or adjust the percentage but make sure you check mark the process all slices.



5. After preprocessing we will now open the Mosaic plugin. Select Plugin->Mosaic->Particle Tracker 2D/3D. Select no on the pop up asking if this is 3D data.



a. Now the particle tracker options pop up should be open. You will have to adjust the radius to be that of just about the size of your particles. 3 to 5 pixels have been working well for me.



b. I usually leave the cut off value as its default but you can mess with it if you like. From my understanding it is used to help differentiate particles that are actually more than one but may be registering only as a single particle. Click the help button for more information on this.

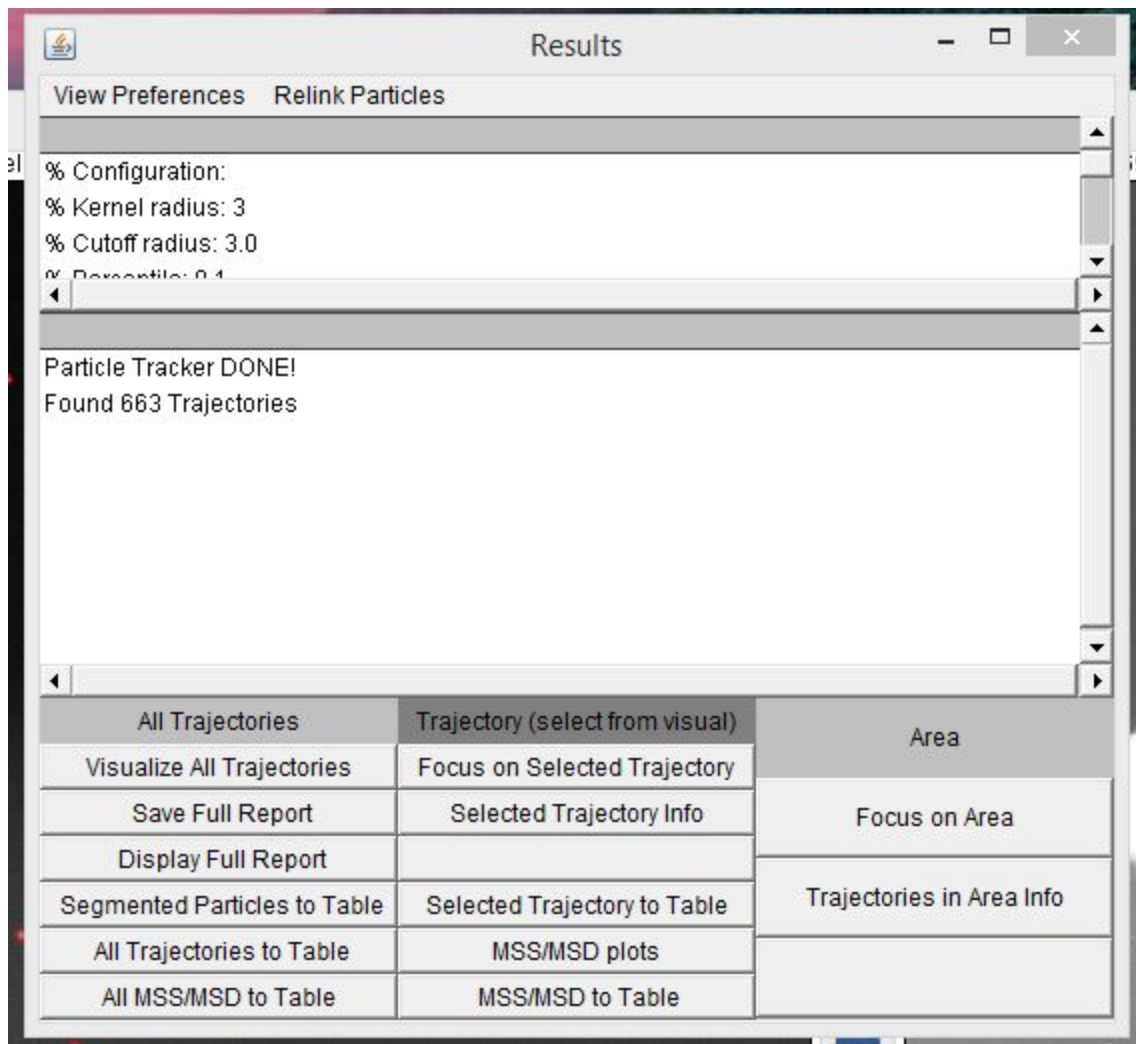
c. For the Per/Abs this value you will have to play around with, it is used to determine how much of a change from black to white is considered a particle. I recommend increasing the value by iterations of .1 and then hitting the preview button to see what the effect is. Pretty much the goal here is to let it find most, if not all the particles, but have almost none to few pieces of interferences or static show up as particles, this usually occurs around the filter or object we are introducing into the particle flow.

d. The last items you will need to play around with are the linking and linking displacement. These are used by the software to track the particles across the frames even if it loses the particle for a frame or two depending on the link range value set. The displacement value is used to tell the software up to how far away it should look for the missing particle in the next frame. I recommend starting with the defaults and then play with the settings from there.

6. After getting all your settings selected hit enter or okay and let it do its work. Depending on your settings and your images this may take a while to run. You can usually find your progress on the imageJ menu bar.



7. When it is done you should see a results pop up window. This is where you can export the data, visualize the trajectories and adjust your linking parameters.



8. To see the trajectories select Visualize trajectories. You can save this as an AVI video by selecting File-> Save as -> AVI then select the frame rate and location.

9. To export the position data on the results window select all trajectories to table and then save the table.

### 7.3 Contact Angle Data

Table A.1. Contact angle of aqueous solution on freshly polished coal surfaces in the presence of sodium dodecyl sulfate (SDS).

Concentration (mM)	Surface tension (mN/m)	Contact Angle
0	72	75.48
0.005	71	75
0.05	70	75
0.5	69.5	75
1	69	75
2.5	61.8	61.3
5	49.8	48.8
7	45.1	23.19

Table A.2. Contact angle of aqueous solution on freshly polished coal surfaces in the presence of Polyethylene Oxide (Triton X-100).

Concentration (mM)	Surface tension (mN/m)	Contact Angle
0	72	75.48
0.001	65	74
0.01	53	62
0.05	42.5	55
0.1	37.5	20
0.2	32	5
0.5	31.5	0



Table A.3. Contact angle of aqueous solution on freshly polished coal surfaces in the presence of Dioctyl sulfosuccinate sodium (AOT).

Concentration (mM)	Surface tension (mN/m)	Contact Angle
0	72	75.48
0.1	63	74
1	35.2	45.38
10	28	0

Table A.4. Contact angle of aqueous solution on freshly polished coal surfaces in the presence of Polyoxyethylene-modified polydimethyl-siloxane (Dow OFX-5211)

Concentration (mM)	Surface tension (mN/m)	Contact Angle
0	72	75.48
0.005	37	44.98
0.01	22.7	20.55
0.05	22	0
0.1	21.7	0

Table A.5. Contact angle of aqueous solution on freshly polished coal surfaces in the presence of Silicone polyether copolymer (Dow Corning 502W)

Concentration (mM)	Surface tension (mN/m)	Contact Angle
0	72	75.48
0.005	38	43.37
0.01	24.6	27.5
0.05	22	0
0.1	21.7	0

#### 7.4 Surface modification of mesh

Table 2.2 shows the contact angle results obtained on two polished stainless steel sheets. Contact angle data were obtained using three pure liquid including water, glycol and diiodomethane. As shown, the contact angle of DI water on both 304 and 316 stainless steel sheets are approximately 64°. However, when using glycol, the contact angle value on 304 stainless steel sheet was 64.2°, while that with 316 SS sheet was 80.3°. For nonpolar organic liquids, the contact angles of diiodomethane on 304 and 316 stainless steel surfaces were dropped to 42.7° and 28.8°, respectively. The present result suggests that the 316 might have more apolar groups on surfaces than 304 SS sheets, resulting in a lower contact angle obtained when using nonpolar organic liquids. The variation in contact angles with different liquids is attributed to variation in interaction energies between liquid molecules and molecules on solid surfaces.

Table 2.2. Contact angles of three pure liquids on cleaned stainless steel surfaces.

Stainless Steel	Contact Angle (°)		
	Water	Glycol	Diiodomethane
304	64.4	64.2	42.7
316	64.7	80.3	28.8

The plasma treatment removes organic hydrocarbon residues on stainless steel plates and rendering surfaces of stainless steel plates hydrophilic. In addition, the ozone gas generated during the plasma treatment oxidizes stainless steel surfaces, rendering the surface hydrophilic. Table 2 shows the contact angle results obtained with plasma-treated stainless steel plates. As shown, the contact angles of all three testing liquids was decreased compared to those obtained without plasma treatment. For instance, the contact angle of water droplets on plasma-treated 304 stainless steel plate was 41.6°, while those obtained without plasma treatment is 64.4°. The results were consistent when using glycol or diiodomethane as wetting liquids. The present result confirms that the use of plasma treatment effectively lowers the hydrophobicity of stainless steel plates.

Table 2.3. Contact angles of three pure liquids on cleaned stainless steel surfaces after the surfaces were treated with plasma.

Stainless Steel	Contact Angle (°)		
	Water	Glycol	Diiodomethane
304	41.7	39.5	34.9
306	41.3	44.3	29.8

## 7.5 Determination of Surface Tension Components

The surface free energies of stainless steel sheets were determined using acid-base theory as described in the aforementioned paragraph. The analysis result shows that the surface energy components  $\gamma_s^{LW}$ ,  $\gamma_s^+$ , and  $\gamma_s^-$  for 316 stainless steel sheet are 44.3, 34.5 and 0.36 mN/m, respectively. Comparing the surface energy data with and without treatment, the  $\gamma_s^{LW}$  for 316 stainless steel surface remained constant while the  $\gamma_s^+$  value was decreased from 34.5 mN/m to 1.1 mN/m after the plasma treatment. The results confirmed that the plasma treatment removes polar components on surfaces.

The results obtained with 304 stainless steel are the same as those obtained with the 316 stainless steel. As shown, both  $\gamma_s^-$  and  $\gamma_s^+$  were decreased after the plasma treatment. It is interesting to note that the non-polar component, i.e. van der Waals component, of the surface free energy was reduced from 42.1 mN/m to 38.2 mN/m after the plasma treatment. The reduction in non-polar component of surface energy might be associated with oxidation of stainless steel surface by ozone gas. However, we cannot exclude the possible calculation errors associated with the determination of surface free energy despite much efforts have been devoted on result accuracy.

Table 2.4. Surface tensions of 304 and 316 stainless steel plates with and without plasma treatment.

Material s	Plasma	$\gamma_s^{LW}$ (mN/m)	$\gamma_s^-$ (mN/m)	$\gamma_s^+$ (mN/m)
304	w/ treatment	38.2	19.9	0.02
	w/o treatment	42.1	30.4	1.15
316	w treatment	44.7	1.1	0.37
	w/o treatment	44.3	34.5	0.36

### Findings:

- Plasma treatment lowers the contact angle of water on stainless steel surfaces while increasing the contact angle of glycols on surfaces.
- Mechanisms include 1) plasma treatment significantly lowers acidic components of surface free energies, but not the dispersing van der Waals (or non-polar) component of surface free energies. The present study confirmed that the use of plasma treatment can effectively increase the wettability of stainless steel surfaces resulting in an improved efficiency of dust collection using the liquid-coated mesh. However, the durability of plasma treatment in rendering surfaces hydrophilic requires further investigation.

## 8.0. Acknowledgement/Disclaimer:

This study was sponsored by the Alpha Foundation for the Improvement of Mine Safety and Health, Inc. (ALPHA FOUNDATION). The views, opinions and recommendations expressed herein are solely those of the authors and do not imply any endorsement by the ALPHA FOUNDATION, its Directors and staff.

## 9.0 References:

[1] Petsonk, E.L., C. Rose, and R. Cohen, *Coal Mine Dust Lung Disease. New Lessons from an Old Exposure*. American Journal of Respiratory and Critical Care Medicine, 2013. **187**(11): p. 1178-1185.

[2] Laney, A.S. and D.N. Weissman, *Respiratory Diseases Caused by Coal Mine Dust*. Journal of occupational and environmental medicine / American College of Occupational and Environmental Medicine, 2014. **56**(0 10): p. S18-S22.

[3] NIOSH, *Criteria for a Recommended Standard: Occupational Exposure to Respirable Coal Mine Dust*, U.S. Department of Health and Human Service, Editor. 1995: Cincinnati, OH. p. 1-336.

[4] Page, S.J., et al., *Equivalency of a personal dust monitor to the current United States coal mine respirable dust sampler*. Journal of Environmental Monitoring, 2008. **10**(1): p. 96-101.

[5] National Research Council (U.S.). Committee on Measurement and Control of Respirable Dust, *Measurement and Control of Respirable Dust in Mines: Report of the Committee on Measurement and Control of Respirable Dust*. 1980, National Academy of Sciences. p. 1-405

[6] Organiscak JA, Klima SS, Pollock DE. *Empirical engineering models for airborne respirable dust capture from water sprays and wet scrubbers*. Mining engineering, 2018. **70**(10): p. 50-57.